Magnetorheology in Rotating Magnetic Fields

by

Arlex Chaves Guerrero

A thesis submitted in partial fulfillment of the requirements for the degree of

Doctor of Philosophy
in
Chemical Engineering

UNIVERSITY OF PUERTO RICO
MAYAGÜEZ CAMPUS
2007

Approved by:

Aldo Acevedo, PhD Member, Graduate Committee	Date
Jaime Benítez, PhD Member, Graduate Committee	Date
Nellore Venkataraman, PhD Member, Graduate Committee	Date
Carlos Rinaldi, PhD President, Graduate Committee	Date
Nairmen Mina, PhD Graduate Studies Representative	Date
Nelson Cardona Martínez, PhD Chairperson of the department	Date

Magnetorheology in Rotating Magnetic Fields

by

Arlex Chaves Guerrero

Submitted to the Department of Chemical Engineering

on July 11, 2007, in partial fulfillment of the

requirements for the degree of

Doctor of Philosophy

Abstract

We studied the flow of ferrofluid induced by rotating magnetic fileds. This flow was observed for first time in 1967 by Moskowitz and Rosensweig [*Appl. Phys. Lett.*, **10**, pag. 301 (1967)] and since then researchers has attempted to explain the phenomenon through theories such as spin diffusion, magnetic tangential surface stresses, and others that claim the impossibility in to obtain ferrofluid flow through a uniform rotating magnetic field. These theories have been tested using experimental observations of tracer particles on the free surface of the container because of the difficulty in obtaining bulk velocity profiles by traditional methods. Nevertheless, as is demonstrated herein such surface velocity profiles are inadequate for the assessment of bulk flow theories as they misrepresent the bulk flow of the fluid and as such can be the cause of confusion.

The principal contribution of the thesis is to provide experimental evidence that allows clarification of the mechanism responsible for the observed flow. To this end we focused on the flow of ferrofluid induced by a rotating magnetic field in a cylindrical container and between two coaxial cylinders. In order to obtain bulk flow measurements we used the ultrasound velocity profile method. Bulk flow measurements taken in the cylindrical container show the fluid co-rotating with the field in a rigid-body-like fashion throughout most of the bulk region of the container, except near the air-fluid interface, where it was observed to counter-rotate. Our experimental measurements show qualitative agreement with an extension of the spin diffusion theory of Zaitsev and Shliomis [*J. Appl. Mech. Tech. Phys.* **10**, pag. 696 (1969)], obtained using the regular perturbation method. An estimate of the spin viscosity is obtained from comparison of flow measurements and theoretical results of the extrapolated wall velocity from

the regular perturbation method. The estimated value $\eta' = 5.8 \times 10^{-10}\,\mathrm{kg\,m\,s^{-1}}$ is several orders of magnitude higher than that obtained from dimensional analysis.

We present the first measurements of bulk flow for ferrofluid in the annular gap between two stationary coaxial cylinders. These results contrast with current theories which only predict flow when one of the cylinders is free to rotate. Qualitative comparison of the experimental results with the predictions of the spin diffusion theory for the annular flow of ferrofluid in the limit of low fields were found in good agreement with velocity profiles obtained for the kerosene based ferrofluid.

Thesis Supervisor: Dr. Carlos Rinaldi

Magnetoreología en Campos Magnéticos rotando

por

Arlex Chaves Guerrero

Sometida al Departamento de Ingeniería Química

en Julio 11 del 2007, en cumplimiento parcial de los

requerimientos para el grado de

Doctor en Filosofía

Resumen

Se estudió el flujo de ferrofluido inducido por un campo magnético rotando. Este fenómeno fue observado por primera vez en 1967 por Moskowitz y Rosensweig [*Appl. Phys. Lett.*, **10**, pag. 301 (1967)]. Desde entonces investigadores han intentado explicar el mecanismo de flujo a través de teorías tales como "spin diffusion", "magnetic surface stresses" y otras que plantean la imposibilidad de obtener flujo usando un campo magnético uniforme rotando. Como consecuencia del color oscuro de los ferrofluidos, ha existido dificultad en obtener perfiles de velocidad dentro del volumen de estos usando métodos convencionales. Por tal razón, estas teorías han sido evaluadas usando perfiles de velocidad tomados en la superficie del contenedor sin embargo, como es demostrado aquí, estos perfiles son inadecuados para evaluar teorías válidas en el volumen del fluido.

La principal contribución de esta tésis es proveer evidencia experimental que permita clarificar el mecanismo responsable por el flujo observado. Para este fin, nos hemos enfocado en el flujo de ferrofluido inducido por un campo magnético rotando, usando dos diferentes geometrías: contenedor cilíndrico y cilindros coaxiales. Perfiles de velocidad tomados en el volumen del fluido fueron obtenidos utilizando una nueva técnica basada en ultrasonido. Estos perfiles mostraron el fluido rotando en la misma dirección del campo magnético y con movimiento similar al de un cuerpo rígido en la mayor parte del volumen del contenedor, excepto cerca de la interface aire-fluido, en la cual el fluido fue observado rotando en dirección opuesta a la del campo magnético. Nuestras medidas experimentales están en cuantitativo acuerdo con las predicciones teóricas obtenidas usando la teoría de "spin diffusion" propuesta por Zaitsev y Shliomis [*J. Appl. Mech. Tech. Phys.* **10**, pag. 696 (1969)], la cual fue obtenida usando el método de

perturbación regular para valores moderados de amplitud del campo magnético. Un estimado del parámetro de "spin viscosity" de $\eta' = 5.8 \times 10^{-10}\,\mathrm{kg\,m\,s^{-1}}$ fue obtenido el cual es varios órdenes de magnitud mayor que el estimado usando análisis dimensional.

Además, se presentan las primeras medidas de flujo en el volumen de ferrofluido contenido en el espacio anular entre dos cilindros coaxiales sin movimiento las cuales estan en cualitativo acuerdo las predicciones obtenidas usando la teoría de "spin diffusion" en el límite de bajos campos. Este resultado contrasta con teorías actuales, las cuales predicen flujo solo en el caso de que a uno de los cilindros le sea permitido rotar.

Consejero de tésis: Dr. Carlos Rinaldi

Este trabajo es dedicado a mis padres,

Oscar Julio Chaves

y

Maria Gladis Guerrero

Por su ejemplo, por los innumerables sacrificios, por su perseverancia, por enseñarme a amar lo que hago, por su amor desinteresado, por creer en mi a pesar de todas las promesas que no he podido cumplir, por siempre estar a mi lado a pesar de la distancia y por animarme a alcanzar mis metas por mas difíciles que estas se vean. Los amo.

Acknowledgements

Definitively, this investigation would not had been the same without the direction and scientific vision of my advisor, Dr. Carlos Rinaldi. Also it is necessarily mentioned his patience and effort in correcting my English writing.

I feel fortunate for the laboratory partners with whom I shared lots of pleasant moments, specially Victoria Calero, Adriana Herrrera, and Carola Barrera. An important part of this work was made by Efren Mercado who gave shape in polycarbonate to several ideas, including those that did not work.

Special mention is for my wife Lilibeth who with patience, love, and special life sense has encouraged my walk with God. Haniel my baby who came to put smiles in my life. I would like to thank my sister Milena and my brother Oscar for their unconditional love. To John Jairo Gil for your insistence that I pursue graduate studies in Puerto Rico. To Ena Brito and Ovidio Graniela for making us part of your family. I would like to thanks the Christian church Catacumba 5 in Mayagüez for showing me the love of Christ. To Milton Rivera for your advise, disposition to help me, and friendship.

This research was supported by the US National Science Foundation (CTS-0320534, CTS-0331379, and CTS-0457359). Acknowledgement is made to the Donors of the American Chemical Society Petroleum Research Fund (ACS-PRF 440867-G 9) for partial support of this research. The author wish to acknowledge the financial support of NSF-EPSCoR Doctoral Fellowship during the last year of the project.

Contents

List of Figures

List of Tables

Chapter 1

Introduction

1.1 Ferrohydrodynamic flows

Ferrofluid flows are the subject of ferrohydrodymanics, a branch of fluid mechanics dealing with the flow of magnetically dipolar media. Ferrohydrodynamics is analogous to, yet dissimilar from, magnetohydrodynamics and electrohydrodynamics. Whereas magnetohydrodynamics is focused on the effects of the Lorentz force on moving charges, ferrohydrodynamics deals with the effects of the Kelvin-type force and couple densities on dipolar fluids. This also differs from electrohydrodynamics due to the non-existence of magnetic poles, which would be analogous to free charge [1, 2]. The term ferrohydrodynamics was introduced in 1964 by Neuringer and Rosensweig [3] in their paper *"Ferrohydrodynamics"* which is considered as the first publication in this science. This research field has grown due to the interest in using ferrofluids in the presence of a magnetic fields in order to convert magnetic energy into motion without the use of moving macroscopic mechanical parts.

Ferrofluids are stable colloidal suspensions of single domain magnetic nanoparticles, usually magnetite (Fe_3O_4), of diameter between 10 to 15 nm in a carrier liquid, typically water or oil [1], and in which the volumetric fraction of magnetic particles is seldom higher than 0.10. Because these particles are single domain and have a total magnetic moment $m \approx 2 \cdot 10^{-19}\,\mathrm{A\,m^2}$, they can be treated as magnetic dipoles in the carrier liquid [4]. This characteristic allows describing the magnetic behavior of ferrofluids with concepts similar to those used for paramagnetic gases. In the absence of a magnetic field the dipolar moment m is randomly oriented and the fluid has

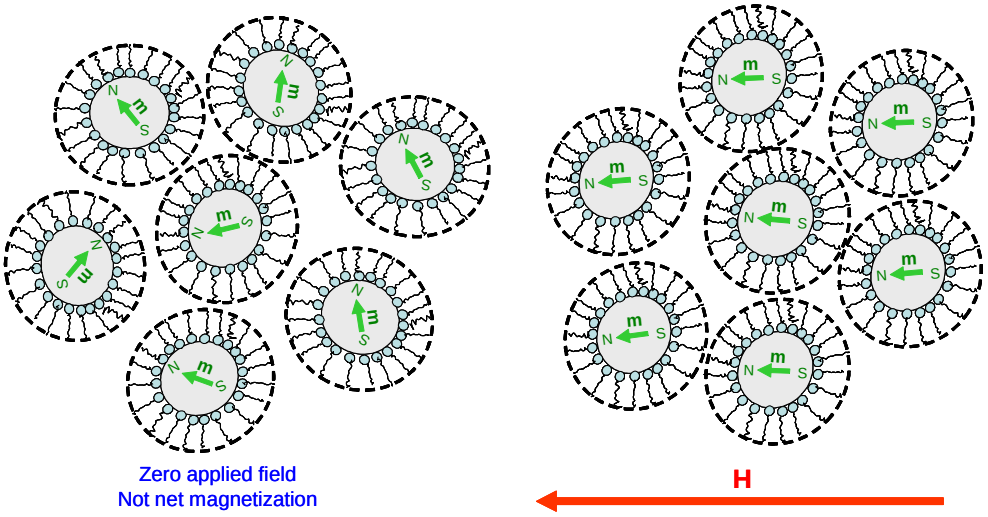

Figure 1-1: Shematic illustration of the magnetization process of ferrofluids. Single domain magnetic particles with embedded magnetic moment m are suspended in a liquid carrier and affected by thermal agitation. The left hand side shows that the magnetic moment of the particles is randomly oriented in the absence of a magnetic field, resulting in no net magnetization of the ferrofluid. The right hand side illustrates how the magnetic moment of the particles is aligned in the direction of a magnetic field whose strength **H** is sufficient to overcome the thermal agitation.

no net magnetization. When a moderate magnetic field is applied, the magnetization is only partially aligned in the direction of the field due to the opposition of thermal agitation. For very high magnetic fields the magnetization is completely aligned in the direction of the field, overcoming the Brownian motion of the particles and reaching the saturation magnetization value M_s, Fig. (1-1). This dependence of the equilibrium magnetization on the magnetic field and temperature is accurately described by the Langevin equation for a monodisperse colloidal ferrofluid

$$\frac{\mathbf{M}_{eq}}{\phi M_d} = L(\alpha)\frac{\mathbf{H}}{H},\ L(\alpha) = \coth\alpha - \alpha^{-1},\ \alpha = \frac{mH}{k_B T}. \tag{1.1}$$

Here $L(\alpha)$ is the Langevin function and α is the Langevin parameter, a measure of the relative magnitudes of magnetic to thermal energy. In (1.1) M_d is the domain magnetization of the magnetic nanoparticles, k_B is Boltzmann's constant, and T is the absolute temperature.

1.1.1 Ferrofluid applications

Since their invention in 1964, interesting phenomena have been observed in ferrofluids, such as: viscosity increase in stationary (DC) magnetic fields [5]; increasing and decreasing effective viscosity in alternating (AC) and rotating magnetic fields [6,7]; field induced flow of a ferrofluid in a stationary cylindrical container in uniform rotating magnetic field [8,9]; and various ferrohydrodynamic instabilities induced by DC magnetic fields. These phenomena arise due to the strong influence exerted by even moderate magnetic fields, in the order of a few tens of mT, over the magnetic particles that act as magnetic dipoles dispersed in the fluid.

The possibility of magnetic flow control and of designing new ferrofluids using different liquid carriers (such as organic and aqueous solvents) [10] has led to the development of a wide variety of applications in engineering, from microdevices to biomedical treatments. Typical commercial applications use DC magnetic fields generated by permanent magnets and ferrofluids as a liquid O-ring in rotary and exclusion seals, as dampers in stepper motors and shock absorbers, and for heat transfer enhancement in audio speakers and electrical transformers. Some recent biomedical applications of magnetic nanoparticles include magnetic resonance imaging, magnetic targeting of drugs and radioactive elements, and magnetic fluid hyperthermia or magnetocytolysis, the magnetic particle induced death of cells under an AC magnetic field. In magnetocytolysis magnetic particles linked to the membrane of a cell rotate and destroy the cell when subjected to an alternating magnetic field by dissipating magnetic energy as heat [11].

1.1.2 Ferrohydrostatics

The first set of ferrohydrodynamics equations presented by Neuringer and Rosensweig assumed that the magnetization $\mathbf{M}$ is collinear with the field $\mathbf{H}$ and that the equilibrium magnetization is determined by Eqn. (1.1). This implies that the magnetization is not affected by ferrofluid flow, however flow is affected by magnetization. The set ferrohydrodynamics equations obtained under these assumptions is known as a quasistationary theory and permits describing phenomena such as the shape of a static meniscus, the behavior of a magnetic liquid under an applied magnetic field, operation of magnetic fluid seals, etc. [1,2].

A more realistic view over that of ferrohydrostatics, is to consider that there exists a finite

time in which m comes to its equilibrium state after the magnetic field has shifted in direction. This relaxation time arises due to two mechanisms: i) The Brownian relaxation time, in which m rotates fixed to the particle and the rotation is resisted by the surrounding liquid, and ii) the Néel relaxation time, where m rotates inside the particle, whereas the particle itself does not rotate [12]. When ferrofluid relaxes by either mechanism, the magnetization $\mathbf{M}$ is non-collinear with field $\mathbf{H}$, resulting in a magnetic couple $\mu_0(\mathbf{M} \times \mathbf{H})$ on the particles, in addition to the magnetic body force $(\mathbf{M} \cdot \boldsymbol{\nabla}\mathbf{H})$. This last situation is studied in this thesis through a combination of theoretical and experimental work.

1.2 Background and motivation

This thesis is concerned with the ferrohydrodynamics of ferrofluids in rotating magnetic fields, particularly: (i) the flow of a ferrofluid in a stationary cylindrical container (commonly referred to as spin up flow), (ii) and the flow of a ferrofluid between coaxial cylinders. In both cases the rotating magnetic field is oriented in the plane perpendicular to the cylinder axis. These flows are characterized by a body couple-density $\mu_0 (\mathbf{M} \times \mathbf{H})$ arising from the non-colinearity of the magnetization vector $\mathbf{M}$ with the magnetic field vector $\mathbf{H}$, due to the viscous opposition to rotation of the magnetic particle relative to the liquid matrix. These body couples are then the origin of a state of antisymmetric stress in the suspension.

Experimental data has been reported for spin up flow and flow of ferrofluid in coaxial cylinders. These efforts were directed at determining: (i) the direction of the flow in relation to the direction of rotation of the magnetic field [9], (ii) measurements of torque on the wall of the cylindrical container [13] (spin up flow torque) and on the inner stationary cylinder (the spindle) [14–16], and (iii) obtaining measurements of the free surface velocity profile for spin up flow and in the annular geometry [17, 18]. Free surface flows were measured because of the difficulty in obtaining velocity profiles in the bulk fluid by conventional methods due to the opaque character of ferrofluids. Unfortunately, many of these studies have been plagued by inconsistencies and confusion. Examples include: (i) the use of magnetic suspensions with particle diameters of several micrometers (now referred to as magnetorheological fluids), (ii) using concentrated colloidal suspensions (slurries), (iii) lack of thorough physical and magnetic

characterization of the suspensions, and (*iv*) usage of non-uniform rotating magnetic fields. Likewise, velocity profile measurements in the free surface are strongly influenced by surface effects, as was observed by Rosensweig *et al.* [17].

The first analysis for the problem of spin-up flow was developed by Zaitsev and Shliomis [19] using the ferrohydrodynamic equations and including the effect of spin viscosity η', but assuming that the spin-magnetization coupling term $\boldsymbol{\omega} \times \mathbf{M}$ in the magnetization equation was negligible. The solution obtained had the character of a boundary layer close to the container wall and rigid-body motion in the core of the flow. However, the predicted co-rotation of field and fluid was contrary to the limited experimental data on free surface velocity profiles. Theoretical alternatives were presented by Jenkins [20] and Glazov [21], who both assumed that the spin viscosity was zero. Both agreed that it is not possible to induce a rotating flow by a uniform rotating magnetic field alone if $\eta' = 0$. According to Glazov, the observed rotation was due to field in-homogeneities in the azimuthal direction. An extension of the analysis of Zaitsev and Shliomis was obtained by Rinaldi [22], where the classical spin-diffusion theory was extended to account for the spin-magnetization coupling in the magnetization equation. The analysis applied a regular perturbation expansion in powers of the small parameter $\tau\Omega \ll 1$ (where Ω is the radian frequency of the applied magnetic field and τ is the relaxation time) and applies to low amplitudes of the magnetic field where $\alpha \to 0$. The analysis showed that the original result of Zaitsev and Shliomis [19] corresponds to the first-order term in the general expansion scheme and predicts rigid body-like co-rotation of field and ferrofluid up to third order in the solution.

1.3 Overview of the thesis

Chapter 2 presents predictions for the zeroth and first order contributions of the θ-directed velocity component, z-directed spin velocity, and torque for spin-up flow of ferrofluid in a cylindrical container. This analysis was obtained using the regular perturbation method. The analysis is an improvement to the original analysis of Zaitsev and Shliomis [19] and the analysis presented by Rinaldi [22], which are valid for low strengths of the magnetic field where the magnetization is proportional to the magnetic field. The analysis presented in Chapter 2 predicts

flow in the zeroth order contribution and takes into consideration saturation of the ferrofluid in moderate fields.

In Chapter 3, we revise the theoretical analysis for flow of ferrofluid in an annular gap in a rotating magnetic field, showing that the theoretical expression for torque presented by Pshenichnikov and Lebedev [15] is incorrect as the integration constants for magnetic field and magnetization do not satisfy Maxwel's equations. Here we present the correct expression for the torque on the external surface of the inner cylinder in the annular geometry and then compare this with the expression obtained by Rinaldi *et al.* [16]. In addition, the analysis for spin up flow of Chapter 2 is extended to the annular case obtaining the zeroth order contribution of the velocity field. As is detailed in this Chapter, this analysis predicts flow even though both cylinders are stationary whereas all previous theoretical work predicts there is no flow.

Chapter 4 presents the experimental setup for the torque and velocity profile measurements and a complete characterization of the ferrofluids used. Several methods were used in determining estimates of the average diameter of the particle which were compared with direct measurements of the average particle diameter obtained from TEM and assuming that the size distribution obeys a log-normal distribution function. The Brownian and Néel relaxation times were estimated using the commonly used expressions given in the literature, which do not take into account polydispersity. These were compared with values obtained with a new expression given by Rinaldi [23] that quantifies the size distribution observed in our ferrofluids.

Chapter 5 presents the first velocity profiles measured in the bulk of a ferrofluid for spin up flow, and shows that volumetric effects are responsible in driving the flow. However, velocity profiles without cover show that surface effects are also present. A complete characterization of the flow is presented, including measurements of the azimuthal component of velocity around the container and at different heights, as well as measurements of the axial component of velocity. Torque measurements for two different volumes of water and kerosene based ferrofluids and their dilutions are presented. Measurements of torque on the inner surface of two hollow spindles with different volumes are reported for each one of the ferrofluids characterized in Chapter 4. Log-log plots of the experimental torque normalized using the expression of the theoretical torque vs the dimensionless applied magnetic field α and vs dimensionless frequency were used to assess the agreement between experimental torque data and theoretical predictions. Finally, the first

comparison between bulk velocity profiles and theoretical predictions of the spin diffusion theory are presented and an estimate of the spin viscosity for EMG900 ferrofluid is obtained.

Chapter 6 presents measured bulk velocity profiles for annular flow of ferrofluid. These measurements show that, contrary to the consensus in the literature, there exists a flow even though both cylinders are fixed. This is in agreement with the theoretical results obtained in Chapter 3. Measurements of torque on the surface of the inner cylinder for several ratios of inner to outer cylinder radii are reported for each of the ferrofluids characterized in Chapter 4. Log-log plots of the experimental torque normalized using the expression of the theoretical torque vs the dimensionless applied magnetic field α and vs dimensionless frequency were used to assess the agreement between experimental torque data and theoretical predictions.

In Chapter 7 we discuss the more relevant contributions of the thesis. Qualitative comparison of the experimental results and predictions of several theories showing the spin diffusion theory as the mechanism responsible for the flow. The next step in this field must be directed to obtain a theoretical or numerical analysis that permit obtained solutions valid for high fields and a more effort must be made to obtain rheological parameters that permit quantify the effect of couple stresses through of estimates of spin viscosity.

Finally we include Appendices where the complete set of flow and torque measurements are presented for spin up and coaxial geometry.

Chapter 2

Theoretical flow analysis for ferrrofluid in a cylindrical container subjected to a uniform rotating magnetic field

2.1 Spin-up flow of ferrofluids

The phenomenon of spin-up flow of a ferrofluid, a stable colloidal suspension of permanently magnetized nanoparticles, in a cylindrical container and subjected to an applied rotating magnetic field which is uniform in the absence of the ferrofluid has received considerable attention in the development of the field ferrohydrodynamics [1, 8, 15, 17, 19, 21, 24–31]. Typically, experiments are carried out by placing a sample of ferrofluid in a cylindrical container subjected to a rotating magnetic field. This setup is suitable for studying the coupling between internal angular momentum, related to the "spin" of the subcontinuum magnetic particles, and the macroscopic or "external" angular momentum, related to the experimentally observable macroscopic flow of the suspension. In a stationary cylindrical container, surface velocity profiles show the ferrofluid rotating, rigid-body-like, in a direction which depends on the applied magnetic field amplitude, frequency, and rotation direction. Such essentially rigid-body motion is

observed in the inner core of the ferrofluid and extends close to the stationary cylindrical vessel wall. To make such observations, tracer particles are often placed on the rotating free surface – ferrofluid is opaque making probing of bulk flow profiles through optical methods difficult. Usage of such free-surface tracers limits the accuracy of measurements close to the container wall. Furthermore, interfacial curvature coupled with magnetic surface shear stresses drive a surface flow [17], making free-surface measurements unsuitable in determining the bulk flow.

Related work using either unstable or concentrated suspensions of particles or using non-uniform magnetic fields include Brown and Horsnell [9], Kagan *et al.* [32], and Calugaru *et al.* [33]. These authors report observations where the magnetic fluid switches between co-rotation and counter-rotation with respect to the applied magnetic field depending on magnetic field amplitude and frequency. Explicitly, Brown and Horsnell [9] observe co-rotation of field and fluid for low applied fields and counter-rotation for high applied magnetic fields, whereas Kagan *et al.* [32] and Calugaru *et al.* [33] observe counter-rotation for low applied magnetic fields and co-rotation for higher applied fields.

Observations of counter-rotation of field and fluid led Brown and Horsnell [9] to investigate the direction in which the cylindrical container would rotate if it could freely do so. This represents an indirect measurement of the torque exerted by the ferrofluid on the container wall. One would expect the counter-rotating fluid to drag the cylindrical container with it, but experiments show the container co-rotating with the field whereas the fluid counter-rotates. Such observations, have since been corroborated by Kagan *et al.* [32] and Rosensweig *et al.* [17].

Various authors [1, 8, 17, 19, 21, 24, 25, 29, 31] have attempted theoretical analyses aimed at explaining experimental observations of free surface flow profiles. The spin diffusion theory, due to Zaitsev and Shliomis [19], assumes the magnetic field throughout the ferrofluid region is uniform, with concomitant uniform magnetization of the ferrofluid. The resulting magnetic body couple is uniform whereas the magnetic body force is exactly zero. Within the assumptions of their analysis, the ferrofluid flow field is determined analytically using the phenomenological structured continuum theory [34–36] which includes the effects of antisymmetric stresses, body couples, and couple-stresses representing the short-range surface-transport of internal angular momentum. The spin-diffusion results of Zaitsev and Shliomis [19] were subsequently used to estimate the magnitude of the phenomenological coefficient of spin viscosity, appearing in the

commonly accepted constitutive form of the couple-stress pseudo-dyadic, as well as to analyze/interpret experimental observations [17, 26]. Unfortunately, as pointed out by Rosensweig *et al.* [17], this analysis fails to correctly predict the experimentally observed free-surface flow magnitude and direction.

The spin-diffusion theory [19] and other [1, 17, 29] analyses adapted therefrom assume that the fluid magnetization is proportional to the magnetic field, limiting the solution range to low values of the applied magnetic field where the Langevin parameter α, appearing in the equilibrium magnetization relation, is negligible ($\alpha \ll 1$). Also, these analyses neglect or are inconsistent with the spin-magnetization coupling in the phenomenological magnetization relaxation Eqn. (2.7) of Shliomis [37]. This can be most clearly seen in [19], where the magnetization Eqn. lacks the $\boldsymbol{\omega}(\mathbf{x}) \times \mathbf{M}(\mathbf{x})$ term on the right-hand-side of (2.7). It is neglected in, or rather is inconsistent with, the analysis the Rosensweig *et al.* [17] and Kaloni [29] when they assume the field and magnetization are uniform throughout of ferrofluid. This is illustrated when one considers that a position dependent spin field, as obtained in their contributions, is inconsistent with a uniform magnetic field and magnetization, as assumed in their treatments, in the magnetization relaxation Eqn. (2.7). The importance of the spin-magnetization coupling term $\boldsymbol{\omega}(\mathbf{x}) \times \mathbf{M}(\mathbf{x})$ in predicting novel ferrofluid behavior has been shown previously by Zahn and coworkers [38–41], where the situation of plane-Pouseuille/Couette flow of ferrofluid subjected to alternating and rotating magnetic fields was analyzed.

An alternative theoretical explanation for the observed flow phenomena was developed by Glazov [21, 24, 25]. The analysis considers the effect of higher-order spatial harmonics, expected to occur in practice due to non-idealities in the stator winding distribution, e.g., due to slot effects. Essentially, Glazov's analysis considers the same phenomenological theory used by Zaitsev and Shliomis [19] and others [1, 17, 29], but neglects contributions due to couple-stresses in the ferrofluid. Glazov's analysis, in its various forms and stages, essentially concludes that flow would not occur in the absence of the higher-order harmonics when a two pole winding distribution is used as the source of the applied magnetic field. Hence, according to Glazov, experimental observations of spin-up flow are entirely attributed to imperfections in the experimental apparatus and the concomitant higher-order spatial harmonics in the magnetic field distribution. Still, the predictions of Glazov fail to explain the experimentally observed counter-

rotation of field and ferrofluid at the free surface [17].

At least three other hypotheses have subsequently been advanced in the literature to explain the observed phenomena: (i) that the flow is entirely driven by free surface curvature and surface excess forces [17]; (ii) that the observed phenomenon results due to a shear-stress dependent slip boundary condition [42] on the ferrofluid translational velocity coupled with a spin-slip boundary condition [29, 43]; and (iii) that an energy dissipation mechanism gives rise to temperature gradients, with concomitant gradients in magnetic properties, resulting in magnetic body forces which drive flow in the direction opposite field rotation [31, 44].

That surface curvature dependent flows indeed occur in ferrofluids was demonstrated by the experiments of Rosensweig *et al.* [17]. In their study, free-surface rotation rate and direction was measured for the meniscus formed by a dilute water-based ferrofluid in a 9.5 mm internal diameter capillary tube subjected to uniform rotating magnetic fields of increasing amplitude. The shape of the meniscus was switched from concave to convex by modifying the capillary surface properties. With a concave meniscus the magnetic field and fluid were observed to counter-rotate, whereas magnetic field and fluid where observed to co-rotate with a convex meniscus. Additionally, Rosensweig *et al.* [17] observed that the angular rotation rate of the free surface increased as the internal diameter of the cylindrical container decreased. This, they remarked, is contrary to usual expectations in viscous flows. These observations led Rosensweig *et al.* [17] to conclude that "surface stress rather than volumetric stress is responsible for the spin up phenomenon".

Another explanation was suggested by Kaloni [29], who attributed the experimental observations of [17] to a slip velocity boundary condition. Kaloni obtained the translational and spin velocity fields between two stationary coaxial cylinders subjected to an externally-applied uniform rotating magnetic field. However, Kaloni fails to make definite predictions based on the magnitude and direction of spin-up flows in ferrofluids under typical experimental conditions.

A third theory, due to Shliomis *et al.* [44], suggested that spin-up flow is driven by nonuniformity of magnetic permeability due to radial temperature gradients produced by viscous dissipation in the microeddies that arise around the rotating particles, especially at high frequencies. This view was extended analytically by Pshenichnikov *et al.* [31], predicting counter rotation of fluid and field for frequencies below 10^5 s^{-1}(16 kHz) and a maximum of the ve-

locity profile located at $r = R_O/\sqrt[3]{3}$ (R_O is the radius of the outer container), independent of the properties of the fluid. In addition, Pshenichnikov *et al.* claim that for low frequencies and amplitudes of the magnetic field the flow is driven only by tangential magnetic stresses on the free boundary of the fluid.

Chaves *et al.* [45] reported experimental bulk velocity profile measurements obtained using the Ultrasound Velocity Profile (UVP) method for ferrofluid under a uniform rotating magnetic field. These measurements showed rigid-body-like azimuthal velocity profiles co-rotating with the field throughout the bulk of the container, in qualitative agreement with the predictions of [19]. Likewise, it was observed that the flow direction at the free surface is opposite to the direction of field rotation as in [17]. These experiments [45] suggest that two different mechanisms operate in driving the flow; surface shear stresses for the fluid near the top free surface and volumetric effects for the bulk. Furthermore, these observations demonstrate that surface flow measurements are inappropriate in the assessment of bulk flow theories.

Herein we present a complete characterization of bulk flow during spin up using the UVP method, with corresponding torque measurements on the surface of the cylindrical container for two different volumes of fluid. Water and kerosene based ferrofluids were used with several volumetric particle fractions obtained by dilution of the more concentrated commercial ferrofluid. Because the experiments were carried out at non-negligible values of the magnetic field, whereas the spin diffusion theory [19] strictly applies in the limit of zero field, we begin by presenting an asymptotic solution of the ferrohydrodynamic problem, extending the results of [19].

2.2 Analytical approach

Motivated by the experimental evidence presented by Chaves *et al.* [45], where bulk velocity profiles for ferrofluid in a cylindrical container showed qualitative agreement with the spin-diffusion theory, we extend this theory using the regular perturbation method. To this end, the magnetization relaxation Eqn. (2.7) used in our analysis includes a term of $\mathcal{O}\left(\alpha^3\right)$ in the equilibrium magnetization expression, Eqn. (2.8), in contrast to the usual assumption of $\mathbf{M}_{eq} = \chi_i \mathbf{H}$, which only includes the term of order $\mathcal{O}(\alpha)$. In addition, the term $\boldsymbol{\omega}(\mathbf{x}) \times \mathbf{M}(\mathbf{x})$

enters the analysis at first order.

In order to solve the coupled ferrohydrodynamic equations, we will apply a regular perturbation expansion in powers of the small parameter

$$\varepsilon \equiv \frac{\mu_0 \chi_i K^2 \tau}{\zeta}, \tag{2.1}$$

where $\mu_0 \equiv 4\pi \times 10^{-7}$ H/m is the permeability of free space, χ_i is the ferrofluid's initial susceptibility, K is the amplitude of the magnetic field, and τ is the effective relaxation time of the particles. A similar approach, using $\Omega_f \tau$ as the perturbation parameter, was used by Rinaldi and Zahn [41] to analyze the problem of plane-Poiseuille/Couette flow of ferrofluid subjected to externally applied alternating and rotating magnetic fields. There it was shown that, as a consequence of the simplified geometry, the magnetic field and magnetization could be obtained analytically to any order n independently of the translational and spin velocity field. This ceases to be the case in the analogous problem of spin-up flow of ferrofluid in a cylindrical container, requiring determination of the $(n-1)^{th}$ order fields before obtaining the n^{th} order fields. Thus, in the present contribution we consecutively obtain the zeroth- and first-order terms in the regular perturbation expansion of all relevant field quantities for the spin-up flow of a ferrofluid in a cylindrical container when the externally applied rotating magnetic field is uniform in the absence of ferrofluid. The solution procedure consists of determining the zeroth-order magnetic quantities, from which the resulting magnetic force and couples are calculated. These are used in turn to obtain the zeroth-order translational and spin velocity fields. The zeroth-order fields thus obtained are subsequently used to determine the first-order magnetic field and magnetization with concomitant first-order magnetic forces and couples used in determining the first-order flow fields. These steps illustrate the procedure used to obtain the effects of the spin-magnetization coupling to any order in ε, with convergence for $\varepsilon < 1$.

2.3 Analysis of flow and torque

Conceptually, we consider the experimental situation illustrated in Fig. (2-1), consisting of an infinite column of ferrofluid contained in a nonmagnetic cylinder of radius R_O and magnetic permeability μ_0 whose outer wall is constrained to be stationary due to an externally applied mechanical torque. The column of ferrofluid is assumed to be long enough in the z-direction such that end effects may be considered negligible. We are therefore solving for the fields in the bulk and thereby eliminating all aforementioned free-surface-curvature effects, the analysis and effects of which we leave to future contributions. The cylinder is placed in the gap of a magnetic field source, which, for definiteness, we choose to be the idealization of a two-pole magnetic machine stator. The stator winding is modeled as a surface current distribution in the z-direction with real amplitude $K(\theta, t)$ located at radius $r = R_O$, and which varies sinusoidally with time at radian frequency Ω_f and is sinusoidally distributed with angle θ

$$K(\theta, t) = \mathrm{Re}\left\{ K e^{j(\Omega_f t - n\theta)} \right\} \mathbf{i}_z. \tag{2.2}$$

The current distribution is backed with a material of infinite magnetic permeability, $\mu \to \infty$. Here, $j \equiv \sqrt{-1}$ is the imaginary number, n is an integer which for a uniform magnetic field source is 1, and K is the surface current peak amplitude, taken to be real so that, without loss of generality, we have chosen a phase angle of zero for the current distribution. We have made the radii of the ferrofluid container and stator equal for simplicity in the analysis. An air gap would have introduced another region where Maxwell's equations, in the magnetoquasistatic limit, would have to be applied and solved.

2.4 Governing equations

We use the set of ferrohydrodynamic equations summarized in [41,46]. The first is the continuity equation, which assumes the ferrofluid is a homogeneous diluted colloidal dispersion of magnetic particles (subcontinuum units) in an incompressible liquid carrier,

$$\boldsymbol{\nabla} \cdot \mathbf{v} = \mathbf{0}, \tag{2.3}$$

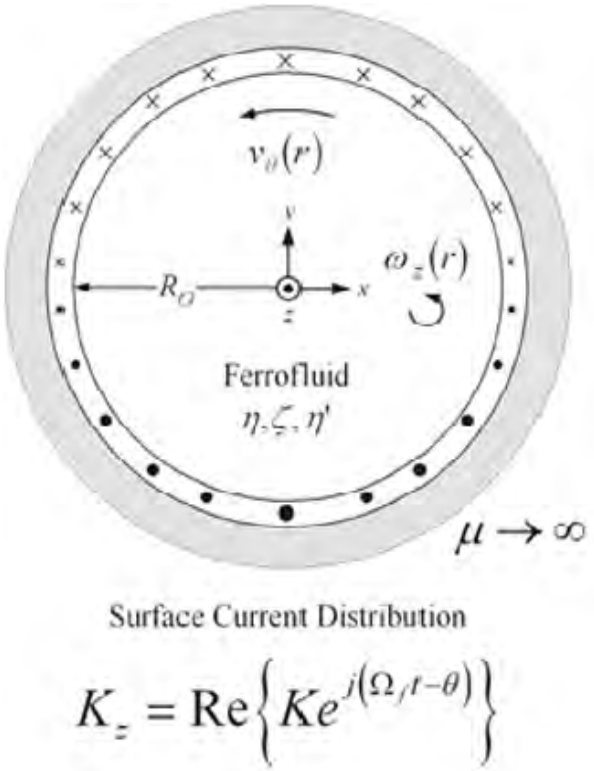

Figure 2-1: Schematic illustration of the coupled magnetic-hydrodynamic problem for spin up flow. The azimuthal velocity component and axial directed spin velocity are obtained for a long column of ferrofluid of external radius R_O subjected to a uniform rotating magnetic field perpendicular to the axis of the cylinder. The magnetic field is modeled as a z-directed surface current distribution $K(\theta, t)\,\mathbf{i}_z$, which is backed by a material of infinite magnetic permeability, $\mu \to \infty$.

where $\mathbf{v}$ is the mass average velocity of the fluid. The second expresses conservation of linear momentum,

$$\rho\frac{D\mathbf{v}}{Dt} = \rho\mathbf{g} + \mu_0\mathbf{M}\cdot\boldsymbol{\nabla}\mathbf{H} - \nabla p - 2\zeta\boldsymbol{\nabla}\times\left(\frac{1}{2}\boldsymbol{\nabla}\times\mathbf{v} - \boldsymbol{\omega}\right) + \eta\nabla^2\mathbf{v}. \tag{2.4}$$

This equation takes into account the asymmetry of the viscous stress tensor, a consequence of body couples exerted on the subcontinun units. In Eqn. (2.4), ρ is the density, $\mathbf{g}$ is the gravitational acceleration, p is the pressure, $\mathbf{M}$ is the magnetization vector of the suspension, $\mathbf{H}$ is the applied magnetic field vector, ζ is the vortex viscosity (a dynamical parameter analogous to the shear viscosity and which characterizes the asymmetric component of the Cauchy stress), $\boldsymbol{\omega}$ is the spin velocity vector, and η is the suspension-scale shear viscosity. The second term on the right hand side of (2.4) represents the magnetic body forces due to field inhomogeneities, whereas the fourth term represents the antisymmetric component of the Cauchy stress, occurring when the particles rotate at a rate different than half the local vorticity of the flow. A dilute limit expression for monodisperse nano-particles suspensions in Newtonian fluids is available for the vortex viscosity

$$\zeta = 1.5\phi_h\eta_0, \tag{2.5}$$

where ϕ_h is the hydrodynamic volume fraction of suspended particles and η_0 is the shear viscosity of the suspending fluid [47].

The spin velocity in the ferrofluid is governed by the internal angular momentum equation,

$$\rho I\frac{D\boldsymbol{\omega}}{Dt} = \mu_0\mathbf{M}\times\mathbf{H} + 4\zeta\left(\frac{1}{2}\boldsymbol{\nabla}\times\mathbf{v} - \boldsymbol{\omega}\right) + \eta'\nabla^2\boldsymbol{\omega}, \tag{2.6}$$

where I is the moment of inertia density of the suspension and η' is the shear coefficient of spin viscosity. The first term on the right hand side of Eqn. (2.6) represents the external body couple density acting on the structured continuum whenever the local magnetization is not aligned with the applied magnetic field. The second term is the antisymmetric vector of the Cauchy stress and represents the interchange of momentum between internal angular and macroscopic linear forms. The third term represents the diffusion of internal angular momentum between contiguous material elements, which has been generally neglected by fixing the coefficient of

spin viscosity to zero. This assumption results in zero flow, as can be easily verified from the analysis presented below.

The suspension magnetization $\mathbf{M}$ represents the local alignment of subcontinuum units and as such must also obey a balance equation. The original equation [37] has been the subject of much recent debate [48–53], but is still regarded as correct for low applied field amplitude and frequency, *i.e.*, when the local magnetization is not far from its equilibrium value. The magnetization relaxation equation, as it is usually called, is then

$$\frac{\partial \mathbf{M}}{\partial t} + \boldsymbol{\nabla} \cdot (\mathbf{v}\mathbf{M}) = \boldsymbol{\omega} \times \mathbf{M} - \frac{1}{\tau} (\mathbf{M} - \mathbf{M}_{eq}) . \tag{2.7}$$

In (2.7), the first term on the right hand side represents the effect of particle rotation on $\mathbf{M}(\mathbf{x})$, whereas the second term accounts for orientational diffusion of $\mathbf{M}(\mathbf{x})$ towards an equilibrium value. The equilibrium magnetization $\mathbf{M}_{eq}$ for a superparamagnetic ferrofluid is given by the Langevin relation [1],

$$\frac{\mathbf{M}_{eq}}{\phi M_d} = L(\alpha) \frac{\mathbf{H}}{|\mathbf{H}|} = \left[\coth \alpha - \frac{1}{\alpha} \right] \frac{\mathbf{H}}{|\mathbf{H}|}, \alpha = \frac{\mu_0 M_d H V_c}{k_B T}. \tag{2.8}$$

Here $L(\alpha)$ is the Langevin function and α is the Langevin parameter, a measure of the relative magnitudes of magnetic and thermal energy. In (2.8) M_d is the domain magnetization of the magnetic nanoparticles, k_B is Boltzmann's constant, T is the absolute temperature, and V_c is the volume of the magnetic cores. The use of an effective relaxation time

$$\frac{1}{\tau} = \frac{1}{\tau_B} + \frac{1}{\tau_N}, \tag{2.9}$$

is commonly assumed because relaxation can occur simultaneously by the Brownian and Néel mechanisms. The Brownian relaxation time is given by

$$\tau_B = \frac{3\eta_0 V_h}{k_B T}, \tag{2.10}$$

with V_h the hydrodynamic particle volume, and the Néel relaxation time is given by

$$\tau_N = \frac{1}{f_0} \exp\left(\frac{K V_c}{k_B T} \right), \tag{2.11}$$

where f_0 is a characteristic frequency of the magnetic material [1], K is the magnetocrystalline anisotropy constant of the magnetite nanoparticles, and V_c is the magnetic volume.

All that remains to complete our description are Maxwell's equations in the magnetoquasi-static limit [54, 55]

$$\boldsymbol{\nabla} \times \mathbf{H} = \mathbf{0}, \ \boldsymbol{\nabla} \cdot (\mathbf{M} + \mathbf{H}) = \mathbf{0}, \tag{2.12}$$

and the corresponding interfacial boundary conditions for the magnetic field, namely continuity of the normal component of magnetic induction and the jump in the tangential magnetic field due to surface currents

$$\mathbf{n} \cdot [(\mathbf{H} + \mathbf{M})_a - (\mathbf{H} + \mathbf{M})_b] = \mathbf{0} \tag{2.13}$$

$$\mathbf{n} \times [\mathbf{H}_a - \mathbf{H}_b] = \mathbf{K} \tag{2.14}$$

in which $\mathbf{n}$ is a unit vector locally normal to the interface pointing from phase b to phase a.

2.5 Fluid boundary conditions

In an attempt to provide an alternate explanation for the observations of Rosensweig *et al.* [17], Kaloni [29] considered the effect of different boundary conditions on the translational and spin velocity fields, in the framework of the Zaitsev and Shliomis [19] analysis. Boundary conditions in structured continuum theories have been under debate for a long time [36, 42, 43, 56–58]. The boundary conditions used by Kaloni [29] are a coefficient-of-friction β dependent slip velocity

$$\mathbf{v} - \mathbf{v}_s = \frac{1}{\beta} \left[\mathbf{n} \times (\mathbf{n} \cdot \mathbf{T} \times \mathbf{n}) \right], \tag{2.15}$$

and a generalized spin-slip condition

$$\boldsymbol{\omega} - \boldsymbol{\omega}_s = \frac{\gamma}{2} \nabla \times \mathbf{v}. \tag{2.16}$$

Here $\mathbf{n}$ is an outward-directed normal unit vector at the boundary, $\mathbf{T}$ the Cauchy stress tensor in the fluid, and $\gamma \in [0, 1]$ is an adjustable coefficient. The subscript s denotes properties of the contacting solid medium.

The translational slip velocity boundary condition (2.15) dates back to Lamb's [59] arguments of slip being opposed by frictional forces at the wall and has been championed by various authors [42, 43]. However, as the slip "friction coefficient" β is inversely proportional to particle radius [42] these effects should be negligible in ferrofluids, where characteristic particle diameters are of the order of 10 nm.

The spin-slip boundary condition (2.16) is a linear combination of the two cases of zero spin and zero asymmetric stress boundary conditions, and is the subject of even further controversy [36, 42, 43, 56–58]. The first case ($\gamma = 0$), corresponds to the possibility of no spin slip of the particles near the wall due to strong particle-wall interaction. In the second case ($\gamma = 1$), the particles rotate at the local vorticity of the fluid, hence antisymmetric stresses are absent in the wall. This boundary condition was initially proposed by Condiff and Dahler [36] and is a simple *ad hoc* alternative, with a single parameter γ, to the general tensorial boundary condition proposed by Aero [43].

2.6 Scaling of the governing equations

Scaling of the governing equations is required in order to formulate a regular perturbation problem which permits an analytical solution by decoupling the ferrohydrodynamic Eqns. (2.3) to (2.12). Field quantities are scaled with respect to their expected characteristic values. The resulting scaled variables are denoted by an over-tilde, are assumed to be of order unity, and are given by

$$\tilde{\mathbf{M}} = \frac{\mathbf{M}}{\chi_i K};\ \tilde{\mathbf{H}} = \frac{\mathbf{H}}{K};\ \tilde{\boldsymbol{\nabla}} = R_O \boldsymbol{\nabla};\ \tilde{r} = \frac{r}{R_O};\ \tilde{t} = \Omega_f t \tag{2.17}$$

$$\tilde{p} = \frac{p}{\mathit{\Pi}};\ \tilde{\mathbf{v}} = \frac{\mathbf{v}}{U_l};\ \tilde{\boldsymbol{\omega}} = \frac{\boldsymbol{\omega}}{\varpi} \tag{2.18}$$

where U_l and ϖ are the characteristic translational and spin velocities [60] and $\mathit{\Pi}$ is the characteristic pressure, assumed to be $\eta\varpi$. As the linear velocity is driven by rotation of the particles, we have chosen for the scale of the linear velocity $U_l = \varpi R_O$. The characteristic spin velocity is then determined by substituting the scaled variables of Eqn. (2.17) in the internal angular

momentum Eqn. (2.6). Grouping terms we obtain,

$$\mathbf{0} = \frac{\mu_0 \chi_i K^2}{\zeta \varpi} \tilde{\Omega}_f \tilde{\mathbf{M}} \times \tilde{\mathbf{H}} + 2\tilde{\boldsymbol{\nabla}} \times \tilde{\mathbf{v}} - 4\tilde{\boldsymbol{\omega}} + \frac{\eta'}{\zeta R_O^2} \tilde{\boldsymbol{\nabla}}^2 \tilde{\boldsymbol{\omega}}. \tag{2.19}$$

The dimensionless frequency defined by $\tilde{\Omega}_f \equiv \Omega_f \tau$ appears in the first term of (2.19) because the magnetic body couple $\tilde{\mathbf{M}} \times \tilde{\mathbf{H}}$ is of order $\sin\theta$, where θ is the angle between $\tilde{\mathbf{M}}$ and $\tilde{\mathbf{H}}$, typically proportional to $\tilde{\Omega}_f$. Thus, from a dominant term analysis the coefficient of the external body-couple density is of order unity only if the characteristic spin velocity is

$$\varpi = \frac{\mu_0 \chi_i K^2 \tilde{\Omega}_f}{\zeta}, \tag{2.20}$$

and consequently

$$\tilde{p} = \frac{\zeta p}{\mu_0 \eta \chi_i K^2 \tilde{\Omega}_f};\ \tilde{\boldsymbol{\omega}} = \frac{\zeta \boldsymbol{\omega}}{\mu_0 \chi_i K^2 \tilde{\Omega}_f};\ \tilde{\mathbf{v}} = \frac{\zeta \mathbf{v}}{\mu_0 \chi_i K^2 \tilde{\Omega}_f R_O}. \tag{2.21}$$

The resulting scaled governing equations, neglecting inertial terms in the linear momentum equation, are

$$\mathbf{0} = \frac{\zeta}{\eta \tilde{\Omega}_f} \tilde{\mathbf{M}} \cdot \tilde{\boldsymbol{\nabla}} \tilde{\mathbf{H}} - \tilde{\boldsymbol{\nabla}} \tilde{p} + 2\frac{\zeta}{\eta} \tilde{\boldsymbol{\nabla}} \times \tilde{\boldsymbol{\omega}} + \frac{\eta_e}{\eta} \tilde{\boldsymbol{\nabla}}^2 \tilde{\mathbf{v}}, \tag{2.22}$$

$$\mathbf{0} = \frac{1}{\tilde{\Omega}_f} \tilde{\mathbf{M}} \times \tilde{\mathbf{H}} + 2\tilde{\boldsymbol{\nabla}} \times \tilde{\mathbf{v}} - 4\tilde{\boldsymbol{\omega}} + \frac{4\eta}{\eta_e \kappa^2} \tilde{\boldsymbol{\nabla}}^2 \tilde{\boldsymbol{\omega}}, \tag{2.23}$$

$$\tilde{\Omega}_f \frac{\partial \tilde{\mathbf{M}}}{\partial \tilde{t}} + \tilde{\Omega}_f \varepsilon \tilde{\mathbf{v}} \cdot \tilde{\boldsymbol{\nabla}} \tilde{\mathbf{M}} = \tilde{\Omega}_f \varepsilon \tilde{\boldsymbol{\omega}} \times \tilde{\mathbf{M}} - \tilde{\mathbf{M}} + \frac{\mathbf{M}_{eq}}{\chi_i K}, \tag{2.24}$$

$$\tilde{\boldsymbol{\nabla}} \times \tilde{\mathbf{H}} = \mathbf{0}, \tag{2.25}$$

$$\tilde{\boldsymbol{\nabla}} \cdot \left(\chi_i \tilde{\mathbf{M}} + \tilde{\mathbf{H}} \right) = \mathbf{0}. \tag{2.26}$$

In the preceding equations we have defined $\eta_e \equiv \eta + \zeta$, and introduced the dimensionless parameter κ

$$\kappa^2 \equiv \frac{4\eta R_O^2 \zeta}{\eta_e \eta'}. \tag{2.27}$$

As can be observed in Eqns. (2.22) to (2.24), the factor $\tilde{\Omega}_f$ could also be used as a perturbation parameter, as done by Rinaldi [22]. Though that would permit decoupling of the equations,

the resulting solution would still be limited to the case $\alpha \to 0$. The parameter ε is related to the Langevin parameter, as can be shown using the following expression for the initial susceptibility [1]

$$\chi_i = \frac{\pi \phi \mu_0 M_d^2 d^3}{18 k_B T}, \tag{2.28}$$

the Brownian relaxation time, Eqn. (2.10), and vortex viscosity, Eqn. (2.5), obtaining

$$\varepsilon = \frac{2}{3} \frac{\alpha^2}{\left|\tilde{\mathbf{H}}\right|^2}. \tag{2.29}$$

Expanding the Langevin function in a power series of α and using Eqn. (2.29), the $\mathbf{M}_{eq}$ term can be expressed as a function of the perturbation parameter

$$\frac{\mathbf{M}_{eq}}{\chi_i K} = \tilde{\mathbf{H}} \left(1 - \frac{\varepsilon}{10} \left|\tilde{\mathbf{H}}\right|^2 + \frac{\varepsilon^2}{70} \left|\tilde{\mathbf{H}}\right|^4 + \mathcal{O}(\varepsilon^3) \right). \tag{2.30}$$

Equation (2.30) is now substituted in Eqn. (2.24) to obtain

$$\tilde{\Omega}_f \frac{\partial \tilde{\mathbf{M}}}{\partial \tilde{t}} + \tilde{\Omega}_f \varepsilon \tilde{\mathbf{v}} \cdot \tilde{\boldsymbol{\nabla}} \tilde{\mathbf{M}} = \tilde{\Omega}_f \varepsilon \tilde{\boldsymbol{\omega}} \times \tilde{\mathbf{M}} - \tilde{\mathbf{M}} + \tilde{\mathbf{H}} \left(1 - \frac{\varepsilon}{10} \left|\tilde{\mathbf{H}}\right|^2 + \frac{\varepsilon^2}{70} \left|\tilde{\mathbf{H}}\right|^4 + O(\varepsilon^3) \right). \tag{2.31}$$

Thus, choosing ε as the perturbation parameter allows decoupling of the equations as well as considering the effects of non-negligible magnetic fields.

2.7 Zeroth order problem

In order to apply the regular perturbation method we expand all field quantities in powers of the parameter ε and group coefficients of like powers of ε to obtain the set of equations for each order of the problem. The corresponding set of equations for the zeroth order problem are

$$\tilde{\boldsymbol{\nabla}} \times \tilde{\mathbf{H}}_0 = 0, \tag{2.32}$$

$$\tilde{\boldsymbol{\nabla}} \cdot \left(\chi_i \tilde{\mathbf{M}}_0 + \tilde{\mathbf{H}}_0 \right) = 0, \tag{2.33}$$

$$\tilde{\Omega}_f \frac{\partial \tilde{\mathbf{M}}_0}{\partial \tilde{t}} = \tilde{\mathbf{H}}_0 - \tilde{\mathbf{M}}_0, \tag{2.34}$$

$$\mathbf{0} = \frac{\zeta}{\tilde{\Omega}_f \eta} \tilde{\mathbf{M}}_0 \cdot \tilde{\boldsymbol{\nabla}} \tilde{\mathbf{H}}_0 - \tilde{\boldsymbol{\nabla}} \tilde{p}_0 + \frac{2\zeta}{\eta} \tilde{\boldsymbol{\nabla}} \times \tilde{\boldsymbol{\omega}}_0 + \frac{\eta_e}{\zeta} \tilde{\boldsymbol{\nabla}}^2 \tilde{\mathbf{v}}_0, \tag{2.35}$$

$$\mathbf{0} = \frac{1}{\tilde{\Omega}_f} \tilde{\mathbf{M}}_0 \times \tilde{\mathbf{H}}_0 + 2\tilde{\boldsymbol{\nabla}} \times \tilde{\mathbf{v}}_0 - 4\tilde{\boldsymbol{\omega}}_0 + \frac{4\eta}{\eta_e \kappa^2} \tilde{\boldsymbol{\nabla}}^2 \tilde{\boldsymbol{\omega}}. \tag{2.36}$$

As can be seen, the zeroth order magnetic field and magnetization can be solved independently of the hydrodynamic problem.

2.7.1 Zeroth order magnetic field and magnetization

We assume the magnetic field and magnetization have a functional form similar to Eqn. (2.2) with $m = 1$

$$\tilde{\mathbf{H}}_0 \left(\tilde{r}, \theta, \tilde{t}\right) = \mathrm{Re}\left\{ \left[\hat{H}_{r,0}(\tilde{r}) \mathbf{i}_r + \hat{H}_{\theta,0}(\tilde{r}) \mathbf{i}_\theta \right] e^{j\left(\tilde{t} - \theta\right)} \right\}, \tag{2.37}$$

$$\tilde{\mathbf{M}}_0 \left(\tilde{r}, \theta, \tilde{t}\right) = \mathrm{Re}\left\{ \left[\hat{M}_{r,0}(\tilde{r}) \mathbf{i}_r + \hat{M}_{\theta,0}(\tilde{r}) \mathbf{i}_\theta \right] e^{j\left(\tilde{t} - \theta\right)} \right\}, \tag{2.38}$$

where the hat denotes a complex-amplitude quantity. Using Eqn. (2.38) in Eqn. (2.34) we obtain expressions for the zeroth order magnetization components as a function of the zeroth order components of the magnetic field,

$$\hat{M}_{\theta,0}\left(\tilde{r}\right) = \frac{\hat{H}_{\theta,0}}{1 + j\tilde{\Omega}}, \;\; \hat{M}_{r,0}\left(\tilde{r}\right) = \frac{\hat{H}_{r,0}}{1 + j\tilde{\Omega}}. \tag{2.39}$$

Now, substituting this in Eqn. (2.33) and using Eqn. (2.32), we obtain the following system of differential equations for the azimuthal and radial components of the magnetic field

$$\frac{d\left(\tilde{r}\hat{H}_{\theta,0}\right)}{d\tilde{r}} + j\hat{H}_{r,0} = 0, \tag{2.40}$$

$$\frac{d\left(\tilde{r}\hat{H}_{r,0}\right)}{d\tilde{r}} = j\hat{H}_{\theta,0}, \tag{2.41}$$

with solution given by,

$$\hat{H}_{r,0} = C_{1,0} + C_{2,0}\tilde{r}^{-2}, \tag{2.42}$$

$$\hat{H}_{\theta,0} = -j\left(C_{1,0} - C_{2,0}\tilde{r}^{-2}\right). \tag{2.43}$$

Because the solution range includes $\tilde{r} = 0$, the constant $C_{2,0}$ must be zero, so that the magnetic field remains finite at the origin. The constant $C_{1,0}$ is obtained using the tangential jump condition, Eqn. (2.14), written in dimensionless form

$$\hat{H}_{\theta,0}(\tilde{r} = 1) = -1. \tag{2.44}$$

The resulting expressions for the complex amplitudes of the zeroth order magnetic field are

$$\hat{H}_{r,0} = -j, \quad \hat{H}_{\theta,0} = -1. \tag{2.45}$$

This result demonstrates that the zeroth order magnetic field is uniform in the cylinder gap.

2.7.2 Zeroth order magnetic body force and body couple

Using the expressions for the zeroth order magnetization (2.39) and magnetic field (2.45) we obtain expressions for the magnetic body force and magnetic body couple. Since the zeroth order magnetic field is uniform, the magnetic body force $\tilde{\mathbf{M}}_0 \cdot \tilde{\boldsymbol{\nabla}}\tilde{\mathbf{H}}_0$ is clearly zero. The zeroth order body couple is,

$$\tilde{l}_{z,0} = \left(\tilde{\mathbf{M}}_0 \times \tilde{\mathbf{H}}_0\right)_z = \frac{\tilde{\Omega}_f}{1 + \tilde{\Omega}_f^2}. \tag{2.46}$$

2.7.3 Zeroth order linear and spin velocity fields

The zeroth order magnetic body force is zero, whereas the zeroth order body couple is constant. Thus, to obtain the linear and spin velocity fields, we solve the linear and internal angular momentum Eqns. (2.35) and (2.36), assuming steady flow in axisymmetric cylindrical coordinates. The resulting equations governing $\tilde{v}_{\theta,0}(\tilde{r})$ and $\tilde{\omega}_{z,0}(\tilde{r})$ are the azimuthal component of the zeroth order linear momentum,

$$\frac{\eta_e}{\eta}\frac{d}{d\tilde{r}}\left[\frac{1}{\tilde{r}}\frac{d\left(\tilde{r}\tilde{v}_{\theta,0}\right)}{d\tilde{r}}\right] - \frac{2\zeta}{\eta}\frac{d\tilde{\omega}_{z,0}}{d\tilde{r}} = 0, \tag{2.47}$$

and the z-component of the zeroth order internal angular momentum

$$\frac{1}{\tilde{r}}\frac{d}{d\tilde{r}}\left(\tilde{r}\frac{d\tilde{\omega}_{z,0}}{d\tilde{r}}\right)\frac{4\eta}{\eta_e\kappa^2}+\frac{2}{\tilde{r}}\frac{d\left(\tilde{r}\tilde{v}_{\theta,0}\right)}{d\tilde{r}}-4\tilde{\omega}_{z,0}+\frac{1}{1+\tilde{\Omega}_f^2}=0. \tag{2.48}$$

In order to solve for $\tilde{v}_{\theta,0}(\tilde{r})$ and $\tilde{\omega}_{z,0}(\tilde{r})$, we introduce the vorticity $\tilde{\Omega}_{z,0}$ of the zeroth order translational velocity in Eqn. (2.47) to obtain

$$\frac{d}{d\tilde{r}}\left(\frac{\eta_e}{\eta}\tilde{\Omega}_{z,0}-\frac{2\zeta}{\eta}\tilde{\omega}_{z,0}\right)=0, \tag{2.49}$$

and then carry out the integration to yield an expression for the zeroth order vorticity

$$\tilde{\Omega}_{z,0}=\frac{2\zeta}{\eta_e}\tilde{\omega}_{z,0}+\frac{\eta}{\eta_e}C_1, \tag{2.50}$$

which we replace in Eqn. (2.48) to yield a nonhomogeneous modified Bessel equation of order zero for the z-component of spin velocity

$$\frac{1}{\tilde{r}}\frac{d}{d\tilde{r}}\left(\tilde{r}\frac{d\tilde{\omega}_{z,0}}{d\tilde{r}}\right)-\kappa^2\tilde{\omega}_{z,0}=-\frac{\kappa^2}{2}C_1-\frac{\eta_e\kappa^2}{4\eta\left(1+\tilde{\Omega}_f^2\right)}. \tag{2.51}$$

The corresponding solution is,

$$\tilde{\omega}_{z,0}(\tilde{r})=\frac{C_1}{2}+C_2I_0\left(\kappa\tilde{r}\right)+\frac{\eta_e}{4\eta\left(1+\tilde{\Omega}_f^2\right)}, \tag{2.52}$$

where $I_0\left(\mathbf{x}\right)$, is the modified Bessel function of first kind, order zero. The constant that accompanies the modified Bessel function of the second kind of order zero, $K_0\left(\mathbf{x}\right)$, has been fixed equal to zero so that the solution remains finite at $\tilde{r}=0$. Using Eqn. (2.52) in Eqn. (2.50) and integrating, we can determine the zeroth order translational velocity. The expressions for the constants C_1 and C_2 were determined using the boundary conditions (2.15) and (2.16) to

obtain

$$\tilde{\omega}_{z,0}(\tilde{r}) = \frac{1}{4\eta^* \left(1+\tilde{\Omega}_f^2\right)} \left\{ \eta_e \left[1 - \frac{I_0\left(\kappa\tilde{r}\right)}{I_0\left(\kappa\right)} \right] - \gamma\zeta \frac{I_2\left(\kappa\right)}{I_0\left(\kappa\right)} \right\}, \tag{2.53}$$

$$\tilde{v}_{\theta,0}(\tilde{r}) = \frac{\zeta}{2\kappa\eta^* \left(1+\tilde{\Omega}_f^2\right)} \frac{I_1\left(\kappa\right)}{I_0\left(\kappa\right)} \left(\tilde{r} - \frac{I_0\left(\kappa\tilde{r}\right)}{I_1\left(\kappa\right)} \right). \tag{2.54}$$

In (2.53) and (2.54) we have defined the parameter η^* as

$$\eta^* \equiv \eta - \zeta\left(\gamma - 1\right) \frac{I_2\left(\kappa\right)}{I_0\left(\kappa\right)}. \tag{2.55}$$

The linear and spin velocity fields are intimately related to the value of κ and therefore to the value of the spin viscosity η'. As $\eta' \to 0$, $\kappa \to \infty$ and the translational velocity tends to zero whereas the spin velocity becomes uniform in the gap. Comparison between Eqn. (2.54) and the expression reported by [19], shows that our zeroth order analysis corresponds to the spin diffusion result, albeit allowing a more general boundary condition for the spin velocity.

2.8 First order problem

The set of equations for the first order problem are obtained using the same procedure as for the zeroth order problem, resulting in

$$\tilde{\nabla} \times \tilde{\mathbf{H}}_1 = \mathbf{0}, \tag{2.56}$$

$$\tilde{\nabla} \cdot \left(\chi_i \tilde{\mathbf{M}}_1 + \tilde{\mathbf{H}}_1 \right) = \mathbf{0}, \tag{2.57}$$

$$\tilde{\Omega}_f \frac{\partial \tilde{\mathbf{M}}_1}{\partial \tilde{t}} + \tilde{\Omega}_f \tilde{\mathbf{v}}_0 \cdot \tilde{\nabla} \tilde{\mathbf{M}}_0 \ = \tilde{\Omega}_f \left(\tilde{\boldsymbol{\omega}}_0 \times \tilde{\mathbf{M}}_0 \right) - \tilde{\mathbf{M}}_1 + \tilde{\mathbf{H}}_1 - \frac{\tilde{\mathbf{H}}_0}{10} \left| \tilde{\mathbf{H}}_0 \right|^2, \tag{2.58}$$

$$\mathbf{0} = \frac{\zeta}{\eta \tilde{\Omega}_f} \left(\tilde{\mathbf{M}}_0 \cdot \tilde{\nabla} \tilde{\mathbf{H}}_1 + \tilde{\mathbf{M}}_1 \cdot \tilde{\nabla} \tilde{\mathbf{H}}_0 \right) - \tilde{\nabla} \tilde{p}_1 + \frac{2\zeta}{\eta} \tilde{\nabla} \times \tilde{\boldsymbol{\omega}}_1 + \frac{\eta_e}{\zeta} \tilde{\nabla}^2 \tilde{\mathbf{v}}_1, \tag{2.59}$$

$$\mathbf{0} = \frac{1}{\tilde{\Omega}_f} \left(\tilde{\mathbf{M}}_0 \times \tilde{\mathbf{H}}_1 + \tilde{\mathbf{M}}_1 \times \tilde{\mathbf{H}}_0 \right) + 2\tilde{\nabla} \times \tilde{\mathbf{v}}_1 - 4\tilde{\boldsymbol{\omega}}_1 + \frac{4\eta}{\eta_e \kappa^2} \tilde{\nabla}^2 \tilde{\boldsymbol{\omega}}_1. \tag{2.60}$$

In the same form as for the zeroth order problem the magnetic field and magnetization can be obtained independently of the hydrodynamic problem. The solution strategy will be similar to the zeroth order problem.

2.8.1 First order magnetic field and magnetization

In the first order magnetization relaxation Eqn. (2.58) it is clear that the second term of the left-hand-side is zero owing to the uniformity of the zeroth order magnetic field, whereas the norm of the zeroth order magnetic field equals unity

$$\left|\tilde{\mathbf{H}}_0\right| = 1. \tag{2.61}$$

We obtain the components of the first order magnetization from Eqn. (2.58)

$$\hat{M}_{r,1}=\frac{1}{1+j\tilde{\Omega}_f}\left[\hat{H}_{r,1}-\tilde{\Omega}\hat{\omega}_{z,0}\hat{M}_{\theta,0}-\frac{\hat{H}_{r,0}}{10}\right], \tag{2.62}$$

$$\hat{M}_{\theta,1}=\frac{1}{1+j\tilde{\Omega}_f}\left[\hat{H}_{\theta,1}+\tilde{\Omega}\hat{\omega}_{z,0}\hat{M}_{r,0}-\frac{\hat{H}_{\theta,0}}{10}\right]. \tag{2.63}$$

Using Eqns. (2.62) and (2.63) together with Eqns. (2.56) and (2.57), we obtain a system of equations similar to (2.40) and (2.41), however, in this case the flux continuity equation has a forcing function that involves the radial derivative of the z-directed component of spin velocity. This system of equations can be reduced to an equidimensional differential equation with a Bessel forcing function for the azimuthal component of the magnetic field,

$$\frac{d}{d\tilde{r}}\left[\tilde{r}\frac{d\left(\tilde{r}\hat{H}_{\theta,1}\right)}{d\tilde{r}}\right]-j\hat{H}_{\theta,1}=\hat{A}\tilde{r}I_1\left(\kappa\tilde{r}\right) \tag{2.64}$$

where $\hat{A}$ has been defined as

$$\hat{A}\equiv\frac{\eta_e\kappa\chi_i\tilde{\Omega}_f}{4\eta^*\left(1+\chi_i+j\tilde{\Omega}_f\right)\left(\tilde{\Omega}_f-j\right)^2\left(j+\tilde{\Omega}_f\right)I_0\left(\kappa\right)}. \tag{2.65}$$

The particular solution can be determined using the method of variation of parameters. The

solution for the azimuthal and radial components of the magnetic field are

$$\hat{H}_{\theta,1}(\tilde{r}) = \frac{\hat{A}}{\kappa^2}\left[\frac{I_1(\kappa\tilde{r})}{\tilde{r}} - I_1(\kappa)\right], \tag{2.66}$$

$$\hat{H}_{r,1}(\tilde{r}) = j\frac{\hat{A}}{2\kappa}\left[I_0(\kappa\tilde{r}) + I_2(\kappa\tilde{r}) - \frac{2I_1(\kappa)}{\kappa}\right]. \tag{2.67}$$

In Eqn. (2.66), it can be shown that the limit of $I_1(\kappa\tilde{r})/\tilde{r}$ when $\tilde{r}$ tends to zero is $\kappa/2$. Using Eqns. (2.66) and (2.67) in Eqns. (2.62) and (2.63) one can obtain the components of the first order magnetization.

2.8.2 First order magnetic body force and body couple

The first order magnetic body force is

$$\tilde{\mathbf{f}}_1(\mathbf{x}) = \tilde{\mathbf{M}}_0 \cdot \tilde{\nabla}\tilde{\mathbf{H}}_1 + \tilde{\mathbf{M}}_1 \cdot \tilde{\nabla}\tilde{\mathbf{H}}_0. \tag{2.68}$$

Owing to the homogeneity of the zeroth order magnetic field, the second term of (2.68) is clearly zero. As can be shown by taking the curl of this equation, and using the fact that the zeroth order magnetic field is uniform, the first order body force is potential

$$\tilde{\nabla} \times \tilde{\mathbf{f}}_1(\mathbf{x}) = \tilde{\nabla} \times \left(\tilde{\mathbf{M}}_0 \cdot \tilde{\nabla}\tilde{\mathbf{H}}_1\right) = \tilde{\mathbf{M}}_0 \cdot \tilde{\nabla}\left(\tilde{\nabla} \times \tilde{\mathbf{H}}_1\right) = \mathbf{0}, \tag{2.69}$$

and can be expressed as the gradient of a scalar field $\mathbf{f}(\mathbf{x}) = -\nabla\varphi$. This is relevant as a potential magnetic force not does result in macroscopic flow [61].

The first order body couple is given by

$$\tilde{\mathbf{l}}_1(\mathbf{x}) = \tilde{\mathbf{M}}_0 \times \tilde{\mathbf{H}}_1 + \tilde{\mathbf{M}}_1 \times \tilde{\mathbf{H}}_0, \tag{2.70}$$

which can be shown to have the form

$$\tilde{l}_{z,1}(\tilde{r}) = B + GI_0(\kappa\tilde{r}), \tag{2.71}$$

where the constants B and G are defined as

$$B \equiv (\gamma\zeta - \eta_e)\frac{\left(7-\tilde{\Omega}_f^2+2\tilde{\Omega}_f^4\right)\tilde{\Omega}_f}{20\eta^*\left(1+\tilde{\Omega}_f^2\right)^3} - 2\tilde{\Omega}_f I_1(\kappa) \tag{2.72}$$

$$\frac{5\eta_e\chi_i(2+\chi_i)\tilde{\Omega}_f^2+\zeta\left[(1+\chi_i)^2+\tilde{\Omega}_f^2\right]\left[7\gamma-2-(4+\gamma)\tilde{\Omega}_f^2+2(\gamma-1)\tilde{\Omega}_f^4\right]}{20\eta^*\kappa\left(1+\tilde{\Omega}_f^2\right)^3\left[(1+\chi_i)^2+\tilde{\Omega}_f^2\right]I_0(\kappa)}, \tag{2.73}$$

$$G \equiv \frac{\eta_e\tilde{\Omega}_f\left[(1+\chi_i)^2-\tilde{\Omega}_f^4\right]}{4\eta^*\left(1+\tilde{\Omega}_f^2\right)^3\left[(1+\chi_i)^2+\tilde{\Omega}_f^2\right]I_0(\kappa)}. \tag{2.74}$$

2.8.3 First order linear and spin velocity fields

To solve the internal angular and linear momentum equations we use the same procedure as for the zeroth order problem to obtain the following non-homogeneous modified Bessel differential equation with Bessel forcing function for the spin velocity,

$$\frac{1}{\tilde{r}}\frac{d}{d\tilde{r}}\left(\tilde{r}\frac{d\tilde{\omega}_{z,1}}{d\tilde{r}}\right)-\kappa^2\tilde{\omega}_{z,1} = -\frac{\kappa^2}{2}C_1 - \frac{\eta_e\kappa^2}{4\eta\tilde{\Omega}_f}\left[B+I_0(\kappa\tilde{r})G\right], \tag{2.75}$$

with particular solution given by

$$\tilde{\omega}_{z,1}(\tilde{r}) = \frac{C_1}{2}+C_2I_0(\kappa\tilde{r})+\frac{\eta_e}{4\eta\tilde{\Omega}_f}\left[B-\frac{\kappa}{2}\tilde{r}I_1(\kappa\tilde{r})G\right]. \tag{2.76}$$

Using (2.76), the first order vorticity is obtained and then upon integration the first order azimuthal component of velocity. The constants C_1 and C_2 were determined from the first order no-slip boundary condition for the velocity and the first order spin velocity boundary condition. Substituting, C_1 and C_2 in Eqn. (2.76), one obtains expressions for the z-directed spin velocity,

$$\begin{aligned}\tilde{\omega}_{z,1}(\tilde{r}) = \frac{1}{8\eta\eta^*\tilde{\Omega}_fI_0(\kappa)}\Big\{&2\zeta(\gamma\zeta-\eta_e)\left[I_1(\kappa)^2G+I_2(\kappa)B\right]\\ &+\eta_eI_0(\kappa\tilde{r})\left[-2\eta B+(\eta_e-\gamma\zeta)\kappa I_1(\kappa)G+2\zeta(\gamma-1)I_2(\kappa)G\right]+\\ &I_0(\kappa)\left[\eta_e\eta^*\left(2B-\tilde{r}I_1(\kappa\tilde{r})\kappa G\right)+2\zeta(\eta_e-\gamma\zeta)I_2(\kappa)G\right]\Big\},\end{aligned} \tag{2.77}$$

and azimuthal-component of the linear velocity

$$\tilde{v}_{\theta,1}(\tilde{r}) = \frac{\zeta}{4\eta\tilde{\Omega}_f}\left\{\frac{I_1(\kappa\tilde{r})\left[-2\eta B + (\eta_e - \gamma\zeta)\,\kappa I_1(\kappa)\,G + 2\zeta(\gamma-1)\,I_2(\kappa)\,G\right] + B}{\eta^*\kappa I_0(\kappa)} - \frac{G}{\eta^*\kappa}\right.$$
$$\left. + \frac{\tilde{r}(\gamma\zeta - \eta_e)\left\{I_1(\kappa)^2 G + I_2(\kappa)\left[B - I_0(\kappa)\,G\right]\right\}}{\eta^* I_0(\kappa)} + \tilde{r}\left[B - I_2(\kappa\tilde{r})\,G\right]\right\}. \quad (2.78)$$

2.9 Second order problem

The second order magnetization equation is

$$\tilde{\Omega}_f\frac{\partial\tilde{\mathbf{M}}_2}{\partial\tilde{t}} + \tilde{\Omega}_f\left(\tilde{\mathbf{v}}_0\cdot\tilde{\boldsymbol{\nabla}}\tilde{\mathbf{M}}_1 + \tilde{\mathbf{v}}_1\cdot\tilde{\boldsymbol{\nabla}}\tilde{\mathbf{M}}_0\right) =$$
$$\tilde{\Omega}_f\left(\tilde{\boldsymbol{\omega}}_0\times\tilde{\mathbf{M}}_1 + \tilde{\boldsymbol{\omega}}_1\times\tilde{\mathbf{M}}_0\right) - \tilde{\mathbf{M}}_2 + \tilde{\mathbf{H}}_2 - \frac{\tilde{\mathbf{H}}_1}{10}\left|\tilde{\mathbf{H}}_0\right|^2$$
$$+ \frac{\tilde{\mathbf{H}}_0}{70}\left(\tilde{H}_{r,0}^4 + \tilde{H}_{\theta,0}^4\right) - \frac{\tilde{\mathbf{H}}_0}{5}\left(\tilde{H}_{r,0}\tilde{H}_{r,1} + \tilde{H}_{\theta,0}\tilde{H}_{\theta,1}\right) + \frac{\tilde{\mathbf{H}}_0}{35}\tilde{H}_{r,0}^2\tilde{H}_{\theta,0}^2. \quad (2.79)$$

In equation (2.79), the fifth, sixth, and seventh terms on the right hand side correspond to the ε^2 terms of equation (2.30). These terms are equivalent to

$$\tilde{\mathbf{H}}_0\left(\tilde{H}_{r,0}^4 + \tilde{H}_{\theta,0}^4\right) = 2\left[\sin(5t-5\theta)\,\mathbf{i}_r - \cos(5t-5\theta)\,\mathbf{i}_\theta\right], \quad (2.80)$$

$$\tilde{\mathbf{H}}_0\left(\tilde{H}_{r,0}\tilde{H}_{r,1} + \tilde{H}_{\theta,0}\tilde{H}_{\theta,1}\right) = \frac{1}{\tilde{r}\kappa^2}\left\{\left[b\kappa\tilde{r}I_0(\kappa\tilde{r}) + (a-b)\,\tilde{r}I_1(\kappa) - (a+b)\,I_1(\kappa\tilde{r})\right]\cos(3t-3\theta)\right.$$
$$\left. + \left[a\tilde{r}\kappa I_0(\kappa\tilde{r}) - (a+b)\,\tilde{r}I_1(\kappa) + (-a+b)\,I_1(\kappa\tilde{r})\right]\sin(3t-3\theta)\right\}\mathbf{i}_r +$$
$$\frac{1}{\tilde{r}\kappa^2}\left\{\left[b\tilde{r}\kappa I_0(\kappa\tilde{r}) + (a-b)\,\tilde{r}I_1(\kappa) - (a+b)\,I_1(\kappa\tilde{r})\right]\cos(3t-3\theta) +\right.$$
$$\left.\left[a\tilde{r}\kappa I_0(\kappa\tilde{r}) - (a+b)\,\tilde{r}I_1(\kappa) + (-a+b)\,I_1(\kappa\tilde{r})\right]\sin(3t-3\theta)\right\}\mathbf{i}_\theta \quad (2.81)$$

$$\tilde{\mathbf{H}}_0\tilde{H}_{r,0}^2\tilde{H}_{\theta,0}^2 = \left[-\sin(5t-5\theta)\,\mathbf{i}_r + \cos(5t-5\theta)\,\mathbf{i}_\theta\right]. \quad (2.82)$$

where

$$a = -\frac{\chi_i \eta_e \kappa^2 \tilde{\Omega}_f^2 \left(2+\chi_i\right)}{4\eta^* \left(1+\tilde{\Omega}_f^2\right)^2 \left[\tilde{\Omega}_f^2 + \left(1+\chi_i\right)^2\right] \kappa I_0\left(\kappa\right)} \tag{2.83}$$

$$b = -\frac{\chi_i \eta_e \kappa^2 \tilde{\Omega}_f \left(1+\chi_i-\tilde{\Omega}_f^2\right)}{4\eta^* \left(1+\tilde{\Omega}_f^2\right)^2 \left[\tilde{\Omega}_f^2 + \left(1+\chi_i\right)^2\right] \kappa I_0\left(\kappa\right)} \tag{2.84}$$

The contributions due to the first and seventh terms of Eqn. (2.79) cancel, as seen from Eqns. (2.80) and (2.82). From Eqn. (2.81) one finds that the fundamental and third harmonics of the applied field will have to be considered in solving for the second order magnetic fields. This will require assuming the following functional forms for the magnetic field and magnetization

$$\tilde{\mathbf{H}} = \mathrm{Re}\left\{\hat{H}_1^1 e^{j\left(\Omega_f \tilde{t}-\theta\right)} + \hat{H}_2^3 e^{j\left(3\Omega_f \tilde{t}-3\theta\right)}\right\}, \tag{2.85}$$

$$\tilde{\mathbf{M}} = \mathrm{Re}\left\{\hat{M}_1^1 e^{j\left(\Omega_f \tilde{t}-\theta\right)} + \hat{M}_2^3 e^{j\left(3\Omega_f \tilde{t}-3\theta\right)}\right\}. \tag{2.86}$$

Thus two magnetic fields problems will have to be solved to obtain the second order force and couple. While this is not difficult, it is lengthy and tedious and we therefore leave our solution at the first order.

2.10 Range of applicability of the analysis

The solution obtained using a regular perturbation method is valid only for small values of the perturbation parameter $\varepsilon \ll 1$. In this case it is expected that a good approximation can be obtained with only a few terms in the perturbation series [62]. However, it is necessary to know how many terms are necessary for a valid level of approximation. Fig. 2-2 shows the perturbation parameter plotted for several orders of the analysis as a function of the amplitude of the applied magnetic field and using the properties of the EMG705 ferrofluid. Thus, for amplitudes of the applied magnetic field $H > 1\,\mathrm{mT}$ corrections terms of $\mathcal{O}\left(\alpha^2\right)$ are relevant in obtaining a good approximation. However, it is important to note that the leading term (zeroth order solution) reveals the more important characteristics of the flow, whereas remaining terms give small corrections to the solution.

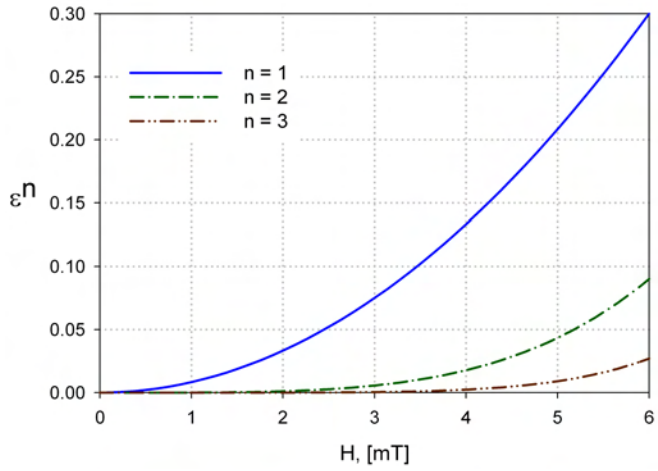

Figure 2-2: Perturbation parameter as a function of the applied magnetic field. In order to obtain predictions for applied magnetic fields of approximately 5 mT correction terms $\mathcal{O}\left(\varepsilon^3\right)$ will be needed.

In addition, analyses such as Zaitsev and Shliomis [19] assume that the $\mathbf{M}_{eq} \approx \chi_i \mathbf{H}$. This is equivalent to assuming that the Langevin function ($L(\alpha)$ in Eqn. (2.8)) is approximated using only the first term $\mathcal{O}(\alpha)$ of a power series. Nevertheless, the first order contribution considers up to the second order of the power series, thus correction terms up to $\mathcal{O}\left(\alpha^3\right)$ are included in the analysis. Fig. 2-3 describes this behaviour, indicating that deviations of the $\mathbf{M}_{eq}$ are observed for values of $\alpha > 0.3$ for the first order analysis whereas for the second order deviations are observed for $\alpha > 0.8$.

2.11 Predictions of the analysis

The predicted translational and spin velocity from the asymptotic analysis are shown in Figs. 2-4 and 2-5. These were obtained using the properties of the EMG705 ferrofluid given in Table 4.1 and 4.3. Because there are no measurements or rigorous estimates for the spin viscosity we have arbitrarily chosen the value $\kappa = 100$ to illustrate the general features of the solution. In Chapter 5, we will consider this matter further and attempt to estimate a value for κ based on our experiments. The analysis predicts, for zeroth order, a rigid-body-like azimuthal velocity

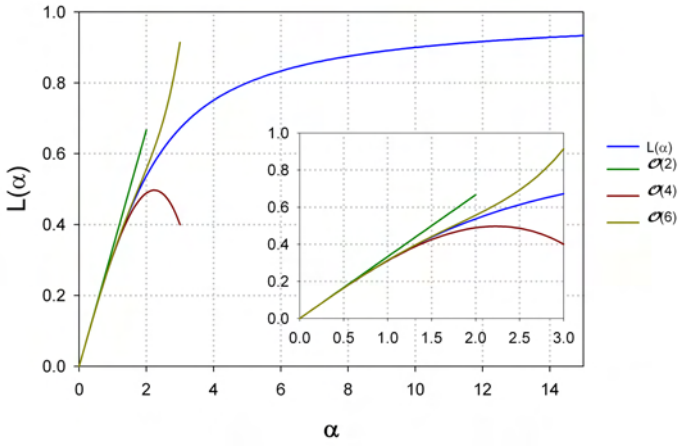

Figure 2-3: Plot of $L(\alpha) = \coth(\alpha) - \alpha^{-1}$ and its approximations obtained from a power series expansion truncated to $\mathcal{O}(\alpha^2)$, $\mathcal{O}(\alpha^4)$, and $\mathcal{O}(\alpha^6)$, versus α. This figure shows that in previous analysis deviations of the $\mathbf{M}_{eq}$ are observed for $\alpha > 0.8$.

profile co-rotating with the field through most of the fluid and decreasing to zero near the container wall in a thin layer whose thickness depends on the dimensionless parameter κ and as a result on the value of the spin viscosity η'. The first order analysis predicts flow opposite to field rotation possibly due to the effect of the spin-magnetization coupling term $\boldsymbol{\omega}(\mathbf{x}) \times \mathbf{M}(\mathbf{x})$ of the magnetization equation. However, it is likely that in contributions of higher order, correction terms of even order yield co-rotation between flow and field whereas counter rotation will be obtained for terms of odd order in similar fashion to the case studied in [22]. Thus, the net effect of higher order terms will be flow retardation and not a change in flow direction.

Figure 2-6 shows the effect on the translational velocity profile of the γ coefficient in the generalized spin boundary condition, Eqn. (2.16). These velocity profiles were obtained using $\kappa = 10$ to emphasize the effect of γ. As can be observed, there is a small effect only on the magnitude of the flow because all other figures were obtained assuming $\gamma = 0$.

Figure 2-7 shows the effect of the parameter κ for translational velocity profiles which is in agreement with the fact that no flow is predicted when $\eta' \to 0$ or $\kappa \to \infty$. Fig. 2-8 illustrates the effect of the magnetic field amplitude on the magnitude of the flow. This theoretical analysis also predicts an increase of the rotation rate of the fluid with decreasing container radius up to

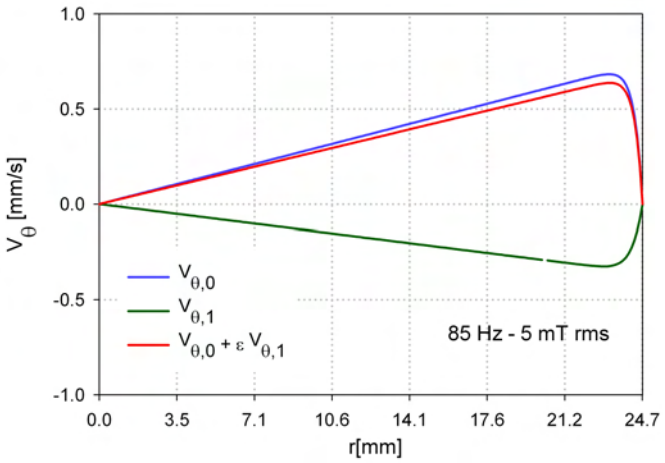

Figure 2-4: Theoretical translational velocity profile for zeroth, first, and composite asymptotic solution obtained from regular perturbation, with $\varepsilon = 0.162$, and using ferrofluid properties for EMG705.

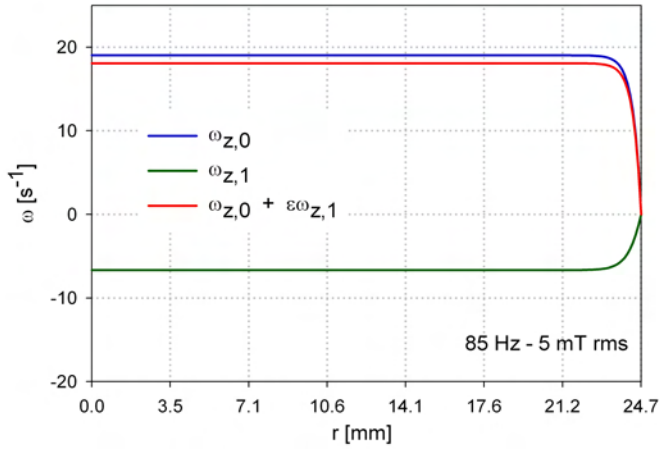

Figure 2-5: Theoretical spin velocity profile for zeroth, first, and composite asymptotic solution obtained from regular perturbation method, with $\varepsilon = 0.162$, and using ferrofluids properties of the EMG705.

a radius which depends on κ, below which the rotation rate decreases to zero, as shown in Fig. 2-9. Similar behavior was observed experimentally by Rosensweig [17] for free surface flow in a cylindrical container for which the external radius was changed between 40 to 5 mm. A more complete comparison with experimental velocity profiles will is presented in the Chapter 5.

2.12 Torque on the cylindrical container

Having obtained the translational and spin velocity fields we proceed to derive an expression for the torque on the surface of the cylinder. The hydrodynamic torque on the container is given by

$$L_O = \oint_s d\mathbf{S} \cdot (-\mathbf{T} \times \mathbf{r} + \mathbf{C}). \tag{2.87}$$

where $\mathbf{T}$ is the stress tensor with a symmetric Newtonian part and an asymmetric part whose phenomenological form was presented by Condiff and Dahler [36]

$$\mathbf{T} = -p\mathbf{I} + \eta \left[\boldsymbol{\nabla}\mathbf{v} + \boldsymbol{\nabla}\mathbf{v}^T\right] + \lambda \left(\boldsymbol{\nabla} \cdot \mathbf{v}\right) \mathbf{I} + \zeta\epsilon \cdot \left(\boldsymbol{\nabla} \times \mathbf{v} - 2\boldsymbol{\omega}\right). \tag{2.88}$$

In (2.88), $\mathbf{I}$ is the unit tensor, p is the pressure, and ϵ is the alternating unit tensor. Further, $\mathbf{C}$ is the surface couple stress tensor representing the diffusive transport of internal angular momentum between contiguous material elements [34] with constitutive form

$$\mathbf{C} = \eta' \left[\boldsymbol{\nabla}\boldsymbol{\omega} + \boldsymbol{\nabla}\boldsymbol{\omega}^T\right] + \lambda \left(\boldsymbol{\nabla} \cdot \boldsymbol{\omega}\right) \mathbf{I}. \tag{2.89}$$

In addition to the expected viscous contributions to the torque, surface excess magnetic forces could also contribute to the measured torque. Surface excess forces arise as a consequence of the change in magnetization at the fluid-wall interface and can be determined by evaluating the jump in the Maxwell stress tensor across the wall-fluid interface

$$L_M = \mathbf{r} \times \left\| \mathbf{n} \cdot \mathbf{T}^{\mathbf{M}} \right\|. \tag{2.90}$$

In this, $\mathbf{r}$ is the position vector, $\mathbf{n}$ is the unit outward normal vector of the surface, which in our case is $\mathbf{i}_r$, and $\mathbf{T}^{\mathbf{M}}$ is the Maxwell stress tensor, which for an incompressible ferrofluid is

given by [1, 40, 55]

$$\mathbf{T}^M = \mathbf{BH} - \frac{1}{2}\mu_0 H^2 \mathbf{I}. \tag{2.91}$$

In (2.91), $\mathbf{B} = \mu_0 (\mathbf{H} + \mathbf{M})$. The azimuthal component of the surface excess magnetic force is relevant with respect to an axial torque and is given by:

$$f_\theta = (B_r H_\theta)|_{r=R_O^+} - (B_r H_\theta)|_{r=R_O^-}. \tag{2.92}$$

Using the continuity conditions for the normal magnetic flux and the tangential component of magnetic field intensity one obtains that

$$f_\theta = B_r \left(H_\theta|_{r=R_O^+} - H_\theta|_{r=R_O^-} \right) = 0, \tag{2.93}$$

showing that the surface excess magnetic force does not contribute to the torque. Returning to equation (2.87), an expression for the torque can be obtained by introducing the constitutive expressions for stress (2.88) and surface couple stress tensor (2.89) in equation (2.87) obtaining

$$L_O = \int_0^l \int_0^{2\pi} \left[\eta r^2 \frac{d}{dr}\left(\frac{v_\theta}{r}\right) + \zeta \frac{d}{dr}(r v_\theta) - 2\zeta r \omega_z + \eta \frac{d\omega_z}{dr} \right] r d\theta dz, \tag{2.94}$$

where l is the height of the cylinder. Introducing the scaled variables of equation (2.16) and carrying out the integration, we obtain the general dimensionless expression for torque on the inner surface of the cylinder

$$\tilde{L}_O = 2\chi_i \tilde{\Omega}_f \left[\frac{\eta}{\zeta} \tilde{r}^2 \frac{d}{d\tilde{r}}\left(\frac{\tilde{v}_\theta}{\tilde{r}}\right) + \frac{d}{d\tilde{r}}(\tilde{r}\tilde{v}_\theta) - 2\tilde{r}\tilde{\omega}_z + \frac{4\eta}{\eta_e \kappa^2} \frac{d\tilde{\omega}_z}{d\tilde{r}} \right]_{\tilde{r}=1} \tag{2.95}$$

where $\tilde{L}_O = L_O / \left(\mu_0 K^2 V_f\right)$ and V_f is the fluid volume. Expanding $\tilde{v}_\theta$ and $\tilde{\omega}_z$ in powers of the parameter ε and grouping coefficients of like powers we obtain the dimensionless z-directed torque

$$\tilde{L}_{O,z} = \frac{L_{O,z}}{\mu_0 K^2 V_f} = -\chi_i \left[\frac{\tilde{\Omega}}{1+\tilde{\Omega}^2} + \left(2B + \frac{G I_1(\kappa)}{\kappa} \right) \varepsilon \right] + \mathcal{O}\left(\varepsilon^2\right). \tag{2.96}$$

where B and G are given by equations (2.73) and (2.74) respectively. The expression for torque given in (2.96) takes into account contributions from anti-symmetric and couple stresses. In

order to quantify the magnitude of antisymmetric stresses, we take the limit of (2.96) when $\kappa \to \infty$, obtaining

$$\lim_{\kappa\to\infty} \tilde{L}_{O,z} = -\frac{\chi_i \tilde{\Omega}}{1+\tilde{\Omega}^2}\left[1 - \frac{\left(7-\tilde{\Omega}^2+2\tilde{\Omega}^4\right)}{20\left(1+\tilde{\Omega}^2\right)^2}\varepsilon\right] + \mathcal{O}\left(\varepsilon^2\right). \tag{2.97}$$

Comparison of Eqns. (2.96) and (2.97) will show that contributions due to antisymmetric stresses dominate the torque in a ferrofluid. These antisymmetric stresses are the result of the spin of the particles on the wall of the cylinder, as a consequence of magnetic body couples. This is verified below by comparison with the experimental torque measurements. In addition, the sole estimated parameter in Eqn. (2.97) is the relaxation time in $\tilde{\Omega} \equiv \Omega\tau$, suggesting that the agreement between the magnitude of the theoretical predictions and experimental measurements of torque will confirm that the relaxation time has been estimated correctly. Figure 2-10, show theoretical torque predictions of Eqn. (2.96) as function of amplitude and frequency of the magnetic field for EMG705 ferrofluid using $\kappa = 100$.

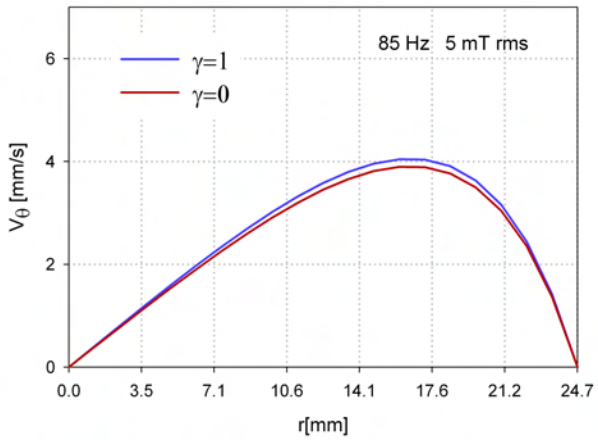

Figure 2-6: Effect of γ parameter on velocity profiles obtained using properties of the EMG700 for frequency of 85 Hz, amplitude of 5 mT for the applied magnetic field, and $\kappa = 10$.

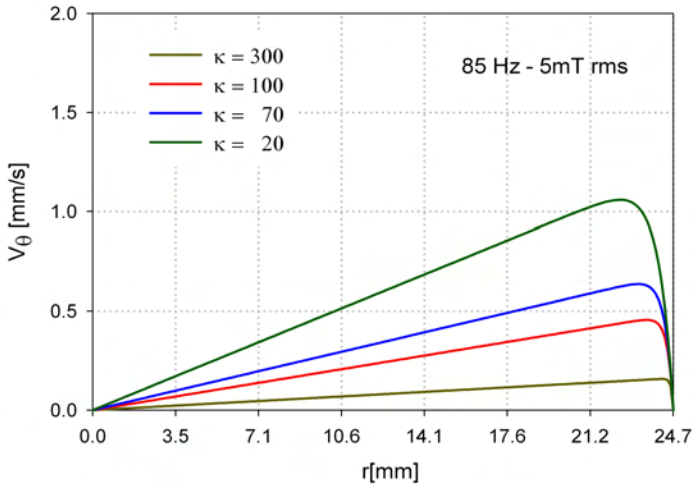

Figure 2-7: Effect of dimensionless parameter κ on maximun velocity position and flow magnitude predicted by composite solution of the regular perturbation method. This was obtained with EMG705 properties, and frequency of 85 Hz and amplitude of 5 mT for the applied magnetic field.

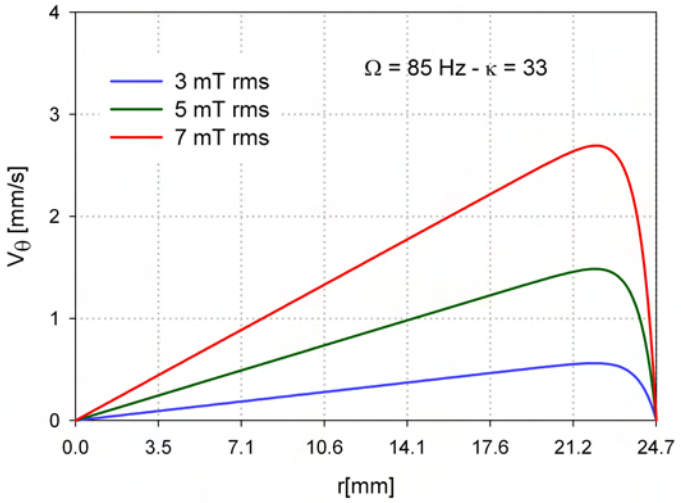

Figure 2-8: Dependence of the flow on magnitude of the magnetic field for a frequency of 85 Hz. These velocity profiles were obtained using the properties of the EMG900-1 ferrofluid and $\kappa = 33$.

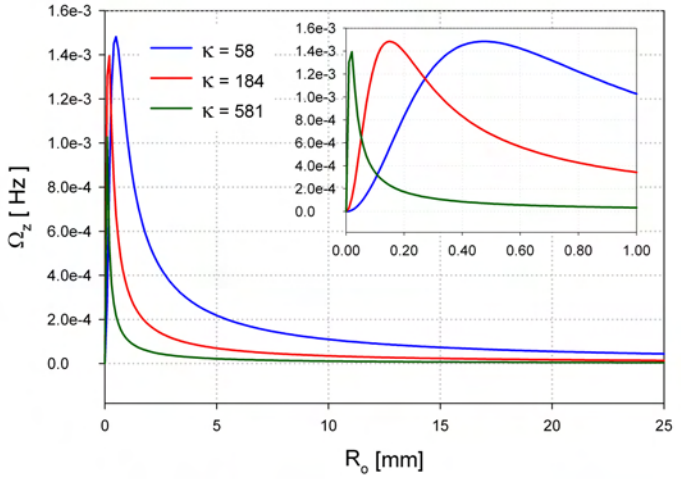

Figure 2-9: Composite vorticity as a function of the external radius of the container R_O. These were obtained with EMG705 properties for a frequency of 85 Hz, amplitude of 5 mT for the applied magnetic field, and κ of 58, 184 and 581 corresponding to η' of 10^{-10}, 10^{-11} and $10^{-12}\,\mathrm{kg\,m\,s^{-1}}$. The inset corresponds to the vorticity for $R_O < 1\,\mathrm{mm}$ where the vorticity maximum changes depending on the value of κ.

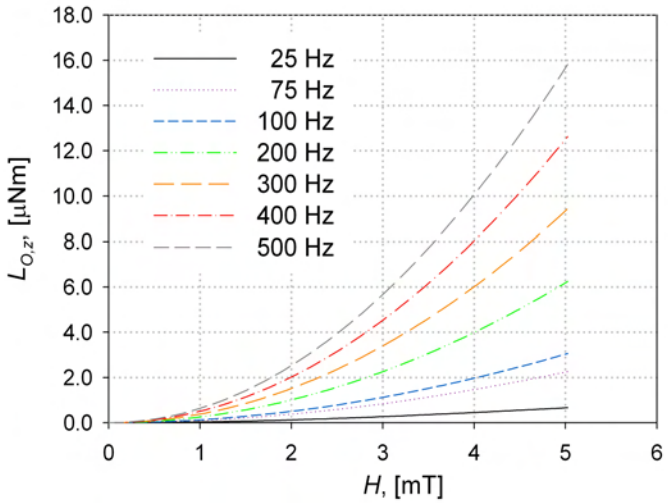

Figure 2-10: Theoretical predictions for torque on the inner surface of a hollow spindle as a function of frequency and amplitude of the applied magnetic field.

Chapter 3

Analysis of flow and torque for ferrofluid between coaxial cylinders with zero and non-zero spin viscosity (η')

In the first section of this chapter we review the theoretical predictions found in the literature for flow and torque of ferrofluid in the gap of two stationary coaxial cylinders with a rotating magnetic field. The principal difference with the previous analysis of flow in a cylindrical container is that the magnetic field and magnetization in the annular gap are nonhomogeneous as a consequence of the inner cylinder, resulting in magnetic body forces that may contribute to the flow. This fact was taken into account for the first time by Pshenichnikov and Lebedev [15] who obtained an expression for the torque on the surface of the free inner cylinder. Nonetheless, as will be shown below, their torque expression is incorrect as the integration constants for the magnetic field and magnetization are inconsistent with Maxwell's equations. In addition, the correct expressions for the torque are obtained and compared with the expressions of torque obtained by Rinaldi *et al.* [16] using a regular perturbation method and $\tilde{\Omega}_f$ as the perturbation parameter in the limit of zero spin viscosity ($\eta' = 0$).

Next, we obtain the zeroth order expression for spin and translation velocity fields with

non-zero spin viscosity using the regular perturbation method and the perturbation parameter $\mu_0 \chi_i K^2 \tau / \zeta$. The predictions of this analysis are compared with experimental measurements of flow and torque in Chapter 6.

3.1 Previous work

The flow of a ferrofluid contained in the annular gap between two concentric cylinders and subjected to a rotating magnetic field has been investigated by several authors [14–17, 27, 63]. The problem is closely related to the observation of ferrofluid motion in a cylindrical container under an applied uniform rotating magnetic field [8, 9, 17, 19, 45], except that the field in the case of the ferrofluid in the annular gap is not uniform owing to the presence of the inner cylinder. The initial work is due to Tsebers [14], who obtained an expression for azimuthal flow, arguing that tangential stresses are zero at the boundary of a freely suspended cylinder. That analysis predicted no bulk flow when both cylinders are held fixed. Rosensweig *et al.* [17], obtained experimental top free surface velocity profiles for the case in which both cylinders are stationary. The velocity profile at the free surface was observed to reverse direction along the annulus, with the ferrofluid co-rotating with the field near the surface of the inner cylinder and counter-rotating with the field near the surface of the outer cylinder. Rosensweig *et al.* [17] compared these observations to their analysis in which the transport of internal angular momentum included the effects of spin viscosity, neglected by Tsebers [14]. Based on their experimental observations and the lack of qualitative agreement with the available analysis, Rosensweig *et al.* concluded that the observed flow was solely due to magnetic surface stresses on the ferrofluid-air interface. Unfortunately, both Tsebers [14] and Rosensweig *et al.* [17] assumed in their models that the magnetic field in the annular gap was homogeneous, an error which was later corrected by Lebedev and Pshenichnikov [27], who obtained expressions for flow and torque in the absence of free surface effects and when the fluid temperature and concentration are homogeneous. Their analysis predicted flow only when the inner cylinder is free to rotate, whereas when both cylinders are stationary flow was considered possible only if the fluid had a concentration or temperature gradient, as discussed by Shliomis *et al.* [44]. Predictions for the torque were compared with experimental data obtaining poor agreement.

Another expression was later obtained by Pshenichnikov and Lebedev [15], in which flow was attributed to tangential stresses at the free cylinder, which upon rotating induces flow in the bulk due to the action of viscous stresses, especially at low magnetic field frequency and amplitude, in which case thermal effects are not important. The analysis of Pshenichnikov and Lebedev [15] predicted no bulk flow when both cylinders were stationary. They obtained expressions for the torque on the inner cylinder and the angular rotation of a freely rotating cylinder immersed in the fluid. Torque predictions were in good agreement with their experimental measurements, but predictions of the amplitude of free cylinder rotation were found in poor agreement. Still, the analysis of Pshenichnikov and Lebedev [15], though it illustrated the role of interfacial stresses in inducing flow in ferrofluids, is internally inconsistent, as the integration constants obtained for the magnetic field are incorrect [63], as will be demonstrated in the next section.

An asymptotic expression for the torque on the inner cylinder taking $\eta' = 0$ and valid for $\tilde{\Omega}_f \ll 1$, was given by Rinaldi *et al.* [16]

$$L_{th} = -\frac{8\mu_0\chi_i\left(1+\chi\right)H_{rms}^2\left(\pi R_I^2 l\right)}{\left[2+\chi_i\left(1+\Upsilon^2\right)\right]^2}\tilde{\Omega}_f + \mathcal{O}\left(\tilde{\Omega}_f^2\right), \tag{3.1}$$

where Υ is the radial aspect ratio of the inner to external cylinder (R_I/R_O). Therein, measurements were reported for the viscous torque when ferrofluid is either entirely inside (torque on the inner surface of the cylindrical container in so-called spin-up flow) or entirely outside (annular flow) of a stationary infinitely long cylinder, subjected to a rotating magnetic field. A more detailed derivation of this expression, together with detailed experimental measurements of torque and flow was presented in [64], where it was shown that ferrofluid flow is present even when both cylinders are fixed. Although flow was not predicted by this analysis, the predictions for torque were found in good agreement with the torque measurements.

3.1.1 Pshenichnikov and Levedev expressions for magnetization and magnetic field.

In their paper "Tangential Stresses on the Magnetic Fluid Boundary and Rotational Effect" [15], Pshenichnikov and Lebedev consider the situation of a ferrofluid in the gap between two coaxial cylinders and subjected to a rotating magnetic field perpendicular to the axis of the cylindrical

walls. The authors provide an analysis based on Shliomis' expression for the interfacial stress on the inner cylinder surface. This analysis is an improvement over previous work by Tsebers [14] and Rosensweig *et al.* [17] who assumed that the magnetic field in the annular space is uniform. Pshenichnikov and Lebedev demonstrate that the general solution for the magnetic field and magnetization in the annular gap which satisfies Maxwell's equations and the magnetization relaxation equation is a field with a radially-dependent contribution. Unfortunately, as we will show below, the integration constants obtained by Pshenichnikov and Lebedev are incorrect and therefore their expression for the torque on the inner cylinder is also incorrect.

Pshenichnikov and Lebedev [15] analyze the problem of ferrofluid in the gap between two coaxial cylinders and subjected to a rotating magnetic field perpendicular to the axis of the cylindrical wall. They obtain solutions for the radial and azimuthal components of magnetic field

$$\begin{aligned} H_r &= C_1 \cos\varphi - \frac{C_2}{r^2}\cos\left(\varphi+\beta\right), \\ H_\theta &= -C_1 \sin\varphi - \frac{C_2}{r^2}\sin\left(\varphi+\beta\right), \end{aligned} \tag{3.2}$$

and magnetization

$$\begin{aligned} M_r &= \chi\left[C_1\cos\left(\varphi+\delta\right) - \frac{C_2}{r^2}\cos\left(\varphi+\beta+\delta\right)\right], \\ M_\varphi &= -\chi\left[C_1\sin\left(\varphi+\delta\right) + \frac{C_2}{r^2}\sin\left(\varphi+\beta+\delta\right)\right], \end{aligned} \tag{3.3}$$

where χ is the dynamic susceptibility given by

$$\chi = \chi_1 - j\chi_2$$

and whose in-phase χ_1, and out of phase χ_2 components are defined as

$$\chi_1 = \frac{\chi_i}{1+\tilde{\Omega}_f^2};\ \chi_2 = \frac{\chi_i\tilde{\Omega}_f}{1+\tilde{\Omega}_f^2};\ \chi = \sqrt{\chi_1^2+\chi_2^2}$$

As can be seen in Eqns. (3.2) and (3.3) Pshenichnikov and Lebedev [15] demonstrate that the general solution for the magnetic field and magnetization in the annular gap (expressed in their

paper in a frame of reference that rotates with the applied field) which satisfies Maxwell's equations and the magnetization relaxation equation, predicts a field with a radially-dependent contribution. However, as was mentioned above, the integration constants obtained by Pshenichnikov and Lebedev are incorrect as they do not satisfy the interfacial jump conditions for the magnetic field and magnetic induction in the inner cylinder-ferrofluid interface. To demonstrate this, we write the boundary conditions of the problem as

$$H_\theta\left(R_1,\varphi\right) = H_\theta^I\left(R_1,\varphi\right) = -A\sin\varphi, \tag{3.4}$$

$$H_r\left(R_1,\varphi\right) + M_r\left(R_1,\varphi\right) = H_r^I\left(R_1,\varphi\right) = A\cos\varphi, \tag{3.5}$$

where the superscript I denotes the magnetic field in the inner solid cylinder obtained by dropping the terms which depend on radial position in Eqn. (3.2) and A is the integration constant in the inner cylinder. Solving for A in Eqns. (3.4) and (3.5) and combining the two resultant expressions in

$$-\cos\varphi H_\theta\left(R_1,\varphi\right) = \sin\varphi\left[H_r\left(R_1,\varphi\right) + M_r\left(R_1,\varphi\right)\right]. \tag{3.6}$$

Substituting the expressions for the components of the field and magnetization in Eqn. (3.6) we obtain

$$\begin{aligned}-\cos\varphi\left[-C_1\sin\varphi - \frac{C_2}{R_1^2}\sin\left(\varphi+\beta\right)\right] = \sin\varphi\,[&C_1\cos\varphi \\ &-\frac{C_2}{R_1^2}\cos\left(\varphi+\beta\right) + \chi\left(C_1\cos\left(\varphi+\beta\right) - \frac{C_2}{R_1^2}\cos\left(\varphi+\beta+\delta\right)\right)\Bigg].\end{aligned}$$

and taking common factors of C_1 and C_2 yields

$$\begin{aligned}C_1\chi\sin\varphi\cos\left(\varphi+\delta\right) = \frac{C_2}{R_1^2}\,[&\cos\varphi\sin\left(\varphi+\beta\right) \\ &+\sin\varphi\cos\left(\varphi+\beta\right) + \chi\sin\varphi\cos\left(\varphi+\beta+\delta\right)].\end{aligned} \tag{3.7}$$

Now, we introduce the expressions for the constants C_1 and C_2 presented in the manuscript of

Pshenichnikov and Lebedev (Eqn. PL-9)

$$\frac{C_1}{\sqrt{4+4\chi_1+\chi^2}} = \frac{C_2}{\chi R_1^2} = \frac{2H_0}{4+4\chi_1+\chi^2-\chi^2 R_1^2/R_2^2}, \qquad (3.8)$$
$$\tan\beta = \frac{2\chi_2}{\chi^2+2\chi_1}.$$

simplifying Eqn. (3.7) to

$$\sin\varphi\cos(\varphi+\delta)\sqrt{4+4\chi_1+\chi^2} = [\cos\varphi\sin(\varphi+\beta) + \sin\varphi\cos(\varphi+\beta)+\chi\sin\varphi\cos(\varphi+\beta+\delta)] \qquad (3.9)$$

Next we separate the trigonometric functions into parts

$$\sqrt{4+4\chi_1+\chi^2}\left(\cos\delta\cos\varphi\sin\varphi-\sin\delta\sin^2\varphi\right) =$$
$$2\cos\beta\cos\varphi\sin\varphi+\sin\beta\cos^2\varphi-\sin\beta\sin^2\varphi$$
$$+\chi\left(\cos\beta\cos\delta\cos\varphi\sin\varphi-\sin\beta\cos\varphi\sin\delta\sin\varphi-\cos\beta\sin\delta\sin^2\varphi-\cos\delta\sin\beta\sin^2\varphi\right),$$

and substitute the following expressions, obtained from the relations given in their paper, for the trigonometric functions of the phase angles α and β

$$\tan\delta = \frac{\chi_2}{\chi_1}; \quad \sin\delta\frac{\chi_2}{\chi}; \quad \cos = \frac{\chi_1}{\chi}, \qquad (3.10)$$

$$\tan\beta = \frac{2\chi_2}{\chi_2+2\chi_1}; \quad \sin\beta = \frac{2\chi_2}{\chi\sqrt{4+4\chi_1+\chi^2}}; \quad \cos\beta = \frac{\chi^2+2\chi_1}{\chi\sqrt{4+4\chi_1+\chi^2}}, \qquad (3.11)$$

to obtain

$$\sqrt{4+4\chi_1+\chi^2}\left(\frac{\chi_1}{\chi}\cos\varphi\sin\varphi-\frac{\chi_2}{\chi}\sin^2\varphi\right) = \left\{2\frac{\chi^2+2\chi_1}{\chi\sqrt{4+4\chi_1+\chi^2}}\cos\varphi\sin\varphi\right.$$
$$+\frac{2\chi_2}{\chi\sqrt{4+4\chi_1+\chi^2}}\cos^2\varphi-\frac{2\chi_2}{\chi\sqrt{4+4\chi_1+\chi^2}}\sin^2\varphi+\chi\left[\frac{\chi_1}{\chi}\frac{\chi^2+2\chi_1}{\chi\sqrt{4+4\chi_1+\chi^2}}\cos\varphi\sin\varphi\right.$$
$$\left.\left.-\frac{\chi_2}{\chi}\frac{2\chi_2}{\chi\sqrt{4+4\chi_1+\chi^2}}\cos\varphi\sin\varphi-\frac{\chi_2}{\chi}\frac{\chi^2+2\chi_1}{\chi\sqrt{4+4\chi_1+\chi^2}}\sin^2\varphi-\frac{\chi_1}{\chi}\frac{2\chi_2}{\chi\sqrt{4+4\chi_1+\chi^2}}\sin^2\varphi\right]\right\}.$$

This result can be simplified to

$$2\chi_2 = 0 \tag{3.12}$$

demonstrating that the integration constants and expressions given by Pshenichnikov and Lebedev satisfy the interfacial conditions for the magnetic field and magnetic induction at the inner cylinder-ferrofluid interface only when $\chi_2 = 0$, which would be the case for a stationary magnetic field. Hence their solution for torque on inner cylinder obtained using Eqn. (3.8) is also incorrect.

3.1.2 Corrected torque expressions for: "Tangential Stresses on the Magnetic Fluid Boundary and Rotational Effect"

First we obtain the solution for the rotating magnetic field and corresponding torque on the inner and outer cylinders. In order to make our solution general, the situation we analyze corresponds to a non-magnetic cylinder of radius R_1, surrounded by ferrofluid in a cylindrical annulus $R_1 < r < R_2$, itself surrounded by a non-magnetic annulus of outer radius R_3. At R_3 there is an ideal two-pole surface current, given by

$$\mathbf{K} = \mathrm{Re}\left\{ jH_0 \; e^{j(\Omega t - n\theta)} \right\} \mathbf{i}_z, \tag{3.13}$$

backed by an infinite-permeability material. In this expression $j = \sqrt{-1}$ and H_0 is the field amplitude of a uniform field generated in the gap of the stator winding in the absence of ferrofluid. This three-region problem reduces to the problem analyzed by Rinaldi *et al.* [16] when $R_2 = R_3$ and it corresponds to the situation when the ferrofluid is surrounded by an infinite non-magnetic material with a uniform counter-clockwise rotating field

$$\mathbf{H}_0 = H_0 \cos(\theta - \Omega t)\, \mathbf{i}_r - H_0 \sin(\theta - \Omega t)\, \mathbf{i}_\theta \tag{3.14}$$

at infinity when one takes the limit $R_3 \to \infty$. This latter limit corresponds to the situation analyzed by Pshenichnikov and Lebedev, except for the specification of a phase angle, as is explained below.

We assume that in each region i, the magnetic field has the form

$$\mathbf{H}_i = \mathrm{Re}\left\{\left[\hat{H}_{r,i}\left(r\right)\mathbf{i}_r + \hat{H}_{\theta,i}\left(r\right)\mathbf{i}_\theta\right]e^{j(\Omega t-\theta)}\right\}, \tag{3.15}$$

where a hat indicates a complex quantity. Region 1 corresponds to the inner non-magnetic cylinder in $r < R_1$, region 2 corresponds to the ferrofluid annulus in $R_1 < r < R_2$, and region 3 corresponds to the outer non-magnetic annulus in $R_2 < r < R_3$. In region 2 we assume the magnetization has the form

$$\mathbf{M}_2 = \mathrm{Re}\left\{\left[\hat{M}_{r,2}\left(r\right)\mathbf{i}_r + \hat{M}_{\theta,2}\left(r\right)\mathbf{i}_\theta\right]e^{j(\Omega t-\theta)}\right\}. \tag{3.16}$$

Substituting these expressions into Ampére's and Gauss' laws and the magnetization relaxation equation of Shliomis, neglecting the velocity and spin velocity dependent terms, one obtains the following solutions for the radially-dependent complex amplitudes

$$\hat{H}_{r,i}\left(r\right) = \hat{C}_{1,i} + \hat{C}_{2,i}r^{-2}, \tag{3.17}$$

$$\hat{H}_{\theta,i}\left(r\right) = -j\left(\hat{C}_{1,i} - \hat{C}_{2,i}r^{-2}\right), \tag{3.18}$$

$$\hat{M}_{r,2}\left(r\right) = \frac{\chi_0}{1+j\tilde{\Omega}_f}\hat{H}_{r,2}\left(r\right), \tag{3.19}$$

$$\hat{M}_{\theta,2}\left(r\right) = \frac{\chi_0}{1+j\tilde{\Omega}_f}\hat{H}_{\theta,2}\left(r\right). \tag{3.20}$$

The integration constant $\hat{C}_{2,1}$ for the inner region is zero from the requirement that the field remain finite at $r = 0$. The remaining integration constants are obtained from the boundary conditions of the magnetic field and magnetic induction $\mathbf{B} = \mu_0\left(\mathbf{H}+\mathbf{M}\right)$

$$\mu_0 H_{r,1}\left(R_1,\theta,t\right) = \mu_0\left[H_{r,2}\left(R_1,\theta,t\right) + M_{r,2}\left(R_1,\theta,t\right)\right], \tag{3.21}$$

$$H_{\theta,1}\left(R_1,\theta,t\right) = H_{\theta,2}\left(R_1,\theta,t\right), \tag{3.22}$$

$$\mu_0\left[H_{r,2}\left(R_2,\theta,t\right) + M_{r,2}\left(R_2,\theta,t\right)\right] = \mu_0 H_{r,3}\left(R_2,\theta,t\right), \tag{3.23}$$

$$H_{\theta,2}\left(R_2,\theta,t\right) = H_{\theta,3}\left(R_2,\theta,t\right), \tag{3.24}$$

$$-H_{\theta,3}\left(R_3,\theta,t\right) = K_z\left(\theta,t\right), \tag{3.25}$$

Upon solving these five relations for the five unknown integration constants, and defining $\Upsilon = \frac{R_1}{R_2}$, $\Upsilon_1 = \frac{R_1}{R_3}$, and $\Upsilon_2 = \frac{R_2}{R_3}$, we obtain

$$\hat{C}_{1,1} = \frac{4\left[\left(1+\chi_i-\tilde{\Omega}_f^2\right)+j\left(2+\chi_i\right)\tilde{\Omega}_f\right]H_0}{A}, \tag{3.26}$$

$$\hat{C}_{1,2} = \frac{2\left[\left(2+\chi_i-2\tilde{\Omega}_f\right)+j\left(4+\chi_i\right)\tilde{\Omega}_f\right]H_0}{A}, \tag{3.27}$$

$$\hat{C}_{2,2} = -\frac{2\left(1+j\tilde{\Omega}_f\right)\chi_i R_1^2 H_0}{A}, \tag{3.28}$$

$$\hat{C}_{1,3} = \frac{\left\{\left[4\left(1-\tilde{\Omega}_f^2\right)+4\chi_i+\left(1-\Upsilon^2\right)\chi_i^2\right]+j4\tilde{\Omega}_f\left(2+\chi_i\right)\right\}H_0}{A}, \tag{3.29}$$

$$\hat{C}_{2,3} = \frac{\left(1-\Upsilon^2\right)\left[\left(2+\chi_i\right)+j2\tilde{\Omega}_f\right]\chi_i R_2^2 H_0}{A}, \tag{3.30}$$

$$A = 4\left(1-\tilde{\Omega}_f^2\right)+2\left(2+\Upsilon_1^2-\Upsilon_2^2\right)\chi_i+\left(1-\Upsilon^2+\Upsilon_1^2-\Upsilon_2^2\right)\chi_i^2 + 2j\tilde{\Omega}_f\left[4+\left(2+\Upsilon_1^2-\Upsilon_2^2\right)\chi_i\right] \tag{3.31}$$

Using these expressions for the complex amplitudes one can obtain expressions for the magnetic field and magnetization. However, the actual measurable quantity is the torque exerted by the ferrofluid on the inner L_{R_1} and outer L_{R_2} cylinders. We can evaluate these torques from

$$L_{R_1} = 2\pi R_1^2 l\left(\sigma_{r\theta}\right)\big|_{r=R_1}, \tag{3.32}$$

$$L_{R_2} = -2\pi R_2^2 l\left(\sigma_{r\theta}\right)\big|_{r=R_2}, \tag{3.33}$$

where $\sigma_{r\theta}$ is the $r\theta$-component of the deviatoric stress tensor $\boldsymbol{\sigma}$. Arguably there would also be a contribution from the jump in the Maxwell stress tensor across the interface, but it is simple to show that this contribution is zero for the z-directed torque. In a ferrofluid the deviatoric stress tensor $\boldsymbol{\sigma}$ has symmetric and anti-symmetric contributions, given by

$$\boldsymbol{\sigma} = \eta\left[\boldsymbol{\nabla}\mathbf{v}+(\boldsymbol{\nabla}\mathbf{v})^{\dagger}\right]+\zeta\boldsymbol{\varepsilon}\cdot\left[\boldsymbol{\nabla}\times\mathbf{v}-2\boldsymbol{\omega}\right], \tag{3.34}$$

where η is the shear viscosity, ζ is the vortex viscosity, and $\boldsymbol{\varepsilon}$ is the unit pseudo-isotropic triadic. However, as explained by Pshenichnikov and Lebedev, under weak applied fields the magnetic forces in the problem are potential and the resulting mass average velocity is zero, $\mathbf{v} = \mathbf{0}$. Upon further substituting the internal angular momentum equation

$$\mathbf{0} = \mu_0 \mathbf{M} \times \mathbf{H} + 2\zeta \left[\boldsymbol{\nabla} \times \mathbf{v} - 2\boldsymbol{\omega} \right], \tag{3.35}$$

neglecting angular inertia and the couple stress term, the above expression for the deviatoric stress reduces to

$$\boldsymbol{\sigma} = -\mu_0 \frac{1}{2} \boldsymbol{\varepsilon} \cdot \left[\mathbf{M} \times \mathbf{H} \right]. \tag{3.36}$$

The corresponding $r\theta$-component is

$$\sigma_{r\theta} = -\mu_0 \frac{1}{2} \left(M_r H_\theta - M_\theta H_r \right). \tag{3.37}$$

Thus the torques on the inner and outer cylinder are given by

$$L_{R_1} = -\mu_0 \left(\pi R_1^2 l \right) \left(M_{r,2} H_{\theta,2} - M_{\theta,2} H_{r,2} \right)|_{r=R_1}, \tag{3.38}$$

$$L_{R_2} = \mu_0 \left(\pi R_2^2 l \right) \left(M_{r,2} H_{\theta,2} - M_{\theta,2} H_{r,2} \right)|_{r=R_2}, \tag{3.39}$$

respectively. Substituting the results for the magnetic field and magnetization in the ferrofluid annular region we obtain

$$L_{R_1} = -\frac{16 \left(\pi R_1^2 l \right) \mu_0 \chi_i \left[\chi_i + \left(1 + \tilde{\Omega}_f^2 \right) \right] \tilde{\Omega}_f H_0^2}{D}, \tag{3.40}$$

$$L_{R_2} = \frac{4 \left(\pi R_2^2 l \right) \mu_0 \chi_i \left[4 \left(1 + \tilde{\Omega}_f^2 \right) + 4\chi_i + \left(1 - \Upsilon^4 \right) \chi_i^2 \right] \tilde{\Omega}_f H_0^2}{D}, \tag{3.41}$$

where the denominator D is given by the expression

$$\begin{aligned} D = \Big\{ 16\left(1+\tilde{\Omega}_f^2\right)^2 + \chi_i \Big[16\left(2+\Upsilon_1^2-\Upsilon_2^2\right)\left(1+\tilde{\Omega}_f^2\right) \\ + \chi_i \Big(4\Big(\left(\Upsilon_1^2-\Upsilon_2^2\right)^2 + 6\left(\Upsilon_1^2-\Upsilon_2^2\right) - 2\Upsilon^2 + 6 \\ + \Big(\left(\Upsilon_1^2-\Upsilon_2^2\right)^2 + 2\left(\Upsilon_1^2-\Upsilon_2^2\right) + 2\left(1+\Upsilon^2\right)\Big)\tilde{\Omega}_f^2\Big) \\ - \left(1-\Upsilon^2\right)\left(1-\Upsilon_2^2\right)\chi_i\left(4\left(2+\Upsilon_1^2-\Upsilon_2^2\right) - \left(1-\Upsilon^2\right)\left(1-\Upsilon_2^2\right)\chi_i\right)\Big)\Big]\Big\}. \quad (3.42) \end{aligned}$$

Equation (3.40) gives the torque exerted by the fluid on the inner cylinder and is clearly in the opposite direction of field rotation (i.e., the torque is clockwise in this case), whereas Eqn. (3.41) gives the torque exerted by the fluid on the outer cylinder and is clearly in the direction of field rotation (i.e., the torque is counter-clockwise in this case).

There are two interesting limits of Eqns. (3.40) and (3.41). The first corresponds to the two-region problem obtained when the outer non-magnetic region is infinitesimally thin. In that case $\Upsilon_1 = \Upsilon$ and $\Upsilon_2 = 1$, resulting in

$$L_{2,R_1} = -\frac{4\left(\pi R_1^2 l\right)\mu_0\chi_i\left[\chi_i + \left(1+\tilde{\Omega}_f^2\right)\right]\tilde{\Omega}_f H_i^2}{\left(1+\tilde{\Omega}_f^2\right)\left[4\left(1+\tilde{\Omega}_f^2\right) + \left(1+\Upsilon^2\right)\chi_i\left(4+\left(1+\Upsilon^2\right)\chi_i\right)\right]}, \quad (3.43)$$

for the inner cylinder, and

$$L_{2,R_2} = \frac{\left(\pi R_2^2 l\right)\mu_0\chi_i\left[4\left(1+\tilde{\Omega}_f^2\right) + 4\chi_i + \left(1-\Upsilon^4\right)\chi_i^2\right]\tilde{\Omega}_f H_0^2}{\left(1+\tilde{\Omega}_f^2\right)\left[4\left(1+\tilde{\Omega}_f^2\right) + \left(1+\Upsilon^2\right)\chi_i\left(4+\left(1+\Upsilon^2\right)\chi_i\right)\right]}, \quad (3.44)$$

for the outer cylinder. It is illustrative to compare Eqn. (3.43) with the expression reported by Rinaldi *et al.* [16] for the torque on the inner cylinder. Their analysis used a regular perturbation expansion in the small parameter $\tilde{\Omega}_f$, hence we expand (3.43) in powers of $\tilde{\Omega}_f$ to obtain

$$L_{2,R_1} = -\frac{4\left(\pi R_1^2 l\right)\mu_0\chi_i\left(1+\chi_i\right)H_0^2\tilde{\Omega}_f}{\left[2+\chi_i\left(1+\Upsilon^2\right)\right]^2} + \mathcal{O}\left(\tilde{\Omega}_f^3\right), \quad (3.45)$$

which is equivalent to the expression in [16] if one replaces the peak field amplitude H_0 with the rms field amplitude $H_{rms} = H_0/\sqrt{2}$. Notice that expanding Eqn. (3.43) in powers of $\tilde{\Omega}_f$

indicates that the term of order $\tilde{\Omega}_f^2$ does not contribute to the torque on the inner cylinder. We can also obtain the result for the torque on the outer cylinder when $R_1 = 0$ ($\Upsilon = \Upsilon_1 = 0$)

$$L_{2,R_1=0} = \frac{\left(\pi R_2^2 l\right) \mu_0 \chi_i \tilde{\Omega}_f H_0^2}{\left(1 + \tilde{\Omega}_f^2\right)}. \tag{3.46}$$

The other limit of Eqns. (3.40) and (3.41) which is of interest corresponds to the case where $R_3 \to \infty$ while Υ remains finite. This limit corresponds to the ferrofluid surrounded by an infinite non-magnetic outer region in which there is a uniform counter-clockwise rotating field at infinity, of magnitude H_0. This limit corresponds to $\Upsilon_1 \to 0$ and $\Upsilon_2 \to 0$ and the resulting torque on the inner cylinder is

$$L_{\infty,R_1} = -\frac{16\left(\pi R_1^2 L\right) \mu_0 \chi_i \left[\chi_i + \left(1 + \tilde{\Omega}_f^2\right)\right] \tilde{\Omega}_f H_0^2}{\left[4\chi_i + \left(1 + \Upsilon^2\right)\chi_i^2 + 4\left(1 + \tilde{\Omega}_f^2\right)\right]^2 - 4\Upsilon^2 \chi_i^2 \left(2 + \chi_i\right)^2}, \tag{3.47}$$

$$= -\frac{16\left(\pi R_1^2 L\right) \mu_0 \chi_2 \left(1 + \chi_1\right) H_0^2}{\left[4 + 4\chi_1 + \left(1 + \Upsilon^2\right)\chi^2\right]^2 - 4\Upsilon^2 \chi_1^2 \left(2 + \chi_i\right)^2}, \tag{3.48}$$

in which the last expression has been modified using the definitions for the in-phase, χ_1, and out-of-phase, χ_2, components of the ferrofluid's dynamic susceptibility

$$\chi = \chi_1 - j\chi_2 \;\; ; \;\; \chi_1 = \frac{\chi_i}{1 + \tilde{\Omega}_f^2} \;\; ; \;\; \chi_2 = \frac{\chi_i \tilde{\Omega}_f}{1 + \tilde{\Omega}_f^2} \;\; ; \;\; \chi = \sqrt{\chi_1^2 + \chi_2^2}. \tag{3.49}$$

The torque on the outer cylinder for this situation is

$$L_{\infty,R_2} = \frac{4\left(\pi R_2^2 l\right) \mu_0 \chi_i \left[4\left(1 + \tilde{\Omega}_f^2\right) + 4\chi_i + \left(1 - \Upsilon^4\right)\chi_i^2\right] \tilde{\Omega}_f H_0^2}{\left[4\chi_i + \left(1 + \Upsilon^2\right)\chi_i^2 + 4\left(1 + \tilde{\Omega}_f^2\right)\right]^2 - 4\Upsilon^2 \chi_i^2 \left(2 + \chi_i\right)^2}, \tag{3.50}$$

$$= \frac{4\left(\pi R_2^2 l\right) \mu_0 \chi_2 \left[4 + 4\chi_1 + \left(1 - \Upsilon^4\right)\chi_i \chi_1\right] H_0^2}{\left[4 + 4\chi_1 + \left(1 + \Upsilon^2\right)\chi^2\right]^2 - 4\gamma^2 \chi_1^2 \left(2 + \chi_i\right)^2}. \tag{3.51}$$

Finally we consider the case without an inner cylinder, $R_1 = 0$, to obtain

$$T_{\infty,R_1=0} = \frac{4\left(\pi R_2^2 l\right)\mu_0\chi_i\left[4\left(1+\tilde{\Omega}_f^2\right)+4\chi_i+\chi_i^2\right]\tilde{\Omega}_f H_0^2}{\left[4\chi_i+\chi_i^2+4\left(1+\tilde{\Omega}_f^2\right)\right]^2}, \tag{3.52}$$

$$= \frac{4\left(\pi R_2^2 L\right)\mu_0\chi_2 H_0^2}{(4+4\chi_1+\chi^2)}. \tag{3.53}$$

Now, we compare the correct torque on the inner cylinder (3.48) to the torque per unit volume K given by Pshenichnikov and Lebedev in their equation (PL-10). To do so we divide (3.48) by the inner cylinder volume to obtain K_∞ and take the ratio of the result with (PL-10)

$$\frac{K_{\infty,R_1}}{K} = \frac{\left(4+4\chi_1+\chi^2-\chi^2\Upsilon^2\right)^2}{\left[4+4\chi_1+\left(1+\Upsilon^2\right)\chi^2\right]^2-4\Upsilon^2\chi_1^2\left(2+\chi_i\right)^2}. \tag{3.54}$$

The ratio of Eqn. (3.54) is in general not unity. However, in the experiments of Pshenichnikov and Lebedev the field frequency was small compared to the inverse rotational relaxation time (i.e., $\tilde{\Omega}_f \ll 1$), hence we expand (3.54) in powers of $\tilde{\Omega}_f$ and obtain

$$\frac{K_\infty}{K} \approx 1 + \mathcal{O}\left(\tilde{\Omega}_f^2\right), \tag{3.55}$$

where the $\mathcal{O}\left(\tilde{\Omega}_f^2\right)$ is not trivially zero (it is not shown here for simplicity). Thus we see that under the limitation $\tilde{\Omega}_f \ll 1$, the expression for the torque given in (PL-10) is equivalent to the correct expression (3.48), and should therefore match the experimental measurements well, as found by Pshenichnikov and Lebedev.

We can also compare the torque expression (3.53) to the torque per unit volume K_0 given by Pshenichnikov and Lebedev in their equation (PL-16). To do so we divide (3.53) by the ferrofluid volume $\pi R_2^2 L$ to obtain $K_{\infty,R_2,R_1=0}$ and take the ratio with the result in (PL-16)

$$\frac{K_{\infty,R_2,R_1=0}}{K_0} = 1. \tag{3.56}$$

Hence in this case, equation (PL-16) is found to be correct.

3.2 Analysis of flow and torque with non-zero spin viscosity

Conceptually, we consider the experimental situation illustrated in Fig. 3-1. This consists of ferrofluid contained in the gap of two nonmagnetic coaxial cylinders of infinite length in the z-direction and magnetic permeability μ_p. The radii of the external and internal cylinder are R_O and R_I respectively. The magnetic field is generated in the gap by a two-pole three-phase stator winding which is modeled as a surface current distribution in the z-direction Eqn. (3.13), with real amplitude $K = jH_0$ located at radius $r = R_O$, and which varies sinusoidally with time at radian frequency Ω_f. The current distribution is backed with a material of infinite magnetic permeability, $\mu \to \infty$. This geometry is a simplification of the general three region problem found in the experiments described in Chapter 6, where a non-magnetic annulus separates the ferrofluid from the stator winding.

3.2.1 Equations of the problem

In order to obtain the solution for the spin and velocity fields we use the zeroth order ferrohydrodynamic equations from Chapter 2. In this geometry we will obtain only the zeroth order solution, hence the subscript zero is dropped, obtaining

$$\tilde{\boldsymbol{\nabla}} \times \tilde{\mathbf{H}} = 0, \tag{3.57}$$

$$\tilde{\boldsymbol{\nabla}} \cdot \left(\chi_i \tilde{\mathbf{M}} + \tilde{\mathbf{H}}\right) = 0. \tag{3.58}$$

$$\tilde{\Omega}_f \frac{\partial \tilde{\mathbf{M}}}{\partial \tilde{t}} = \tilde{\mathbf{H}} - \tilde{\mathbf{M}}, \tag{3.59}$$

$$\mathbf{0} = \frac{\zeta}{\tilde{\Omega}_f \eta} \tilde{\mathbf{M}} \cdot \tilde{\boldsymbol{\nabla}} \tilde{\mathbf{H}} - \tilde{\boldsymbol{\nabla}} \tilde{p} + \frac{2\zeta}{\eta} \tilde{\boldsymbol{\nabla}} \times \tilde{\boldsymbol{\omega}} + \frac{\eta_e}{\zeta} \tilde{\boldsymbol{\nabla}}^2 \tilde{\mathbf{v}} \tag{3.60}$$

$$\mathbf{0} = \frac{1}{\tilde{\Omega}_f} \tilde{\mathbf{M}} \times \tilde{\mathbf{H}} + 2\tilde{\boldsymbol{\nabla}} \times \tilde{\mathbf{v}} - 4\tilde{\boldsymbol{\omega}} + \frac{4\eta}{\eta_e \kappa^2} \tilde{\boldsymbol{\nabla}}^2 \tilde{\boldsymbol{\omega}}. \tag{3.61}$$

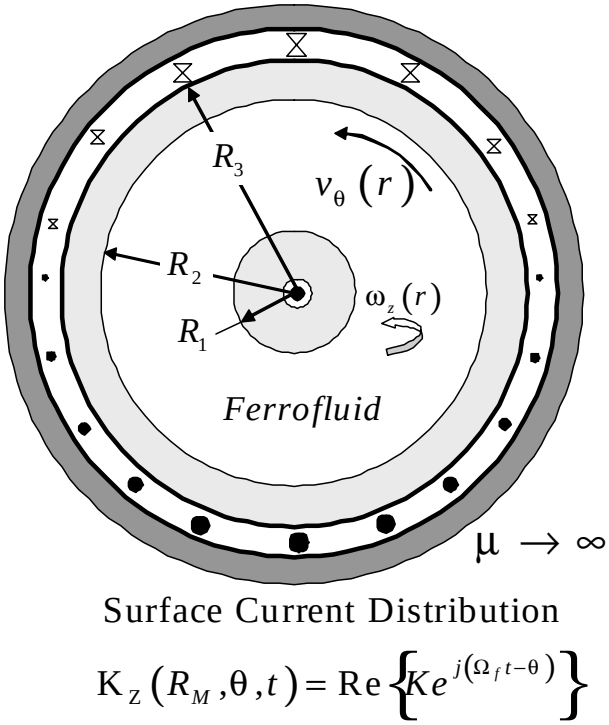

Figure 3-1: Schematic illustration of the coupled magnetic-hydrodynamic problem for ferrofluid in the annular gap between two nonmagnetic coaxial cylinders. The radii of the external and internal cylinders are R_1 and R_2 respectively. In this figure $R_3 - R_2$ corresponds to the thickness of the external cylinder or the space between the cylinder and the surface current distribution. The azimuthal velocity component and axial directed spin velocity are obtained for a long annulus of ferrofluid between $R_1 < r < R_2$ subjected to a rotating magnetic field perpendicular to the axis of the cylinder. The magnetic field source is modeled as a z-directed surface current distribution $K(\theta, t)\,\mathbf{i}_z$. which is backed by a material of infinite magnetic permeability, $\mu \to \infty$.

3.2.2 Magnetic field and magnetization

We assume that the magnetic field and magnetization have a functional form similar to Eqn. (3.13) with $m = 1$

$$\tilde{\mathbf{H}}\left(\tilde{r},\theta,\tilde{t}\right) = \mathrm{Re}\left\{\left[\hat{H}_r(\tilde{r})\mathbf{i}_r + \hat{H}_\theta(\tilde{r})\mathbf{i}_\theta\right]e^{j\left(\tilde{t}-\theta\right)}\right\}, \tag{3.62}$$

$$\tilde{\mathbf{M}}\left(\tilde{r},\theta,\tilde{t}\right) = \mathrm{Re}\left\{\left[\hat{M}_r(\tilde{r})\mathbf{i}_r + \hat{M}_\theta(\tilde{r})\mathbf{i}_\theta\right]e^{j\left(\tilde{t}-\theta\right)}\right\}, \tag{3.63}$$

where the hat denotes a complex-amplitude quantity.

Using Eqn. (3.63) in Eqn. (3.59), we obtain expressions for the zeroth order magnetization components as a function of the zeroth order components of the magnetic field,

$$\hat{M}_\theta\left(\tilde{r}\right) = \frac{\hat{H}_\theta}{1+j\tilde{\Omega}_f},\ \hat{M}_r\left(\tilde{r}\right) = \frac{\hat{H}_r}{1+j\tilde{\Omega}_f}. \tag{3.64}$$

Now, substituting (3.64) in Eqn. (3.58) and using Eqn. (3.57), we obtain the following system of differential equations for the azimuthal and radial components of the magnetic field

$$\frac{d\left(\tilde{r}\hat{H}_\theta\right)}{d\tilde{r}} + j\hat{H}_r = 0, \tag{3.65}$$

$$\frac{d\left(\tilde{r}\hat{H}_r\right)}{d\tilde{r}} = j\hat{H}_\theta. \tag{3.66}$$

Solving Eqn. (3.66) for $\hat{H}_\theta$ and substituting into (3.65) we obtain an equidimensional equation which we solve to obtain

$$\hat{H}_{r,0} = C_1 + C_2\tilde{r}^{-2} \tag{3.67}$$

$$\hat{H}_{\theta,0} = -j\left(C_1 - C_2\tilde{r}^{-2}\right). \tag{3.68}$$

Because the magnetic field must remain finite everywhere in the region for which $r < R_I$ (inner cylinder region), we necessarily have $C_2 = 0$ in that region, then the corresponding complex

amplitude magnetic field components are given by

$$\hat{H}_r^I = C_1^I, \tag{3.69}$$

$$\hat{H}_\theta^I = -jC_1^I, \tag{3.70}$$

where $\hat{H}_r^I$ and $\hat{H}_\theta^I$ are the components of the magnetic field in the inner cylinder.

Next we apply the interfacial conditions for the magnetic field and magnetization given by Eqns. (2.13) and (2.14), expressed for the complex amplitude components of the magnetic field and magnetization and evaluated at $\tilde{r} = R_I/R_O \equiv \Upsilon$ and at $\tilde{r} = 1$ to obtain the relations

$$\mu_p \hat{H}_r^I(\Upsilon) = \mu_0 \left(\hat{H}_r(\Upsilon) + \chi_i \tilde{M}_r(\Upsilon) \right), \tag{3.71}$$

$$\hat{H}_\theta^I(\Upsilon) = \hat{H}_\theta(\Upsilon), \tag{3.72}$$

$$-\hat{H}_\theta(\Upsilon) = 1. \tag{3.73}$$

Solving Eqns. (3.71) to (3.73) for the integration constant and defining the parameters

$$\alpha \equiv \frac{\mu_0^2 \left[(1+\chi_i)^2 + \tilde{\Omega}_f^2 \right] - \mu_p^2 \left(1 + \tilde{\Omega}_f^2 \right)}{\left[\mu_0 (1+\chi_i) + \mu_p \right]^2 + \tilde{\Omega}_f^2 \left(\mu_p + \mu_0 \right)^2} \Upsilon^2, \tag{3.74}$$

and

$$\beta \equiv -\frac{2\chi_i \mu_p \mu_0 \tilde{\Omega}_f}{\left[\mu_0 (1+\chi_i) + \mu_p \right]^2 + \tilde{\Omega}_f^2 \left(\mu_p + \mu_0 \right)^2} \Upsilon^2, \tag{3.75}$$

we obtain the zeroth order complex-amplitude magnetic field components for the annular region

$$\hat{H}_r = \frac{-j}{1+\alpha+\beta} \left(1 - \frac{\alpha + j\beta}{\tilde{r}^2} \right), \tag{3.76}$$

$$\hat{H}_\theta = \frac{-1}{1+\alpha+\beta} \left(1 + \frac{\alpha + j\beta}{\tilde{r}^2} \right). \tag{3.77}$$

Equations (3.76) and (3.77) show that the magnetic field in the annular space filled with ferrofluid is position dependent. The complex-amplitude magnetization components are found simply by introducing Eqns. (3.76) and (3.77) in Eqn. (3.64).

3.2.3 Magnetic body force and body couple

To obtain the magnetic body force density we evaluate $\tilde{\mathbf{M}} \cdot \tilde{\boldsymbol{\nabla}} \tilde{\mathbf{H}}$. The relevant force component for the flow problem under consideration is the azimuthally directed magnetic force

$$\tilde{f_\theta} = (\tilde{\mathbf{M}} \cdot \tilde{\boldsymbol{\nabla}} \tilde{\mathbf{H}})_\theta = \hat{M_r} \frac{d\hat{H}_\theta}{d\tilde{r}} + \hat{M_\theta} \left(\frac{1}{\tilde{r}} \frac{d\hat{H}_\theta}{d\theta} + \frac{\hat{H}_r}{\tilde{r}} \right). \tag{3.78}$$

The magnetic body force is time dependent. The time-averaged azimuthal zeroth-order body force is calculated, using the expression given by Melcher [55] to evaluate temporal or spatial averages of complex-amplitude expressions, obtaining

$$\left\langle \tilde{f_\theta} \right\rangle_t = \frac{1}{1 + j\tilde{\Omega}_f^2} \left[\hat{H}_r^* \frac{d\hat{H}_\theta}{d\tilde{r}} + \hat{H}_r \frac{d\hat{H}_\theta^*}{d\tilde{r}} + \frac{1}{\tilde{r}} \left(\hat{H}_\theta^* \hat{H}_r + \hat{H}_\theta \hat{H}_r^* \right) \right], \tag{3.79}$$

where a superscript asterisk denotes the complex conjugate of a complex quantity. Using Eqns. (3.76) and (3.77) we obtain

$$\left\langle \tilde{f_\theta} \right\rangle_t = \frac{2\left(\alpha^2 + \beta^2\right)\tilde{\Omega}_f}{\left((1+\alpha)^2 + \beta^2\right)\left(1 + \tilde{\Omega}_f^2\right)} \frac{1}{\tilde{r}^5}. \tag{3.80}$$

The external body couple is given by

$$\tilde{l_z} = \left(\tilde{\mathbf{M}}_0 \times \tilde{\mathbf{H}}_0 \right)_z, \tag{3.81}$$

which is also time dependent. The time averaged external body couple is

$$\left\langle \tilde{l_z} \right\rangle_t = \frac{\tilde{\Omega}_f}{\left((1+\alpha)^2 + \beta^2\right)\left(1 + \tilde{\Omega}_f^2\right)} \left(1 - \frac{\alpha^2 + \beta^2}{\tilde{r}^4} \right). \tag{3.82}$$

In addition, and from Eqns. (3.80) and (3.82) it can be noted that $\left\langle \tilde{f_\theta} \right\rangle_t$ can be written as

$$\left\langle \tilde{f_\theta} \right\rangle_t = \frac{1}{2} \frac{d}{d\tilde{r}} \left[\left\langle \tilde{l_z} \right\rangle_t - \frac{\tilde{\Omega}_f}{\left((1+\alpha)^2 + \beta^2\right)\left(1 + \tilde{\Omega}_f^2\right)} \right]. \tag{3.83}$$

3.2.4 Linear and spin velocity fields

Next, we obtain the translational and spin velocity fields by solving the time-averaged linear and internal angular momentum Eqns. (3.60) and (3.61), assuming steady flow in axisymmetric cylindrical coordinates. The resulting equations governing $\tilde{v}_{\theta,0}(\tilde{r})$ and $\tilde{\omega}_{z,0}(\tilde{r})$ are the azimuthal component of the zeroth order linear momentum,

$$\eta_e \frac{d}{d\tilde{r}}\left[\frac{1}{\tilde{r}}\frac{d\left(\tilde{r}\tilde{v}_\theta\right)}{d\tilde{r}}\right] - 2\zeta\frac{d\tilde{\omega}_z}{d\tilde{r}} + \frac{\zeta}{\tilde{\Omega}_f}\left\langle \tilde{f}_\theta \right\rangle_t = 0, \tag{3.84}$$

and the z-component of the zeroth order internal angular momentum,

$$\frac{1}{\tilde{r}}\frac{d}{d\tilde{r}}\left(\tilde{r}\frac{d\tilde{\omega}_z}{d\tilde{r}}\right)\frac{4\eta}{\eta_e\kappa^2} + \frac{2}{\tilde{r}}\frac{d\left(\tilde{r}\tilde{v}_\theta\right)}{d\tilde{r}} - 4\tilde{\omega}_z + \frac{1}{\tilde{\Omega}_f}\left\langle \tilde{l}_z \right\rangle_t = 0. \tag{3.85}$$

In order to solve for $\tilde{v}_\theta(\tilde{r})$ and $\tilde{\omega}_z(\tilde{r})$, we introduce the vorticity $\tilde{\Omega}_z$ of the zeroth order translational velocity in Eqn. (3.84) and use Eqn. (3.83) to obtain

$$\frac{d}{d\tilde{r}}\left\{\frac{\eta_e}{\zeta}\tilde{\Omega}_z - 2\tilde{\omega}_z - \frac{\left(\alpha^2+\beta^2\right)}{2\left[\left(1+\alpha\right)^2+\beta^2\right]\left(1+\tilde{\Omega}_f^2\right)}\frac{1}{\tilde{r}^4}\right\} = 0. \tag{3.86}$$

Then we carry out the integration to yield an expression for the zeroth order vorticity,

$$\tilde{\Omega}_z = \frac{\zeta}{\eta_e}\left\{2\tilde{\omega}_z + \frac{\left(\alpha^2+\beta^2\right)}{2\left[\left(1+\alpha\right)^2+\beta^2\right]\left(1+\tilde{\Omega}_f^2\right)}\frac{1}{\tilde{r}^4} - C_3\right\} \tag{3.87}$$

which we substitute in Eqn. (3.85) to yield a nonhomogeneous modified Bessel equation of order zero for the z-component of spin velocity

$$\frac{1}{\tilde{r}}\frac{d}{d\tilde{r}}\left(\tilde{r}\frac{d\tilde{\omega}_z}{d\tilde{r}}\right) - \kappa^2\tilde{\omega}_z = \frac{\zeta\kappa^2}{2\eta}C_3 - \frac{\left(\alpha+\beta^2\right)\kappa^2}{4\left[\left(1+\alpha\right)^2+\beta^2\right]\left(1+\tilde{\Omega}_f^2\right)}\left[\frac{\eta_e}{\eta\left(\alpha^2+\beta^2\right)} - \frac{1}{\tilde{r}^4}\right]. \tag{3.88}$$

The corresponding solution is,

$$\tilde{\omega}_z(\tilde{r}) = C_4 K_0(\kappa\tilde{r}) + C_5 I_0(\kappa\tilde{r}) - \frac{\zeta}{2\eta} C_3 + \frac{\kappa^2}{4\left[(1+\alpha)^2+\beta^2\right]\left(1+\tilde{\Omega}_f^2\right)} \left\{ \frac{\eta_e}{\eta} + \left(\alpha^2+\beta^2\right)\mathcal{F}_1(\tilde{r}) \right\}, \quad (3.89)$$

where $I_0(\kappa\tilde{r})$ and $K_0(\kappa\tilde{r})$, are the modified Bessel function of first and second kind of order zero and

$$\mathcal{F}_1(\tilde{r}) = I_0(\kappa\tilde{r}) \int_{\Upsilon}^{\tilde{r}} \frac{K_0(\kappa\lambda)}{\lambda^3} d\lambda - K_0(\kappa\tilde{r}) \int_{\Upsilon}^{\tilde{r}} \frac{I_0(\kappa\lambda)}{\lambda^3} d\lambda. \quad (3.90)$$

The integral function $\mathcal{F}_1(\tilde{r})$ was introduced as the first integral of the right hand side of (3.90) does not have an analytical form whereas the solution of the second integral is only obtained in terms of Meijer G functions.

Using Eqn. (3.89) in Eqn. (3.87) and integrating this, we can determine the zeroth order translational velocity as

$$\tilde{v}_\theta(\tilde{r}) = \frac{2\zeta}{\eta_e \kappa} \left\{ C_4 I_1(\kappa\tilde{r}) - C_5 K_1(\kappa\tilde{r}) \right\} + \frac{\zeta\left(\alpha^2+\beta^2\right)}{2\eta_e\left[(1+\alpha)^2+\beta^2\right]\left(1+\tilde{\Omega}_f^2\right)} \left\{ \frac{\kappa^2 \mathcal{F}_2(\tilde{r})}{\tilde{r}} + \frac{\eta_e \tilde{r}}{2\eta\left(\alpha^2+\beta^2\right)} - \frac{1}{2\tilde{r}^3} \right\} - \frac{\tilde{r}\zeta C_3}{2\eta} + \frac{C_6}{\tilde{r}}, \quad (3.91)$$

where $\mathcal{F}_2(\tilde{r})$ is given by

$$\mathcal{F}_2(\tilde{r}) = \int_{\Upsilon}^{\tilde{r}} \beta \left\{ I_0(\kappa\beta) \int_{\Upsilon}^{\beta} \frac{K_0(\kappa\lambda)}{\lambda^3} d\lambda - K_0(\kappa\beta) \int_{\Upsilon}^{\beta} \frac{I_0(\kappa\lambda)}{\lambda^3} d\lambda \right\} d\beta. \quad (3.92)$$

Next we obtain expressions for the constants C_3, C_4, C_5, and C_6, using the boundary conditions at the inner surface of the external cylinder ($\tilde{r} = 1$) and at the outer surface of the inner cylinder ($\tilde{r} = \Upsilon$) assuming that $\gamma = 0$ (zero spin slip)

$$\tilde{v}_\theta(\Upsilon) = 0,\ \tilde{v}_\theta(1) = 0, \quad (3.93)$$
$$\tilde{\omega}_z(\Upsilon) = 0,\ \tilde{\omega}_z(1) = 0.$$

In this form was obtained that

$$C_3 = \frac{\tilde{\Omega}_f}{\boldsymbol{\Xi}} \left\{ \kappa I_0(\kappa\Upsilon) \left[\kappa \left(\eta\Psi + \Upsilon^2 (\eta_e - \eta\Psi) \right) K_0(\kappa) + 2\Upsilon^2 \eta_e K_1(\kappa) \right] - 4\Upsilon^2 \eta_e \right.$$
$$\kappa^2 \left[\Upsilon^4 \eta_e I_2(\kappa\Upsilon) K_0(\kappa) + \left(\Upsilon^2 \eta_e I_2(\kappa) - \left(\Upsilon^2 - 1 \right) \eta\Psi I_0(\kappa) \right) K_0(\kappa\Upsilon) \right.$$
$$\left. - \Upsilon^4 \eta_e I_0(\kappa) K_2(\kappa\Upsilon) \right] + 2\Upsilon^2 \eta\kappa^2\Psi \left[(\kappa I_1(\kappa) K_0(\kappa\Upsilon) + \kappa I_0(\kappa\Upsilon) K_1(\kappa) - 1) \mathcal{F}_1(1) \right.$$
$$\left. \left. + \kappa^2 \left(I_0(\kappa\Upsilon) K_0(\kappa) - I_0(\kappa) K_0(\kappa\Upsilon) \right) \mathcal{F}_2(1) \right] \right\}, \quad (3.94)$$

$$C_4 = \frac{\tilde{\Omega}_f \kappa^2}{2\boldsymbol{\Xi}} \left\{ \Upsilon^2 \kappa\Psi \left[2\zeta \left(K_1(\kappa) - \Upsilon K_1(\kappa\Upsilon) \right) - \eta_e \kappa \left(\Upsilon^2 - 1 \right) K_0(\kappa\Upsilon) \right] \mathcal{F}_1(1) + \right.$$
$$\left. \left[2\Upsilon^2 \zeta\kappa^2\Psi \mathcal{F}_2(1) + \left(\Upsilon^2 - 1 \right) \left(\Upsilon^2 \eta_e - \zeta\Psi \right) \right] \left[K_0(\kappa) - K_0(\kappa\Upsilon) \right] \right\}, \quad (3.95)$$

$$C_5 = \frac{\tilde{\Omega}_f \kappa^2}{2\boldsymbol{\Xi}} \left\{ \Upsilon^2 \kappa\Psi \left[2\zeta \left(I_1(\kappa) - \Upsilon I_1(\kappa\Upsilon) \right) + \eta_e \kappa \left(\Upsilon^2 - 1 \right) I_0(\kappa\Upsilon) \right] \mathcal{F}_1(1) + \right.$$
$$\left. \left[2\Upsilon^2 \zeta\kappa^2\Psi \mathcal{F}_2(1) + \left(\Upsilon^2 - 1 \right) \left(\Upsilon^2 \eta_e - \zeta\Psi \right) \right] \left[I_0(\kappa) - I_0(\kappa\Upsilon) \right] \right\}, \quad (3.96)$$

$$C_6 = \frac{\tilde{\Omega}_f \zeta}{2\eta_e \boldsymbol{\Xi}} \left\{ 2\Upsilon^3 \kappa \left(\eta_e + \zeta\Psi \right) I_1(\kappa\Upsilon) K_0(\kappa) - 2 \left(\Upsilon^2 + 1 \right) \left(\Upsilon^2 \eta_e + \zeta\Psi \right) + \kappa I_0(\kappa\Upsilon) \right.$$
$$\left[2K_1(\kappa) \left(\zeta\Psi + \Upsilon^4 \left(\eta_e + \eta\kappa^2\Psi \mathcal{F}_1(1) \right) \right) + \kappa\Psi K_0(\kappa) \left(\eta_e - \Upsilon^4 \eta_e + 2\Upsilon^4 \eta\kappa^2 \mathcal{F}_2(1) \right) \right] +$$
$$\kappa I_0(\kappa) \left[\kappa\Psi K_0(\kappa\Upsilon) \left(\left(\Upsilon^4 - 1 \right) \eta_e - 2\Upsilon^4 \eta_e \kappa^2 \mathcal{F}_2(1) \right) - 2\Upsilon^3 K_1(\kappa\Upsilon) \left(\eta_e + \zeta\Psi - 2\zeta\kappa^2\Psi \right) \mathcal{F}_2(1) \right] +$$
$$2\kappa I_1(\kappa) \left(\zeta\Psi\kappa^2 \Upsilon^4 K_2(\kappa\Upsilon) \mathcal{F}_1(1) + K_0(\kappa\Upsilon) \left(\zeta\Psi + \Upsilon^4 \left(\eta_e + \eta\kappa^2\Psi \mathcal{F}_1(1) \right) \right) \right) +$$
$$\left. 2\Upsilon^2 \kappa^2\Psi \left(2\zeta \mathcal{F}_2(1) - \eta_e \mathcal{F}_1(1) + \Upsilon^2 \zeta\kappa I_2(\kappa\Upsilon) \left(K_1(\kappa) \mathcal{F}_1(1) + \kappa K_0(\kappa) \mathcal{F}_2(1) \right) \right) \right\}, \quad (3.97)$$

Where

$$\boldsymbol{\Xi} \equiv 4\Upsilon^2 \tilde{\Omega}_f \kappa\zeta \left(1 + \tilde{\Omega}_f^2 \right) \left[(1+\alpha)^2 + \beta^2 \right] \left\{ \frac{\eta_e \kappa \left(\Upsilon^2 - 1 \right)}{2\zeta} \left[I_0(\kappa) K_0(\kappa\Upsilon) - K_0(\kappa) I_0(\kappa\Upsilon) \right] \right.$$
$$\left. - \frac{2}{\kappa} + \Upsilon I_1(\kappa\Upsilon) K_0(\kappa) + I_1(\kappa) K_0(\kappa\Upsilon) + K_1(\kappa) I_0(\kappa\Upsilon) + \Upsilon I_0(\kappa) K_1(\kappa\Upsilon) \right\} \quad (3.98)$$

and

$$\Psi \equiv \alpha^2 + \beta^2. \tag{3.99}$$

3.2.5 Torque on the inner cylinder

As was shown in Chapter 2, the surface excess magnetic forces do not contribute to the measured torque due to the continuity of the normal magnetic flux and the tangential component of magnetic field intensity in the wall-fluid interface. Therefore, the torque is due to the symmetric and antisymmetric parts of the stress tensor and couple stresses and is given by

$$L_z = \mu_0 \chi_i K^2 \tilde{\Omega}_f R_O^2 l \int_0^{2\pi} \int_0^1 \left[\frac{\eta}{\zeta} \tilde{r}^2 \frac{d}{d\tilde{r}} \left(\frac{\tilde{v}_\theta}{\tilde{r}} \right) + \zeta \frac{d}{d\tilde{r}} \left(\tilde{r} \tilde{v}_\theta \right) - 2\tilde{r}\tilde{\omega}_z + \frac{4\eta}{\eta_e \kappa^2} \frac{d\tilde{\omega}_z}{d\tilde{r}} \right] \tilde{r} d\theta d\tilde{z}. \tag{3.100}$$

Substituting the expressions for spin and translational velocity in Eqn. (2.53) and integrating the z-directed torque over the internal cylinder surface yields

$$\begin{aligned} L_z = \left(\mu_0 K^2 \pi R_O^2 l \right) & \frac{\chi_i \tilde{\Omega}_f \left[4\tilde{\Omega}_f^2 + (2+\chi_i)^2 \right]}{\Upsilon^2 \eta_e \left(1 + \tilde{\Omega}_f^2 \right) \left[4\tilde{\Omega}_f^2 + (2 + \chi_i + \Upsilon^2 \chi_i)^2 \right]} \\ & \left\{ \frac{\Upsilon^4 (\zeta + 2\eta) \chi_i^2}{(2+\chi_i)^2 + 4\tilde{\Omega}_f^2} - \Upsilon^4 \eta_e - \frac{4\Upsilon^2 \eta \eta_e \left(1 + \tilde{\Omega}_f^2 \right) \left[4\tilde{\Omega}_f^2 + \left(2 + \chi_i + \Upsilon^2 \chi_i \right)^2 \right]}{\zeta \left[(2+\chi_i)^2 + 4\tilde{\Omega}_f^2 \right]} C_6 \right\} + \mathcal{O}(\varepsilon). \end{aligned} \tag{3.101}$$

Thus, the torque expression obtained has a power two dependence on the amplitude of the magnetic field and an approximately linear dependence with the dimensionless frequency as $\tilde{\Omega}_f^2 \to 0$.

3.2.6 Theoretical predictions for spin and translational velocity

Spin and azimuthal velocity profiles are shown in Figs. 3-2 and 3-3. These were obtained using values for physical and magnetic properties given in Table 4.1 and 4.2, for a frequency of 85 Hz and amplitude of the magnetic field of 5 mT rms, for which $\varepsilon = 0.142$. Figure 3-5 shows the dependence of flow on the dimensionless parameter κ for values of 20, 40, and 50. In order to obtain these velocity profiles, we used the commercial package Mathematica® to numerically integrate the functions given by Eqns. (3.90) and (3.92). However, because the integrand of

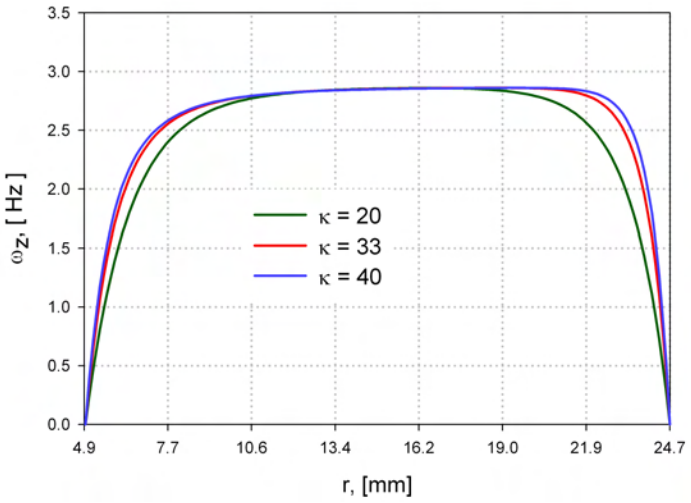

Figure 3-2: Spin up velocity profiles for ferrofluid in the annular gap of two coaxial cylinders for 85 Hz and 5 mT rms of applied magnetic field. These were obtained using physical and magnetic porperties of the EMG705 ferrofluid and values of the dimensionless parameter κ of 20, 35 and 50.

these functions changes rapidly for high values of κ, especially near $\tilde{r} = 1$, the numerical values of these functions are inaccurate for values of $\kappa > 50$.

The spin velocity profiles presented in Fig. 3-2 show orders of magnitude similar to those predicted for spin up, however, in this case the spin velocity is not uniform throughout the annular gap due to the radial dependence of the magnetic couple. In addition, a boundary layer forms close to both cylinders walls. Translational velocity profiles in Fig. 3-3 show the expected behavior with the dimensionless parameter κ, that is $v_\theta \to 0$, when $\kappa \to \infty$ or $\eta' \to 0$. Of note is the change in flow direction close to the wall of the internal cylinder and the decrease in the flow with reduction of the annular gap as illustrated in Fig. 3-5. The latter is contrary to predictions for spin up flow where the magnitude of the flow increases with reduction of the container radius. Both predictions can be used in the experimental assessment of the theory.

This analysis is valid for $\varepsilon \ll 1$ as higher order terms of the regular perturbation method were not obtained. Nevertheless, as is known, the zeroth order solution in the regular perturbation method is the principal contribution to the solution allowing to obtain valuable insight into

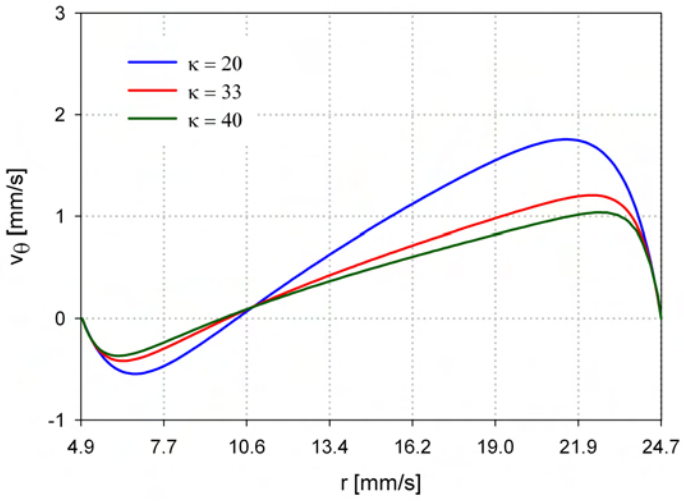

Figure 3-3: Translational velocity profiles for ferrofluid in the annular gap of two coaxial cylinders for 85 Hz and 5 mT rms of the applied magnetic field. These were obtained using physical and magnetic properties of the EMG705 ferrofluid and values of the dimensionless parameter κ of 20, 35, and 50.

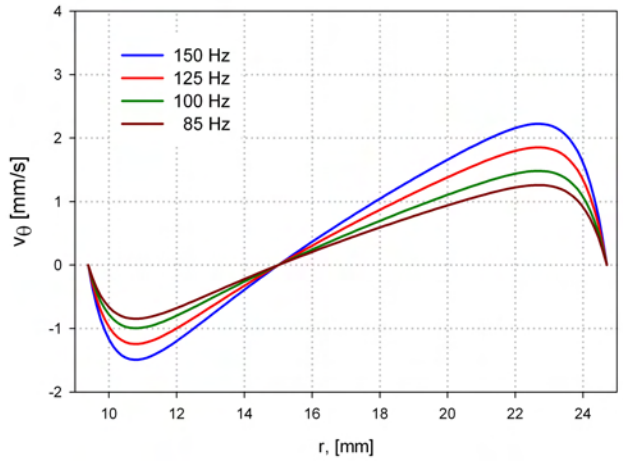

Figure 3-4: Effect of the frequency of the magnetic field on velocity profiles obtained using $\kappa = 33$ and properties of the EMG900-1 ferrofluid.

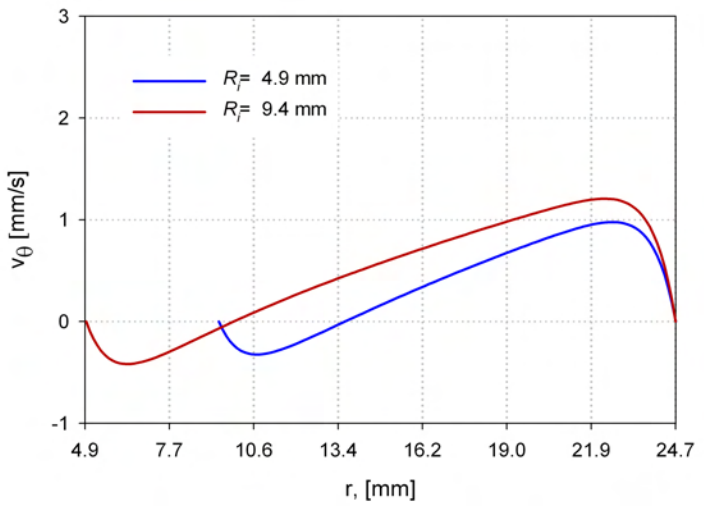

Figure 3-5: Translational velocity profiles showing the effect of Υ on flow magnitude for 85 Hz and 5 mT rms of the applied magnetic field. These were obtained using physical and magnetic properties of the EMG705 ferrofluid and $\kappa = 50$.

the characteristics of the flow. Thus, our zeroth order solution for annular flow imply that this analysis is valid only for low fields where $\mathbf{M}$ is assumed proportional to $\mathbf{H}$ and that the term for spin magnetization coupling $\boldsymbol{\omega} \times \mathbf{M}$ in the magnetization equation is negligible. Solutions for the first order contribution were not obtained as higher harmonics are introduced in the magnetization equation due to the radial dependence of the magnetization and the magnetic field, giving greater complexity to the problem and small insight.

Chapter 4

Ferrofluid characterization and experimental setup

In this Chapter, we describe and summarize the physical and magnetic characterization of the ferrofluids used in the rheological measurements and the experimental setup used to obtain velocity profile measurements. Magnetic characterization is based on measuring magnetization curves and the asymptotic approximations of the Langevin equation in the limit of low and high fields. These asymptotic approximations are used in order to estimate the range for the particle diameter assuming monodisperse ferrofluids. In addition, we used the method of Chantrell *et al.* [65] together with direct measurements of the particle diameter from TEM to determine an effective particle diameter.

Several estimates for the Brownian and Néel relaxation times were obtained using particle diameters obtained from asymptotic approximations, Chantrell's method, and from new expressions that include the effect of polydispersity in both relaxation processes.

4.1 Physical characterization

Two commercial concentrated ferrofluids, EMG705 and EMG900, were obtained from Ferrotec Corporation (Nashua, NH. USA). These consist of magnetite (Fe_3O_4) nanoparticles suspended in water (EMG705) and oil (EMG900) respectively. In order to obtain fluids with different physical and magnetic properties these ferrofluids were diluted using deionized water for EMG705

and a suitable solvent for EMG 900, also obtained from Ferrotec. Stability of the ferrofluid is a requirement in order to ensure the validity of our experimental results. Thus, fluid characterization and rheological measurements were carried out within weeks of receiving the ferrofluids to avoid particle agglomeration, which commonly occurs in commercial water based ferrofluids.

4.1.1 Mass density and shear viscosity measurements

Mass density measurements were obtained gravimetrically while the shear viscosity coefficient was obtained using a STRESSTECH HR rheometer with double gap geometry. Figures 4-1 and 4-2 show measurements of shear viscosity vs shear rate (measured between 10 to 110 s^{-1}) for EMG705, EMG900, and their dilutions. The fact that the shear viscosity is constant for the range of shear rate measured suggests that these ferrofluids are Newtonian in the absence of a magnetic field. Density and shear viscosity values for all ferrofluids are summarized in Table 4.1.

4.1.2 Speed of sound in ferrofluids

The value of the speed of sound in ferrofluids is required as a parameter in the DOP2000 used to determine the bulk velocity profiles. Measurements of the speed of sound in ferrofluids as a function of temperature and weight fraction of magnetite particles have been reported in the literature [66,67]. Their results showed that contrary to the behavior of most liquids, the speed of sound in ferrofluids decreases with increasing temperature while an increase in the weight fraction of magnetite particles resulted in a decrease of the sound velocity throughout the fluid. This behavior was attributed to the presence of the magnetite particles in the ferrofluid.

Sound velocity was measured using a cell unit attached to the DOP2000, similar to that shown in Fig. 4-3. This measurement is based on phase analysis of an echo generated by a mobile screw when it is moved over a known distance. The sound velocity obtained for EMG705 and EMG900-1 are shown in Table 4.1 and are in agreement with the results reported by [66].

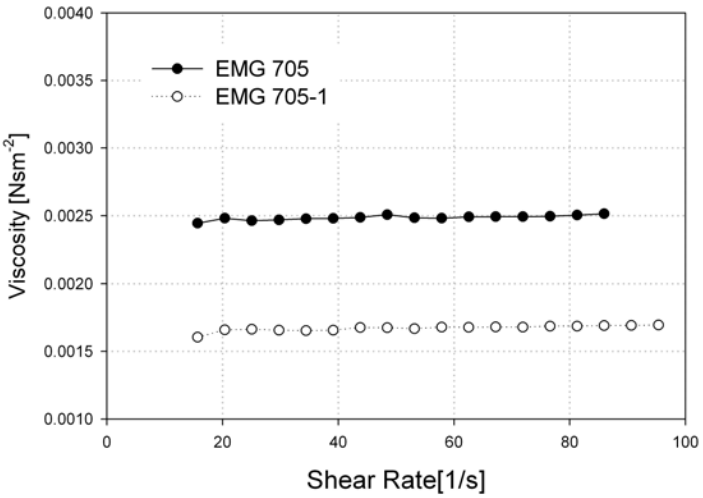

Figure 4-1: Plots of viscosity vs shear rate for EMG705 and EMG705-1, showing Newtonian behavior in absence of magnetic field.

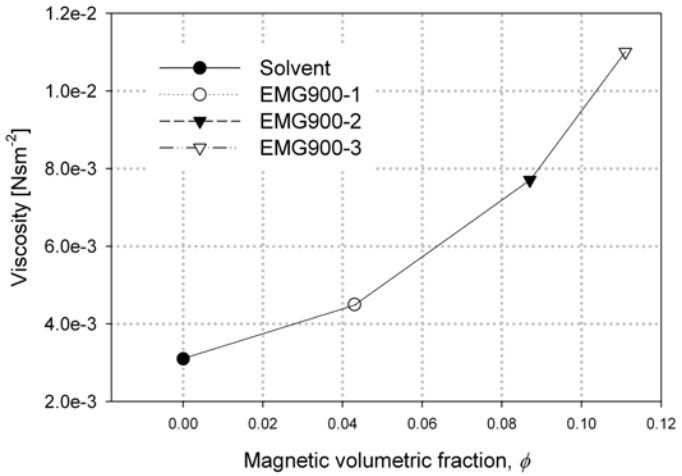

Figure 4-2: Plots of viscosity vs magnetic volume fraction for EMG900-1, EMG900-2, EMG900-3, and the dilution solvent.

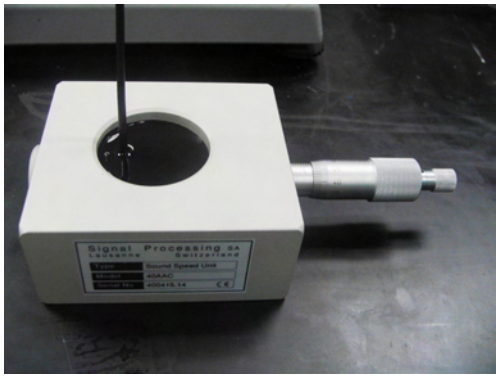

Figure 4-3: Speed of sound unit used with the DOP2000 machine. An ultrasonic transducer is placed in front of a movable screw. An ultrasound beam is emitted from the transducer while the screw is displaced a known distance. The sound velocity is obtained from the change in phase of the echo received due to displacement of the screw.

4.2 Magnetic characterization

4.2.1 Saturation magnetization, initial susceptibility, and magnetic volume fraction

The magnetic properties of the ferrofluids were measured using a MPMS-XL7 Super Conducting Quantum Interference Device (SQUID) magnetometer (Quantum Design, San Diego, CA, USA) at 300 K. The results are shown in Fig. 4-4, for water based ferrofluid, where the abscissa corresponds to internal magnetic field, obtained from external magnetic field using the relation, $H_i = H_e - DM$ with a demagnetization factor D of 0.5 [13][1]. The inset in Fig. 4-4 shows the linear relation between magnetization and applied field at low magnetic fields. From the high-field asymptote of the magnetization curve we obtained values for the saturation magnetization M_s of the ferrofluids. The magnetic volume fractions were estimated using the relation $M_s = \phi M_d$, and a value of 446 kA/ m for the domain magnetization of magnetite. The initial susceptibility of each fluid was obtained from the low field slope of the magnetization curve. These results are summarized in Table 4.1.

[1] Demagnetization effects are due to effective magnetic charge induced on the surface of a magnetic material, with magnetization M, that contributes a magnetic field that partially cancels the externally applied magnetic field.

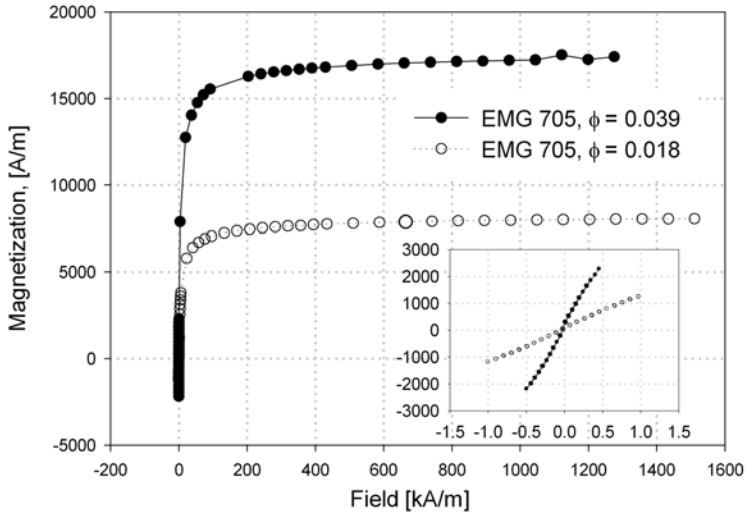

Figure 4-4: Magnetization curve for the water based ferrofluid EMG 705. The inset shows the low field response of the ferrofluid

4.2.2 Magnetic particle diameter

In the literature, it is common to estimate the magnetic particle size range using magnetization curves and asymptotic expressions for the Langevin equation in the limit of low ($\alpha \ll 1$) and high fields. The particle diameter is estimated from magnetization curves and asymptotic approximation of the Langevin equation in the linear region at low fields ($\alpha \ll 1$)

$$\chi_i = \frac{\pi}{18}\phi\mu_0\frac{M_d^2 D_p^3}{k_B T}, \tag{4.1}$$

and from the asymptotic form of the Langevin equation for high fields

$$M = \phi M_d\left(1 - \frac{6k_B T}{\pi\mu_0 M_d D_p^3}\frac{1}{H}\right). \tag{4.2}$$

The value of D_p estimated using Eqn. (4.1) is always higher than that estimated using Eqn. (4.2). This is because at low fields larger particles are more easily oriented by the field whereas for high fields fine particles contribute more to the changes in magnetization [1]. The range of D_p estimated using this method is reported in Table 4.2. In addition, the median particle diameter

Table 4.1: Physical and magnetic properties at room temperature for water and kerosene based ferrofluid

Ferrofluid	$c, [\,\mathrm{m/s}]$	$\eta, [\,\mathrm{N\,s\,m^{-2}}]$	$\boldsymbol{\rho}, [\,\mathrm{kg/m^3}]$	$\mu_0 M_s, [\,\mathrm{mT}]$	$\boldsymbol{\chi}_i$	ϕ
EMG705	1450	2.5×10^{-3}	1220	21.9	4.99	0.039
EMG705-1	—	1.7×10^{-3}	1120	10.1	1.28	0.018
EMG900-1	1150	4.5×10^{-3}	1030	23.9	1.19	0.043
EMG900-2	—	7.7×10^{-3}	1270	47.8	3.63	0.087
EMG900-3	—	1.1×10^{-2}	1391	61.3	12.2	0.111

and geometric deviation were determined assuming a log-normal particle size distribution using two different methods: (i) the low and high-field asymptotes of fluid magnetization as described by Chantrell *et al.* [65], and whose expression are given respectively by,

$$D_{pgv} = \left[\frac{18 k_B T}{\pi \mu_o M_d} \sqrt{\frac{\chi_i}{3\phi M_d H_0}}\right]^{1/3}, \tag{4.3}$$

and

$$\ln \delta_g = \frac{1}{3}\left[\ln\left(\frac{3\chi_i H_0}{\phi M_d}\right)\right]^{1/2}, \tag{4.4}$$

where H_0 corresponds to the extrapolated intercept with the abscissa of a plot of M versus $1/H$ at high fields, and (ii) from direct measurements of particle diameter by TEM, Fig. 4-5. The method of Chantrell *et al.* yields the volume median diameter D_{pgv} whereas TEM measurements yield the number median diameter D_{pg}. The two are ideally related by the expression

$$\ln D_{pgv} = \ln D_{pg} + 3 \ln^2 \delta_g \tag{4.5}$$

where δ_g is the geometric deviation. Because of the existence of a "magnetically dead" layer on the nanoparticle surface, the volume median diameters and geometric deviations determined from magnetic measurements and TEM cannot be expected to agree exactly, but should be in the same order of magnitude. The estimated values for median particle diameter D_{pgv}, and the size distribution parameters obtained from magnetic measurements and TEM are summarized

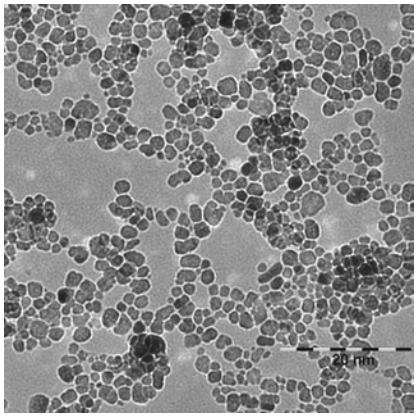

Figure 4-5: TEM image of magnetite nanoparticles in the water based ferrofluid EMG705.

in Table 4.2.

4.2.3 Relaxation times

As was mentioned before, when a magnetic field shifts in direction the magnetic moment of the particle $\mathbf{m}$ rotates due to a torque $\mu_0 \mathbf{m} \times \mathbf{H}$ which tends to align $\mathbf{m}$ and $\mathbf{H}$ [68]**.** There are two mechanisms through which the magnetic moment can attain the new equilibrium position. Brownian relaxation is a hydrodynamic process where the magnetic moment is fixed to the nanoparticle of hydrodynamic volume $V_h = \pi \left(D_p + 2\delta\right)^3 /6$ and the whole particle (magnetic core and surfactant layer of thickness δ) rotates in a fluid of viscosity η_0. This relaxation process is characterized by a Brownian time constant given by

$$\tau_B = \frac{3\eta_0 V_h}{k_B T}. \tag{4.6}$$

In the Néel relaxation mechanism the magnetic dipole rotates without rotation of the particle itself. The Néel relaxation time is given by

$$\tau_N = \frac{1}{f_0} \exp\left(\frac{K V_c}{k_B T}\right), \tag{4.7}$$

where f_0 is a characteristic frequency of the magnetic material, K is the magnetocrystalline anisotropy constant of the magnetite nanoparticles for which $K = 78\,\mathrm{kJ\,m^{-3}}$ [69], and V_c is

Table 4.2: Estimated magnetic particle diameters for water and kerosene based ferrofluid

Ferrofluid	D_p, [nm]*	D_{pgv}, [nm]†	$\ln \delta_g$ †	D_{pgv}, [nm]‡	$\ln \delta_g$ ‡
EMG705	23.0-9.7	14.9	0.535	20.1	0.288
EMG705-1	18.9-8.2	12.4	0.525	20.1	0.288
EMG900-1	13.8-6.5	9.5	0.499	14.2	0.410
EMG900-2	15.9-6.8	10.4	0.528	14.2	0.410
EMG900-3	21.9-7.2	12.5	0.608	14.2	0.410

*Determined using equations (4.1) and (4.2) and magnetization curve

†Determined using Chantrell approximation. Eqns. (4.3) and (4.4)

‡Obtained from TEM image analysis

the magnetic core volume. In a system of non-interacting particles the effective magnetic relaxation of particles with different diameters is expected to occur in parallel with an effective time constant

$$\tau = \frac{\tau_B \tau_N}{\tau_B + \tau_N}. \tag{4.8}$$

The effective relaxation constant is dominated by the faster of the two mechanisms. However, τ_B depends cubically on particle diameter whereas τ_N depends exponentially on particle diameter cubed. Hence, it can be estimated that for a typical ferrofluid with $D_p < 10\,\text{nm}$ $\tau_N \ll \tau_B$ and $\tau \simeq \tau_N$ indicating that particles relax by a Néel mechanism. Consequently for $D_p > 10\,\text{nm}$, $\tau_B \ll \tau_N$ meaning that the ferrofluid magnetization relaxes by the Brownian mechanism. The dependence of the relaxation time on the particle diameter is illustrated in Fig. 4-6.

It is important to note that the Brownian and Néel relaxation given by Eqns. (4.6) and (4.7) are for a single particle. It is of interest to estimate the effective Brownian and Néel relaxation time taking into account the effect of particle polydispersity. For this we use the expression

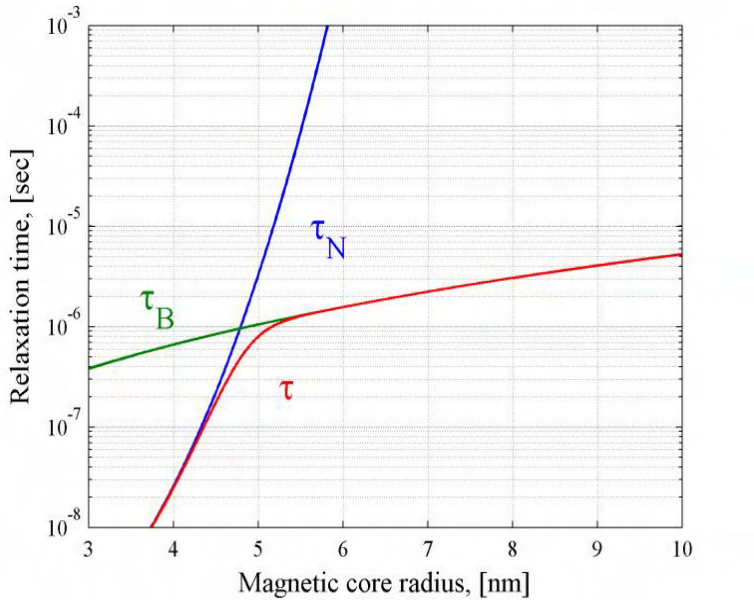

Figure 4-6: Dependence of the relaxation time on the magnetic core radius for a typical water based ferrofluid.

obtained by Rinaldi [23] for the effective Brownian relaxation time

$$\bar{\tau}_B \equiv \left[\int_0^\infty \frac{n_v\left(D_p\right)}{\tau_B\left(D_p\right)}\right]^{-1} = \frac{\pi\eta_0}{2k_BT} D_{pgv}^3 \exp\left(-9/2\ln^2\delta_g\right), \tag{4.9}$$

and effective Néel relaxation time

$$\bar{\tau}_N \equiv \left[\int_0^\infty \frac{n_v\left(D_p\right)}{\tau_N\left(D_p\right)}\right]^{-1}, \tag{4.10}$$

where $n_v\left(D_p\right)$ is the lognormal particle volume distribution function and $\tau_B\left(D_p\right)$ and $\tau_N\left(D_p\right)$ are given respectively by Eqns. (4.6) and (4.7). In deriving Eqn. (4.9) it was assumed that the particle hydrodynamic diameter is the same as the particle core diameter D_p (*i.e.*, $\delta = 0$). The effective Néel relaxation time $\bar{\tau}_N$ was estimated through numerical integration of Eqn. (4.10). The effect of an adsorbed surfactant layer δ on the effective relaxation time can be accounted by performing a numerical integration of Eqn. (4.9), with similar qualitative and quantitative results. The physical relevance of Eqns. (4.9) and (4.10) is that they illustrate the effect of

particle polydispersity (characterized by the geometric deviation δ_g) in decreasing the effective Brownian and Néel relaxation times of the collection of magnetic nanoparticles. Table 4.3 shows values of both effective relaxation times for our ferrofluid, calculated using the different methods mentioned above. In Chapters 5 and 6, the diameters determined from TEM, rather than the magnetic diameter, are used in calculations of particle size as the former represent the actual physical particle size, whereas the latter are subject to error due to the assumed value of the domain magnetization (the bulk value of magnetite is used) and the existence of the so-called magnetically dead layer on the surface of the particles.

4.3 Apparatus and experimental method

4.3.1 Magnetic field generation

Experiments were realized using the uniform rotating magnetic field generated by exciting a three-phase winding using balanced three phase currents each with 120 ° phase difference from each other. We do this by grounding one phase, exciting the remaining two phases with sinusoidal voltages at plus or minus phase difference, and letting the neutral point float. This results in balanced three phase currents in the windings to create clockwise or counterclockwise rotating magnetic fields. The amplitude, frequency, and direction of the field can be controlled using the signal generator or linear amplifier gain. The length and diameter of the stator winding were 77.7 mm and 63.6 mm respectively. The experimental setup is shown in Fig.4-7. Measurements of the magnetic fields produced by the stator, with and without ferrofluid in the cylindrical container, were made using a Gaussmeter (Sypris Test & Measurement, Orlando, FL USA) with a three-axis probe (model ZOA73). From these measurements it was determined that the stator produces a magnetic field of 4.54 mT rms per ampere rms of input current in the absence of the ferrofluid. The radial field in-homogeneity was determined to be 2.2% from axis to outer container radius at mid height, with a maximum of 6% at the top of the container, while axial field in-homogeneity was $\sim$ 4% from middle to 3/4 height and 21% to top, along the gap axis.

Table 4.3: Estimated magnetic relaxation times at room temperature for EMG705 and EMG900 and their dilutions.

Ferrofluid	$\boldsymbol{\tau}_B$ [s]^a	$\boldsymbol{\tau}_N$ [s]^b	$\bar{\tau}_B$ [s]^c	$\bar{\tau}_N$ [s]^d	$\bar{\tau}_B$ [s]^e	$\bar{\tau}_N$ [s]^e
EMG705	3.7×10^{-5} - 2.8×10^{-6}	8.0×10^{43} - 8.3×10^{-5}	3.5×10^{-7}	5.6×10^{-8}	2.1×10^{-6}	4.4×10^{-5}
EMG705-1	2.0×10^{-5} - 1.7×10^{-6}	7.1×10^{20} - 2.3×10^{-6}	2.1×10^{-7}	2.9×10^{-8}	2.1×10^{-6}	4.4×10^{-5}
EMG900-1	3.0×10^{-5} - 3.1×10^{-6}	2.4×10^{3} - 1.6×10^{-7}	3.9×10^{-7}	9.6×10^{-9}	1.9×10^{-6}	1.4×10^{-7}
EMG900-2	4.5×10^{-5} - 3.6×10^{-6}	2.1×10^{9} - 2.3×10^{-7}	4.5×10^{-7}	1.6×10^{-8}	1.9×10^{-6}	1.4×10^{-7}
EMG900-3	1.2×10^{-4} - 4.2×10^{-7}	1.6×10^{37} - 3.8×10^{-7}	5.2×10^{-7}	2×10^{-8}	1.9×10^{-6}	1.4×10^{-7}

[a]Determined using Eqn. (4.6), and particle diameter from asymptotic approximation of the Langevin Equation

[b]Determined using Eqn. (4.7), and particle diameter from asymptotic approximation of the Langevin Equation

[c]Determined using Eqn. (4.9) and D_{pgv} determined from Chantrell approximation

[d]Determined using numerical integration of the Eqn. (4.10) and D_{pgv} determined from Chantrell approximation

[e]Determined using Eqns. (4.9) and (4.10)and D_{pgv} determined from TEM

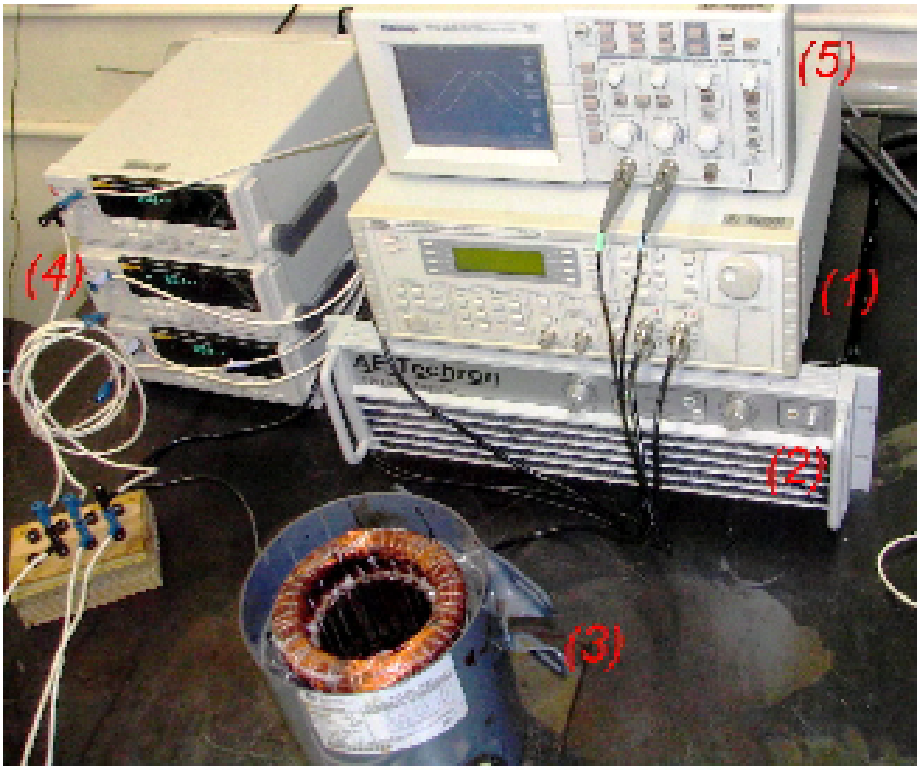

Figure 4-7: Setup used in generating a uniform rotating magnetic field, consisting of : (1) A dual channel Universal Signal Generator used to generate two low current sinusoidal signals which are amplified using (2) an AE Techron 5050 Linear Amplifier. These are used in exciting the two pole motor stator winding (3). Three Fluke 45 multimeters (4) are used to verify that the input currents to the stator winding are balanced. The oscilloscope (5) is used to verify the input signals to the linear amplifier.

4.3.2 Torque measurements

Torque measurements were made using a rotational viscometer (Brookfield Engineering Laboratories, model LV-III+, Brookfield, MA USA) as a torque meter, with a full scale range of -6.73 to 67.3 μ N m. The viscometer measures the torque needed to keep a spindle rotating at a constant angular velocity (including zero rotation). Standard spindles are made of stainless steel, which would be subject to induced eddy currents and torques in the presence of a rotating magnetic field; hence we replaced them with custom polycarbonate spindles.

For the measurements of torque in an annular space, cylindrical containers and spindles of different diameters were constructed to permit studying the effect of geometry for three values of radial aspect ratio ($\Upsilon = R_I/R_O$) whereas for the torque measurements on the inner wall of a container in spin-up flow, we replaced the solid standard spindles with customized hollow polycarbonate spindles of 12 ml and 28 ml volumes. The left hand side of Fig. 4-8 shows the hollow spindle and the right hand side shows the experimental setup for torque measurements on the external surface of a solid cylinder in annular geometry. To carry out torque measurements, the polycarbonate spindle filled with ferrofluid or the coaxial cylinders were centered in the gap of a two-pole, three-phase induction motor stator winding. In all experiments the angular velocity of the inner spindle was set to zero and the direction of the rotating field was selected in order to obtain positive torque measurements and thereby utilize the full instrument range: counterclockwise for torque measurements on the external surface of a solid spindle and clockwise for torque measurements on the inner surface of a hollow cylinder. Reversing the field rotation direction merely reversed the direction of torque and flow.

The torque required to restrain the spindle from rotating was measured for field frequencies from 25 Hz to 500 Hz and field amplitudes from 0 to 17.0 mT rms, for the two different volumes of fluid in the hollow spindles and for the three values of Υ in the coaxial cylinders geometry. This series of measurements was made for both ferrofluids and their dilutions.

4.3.3 Velocity profile measurements

The Ultrasound Velocity Profile (UVP) method has been recently developed for acquisition of instantaneous velocity fields. The method was initially developed for medical applications such as blood flow measurement. Afterwards, application was expanded to the study of liquid metal

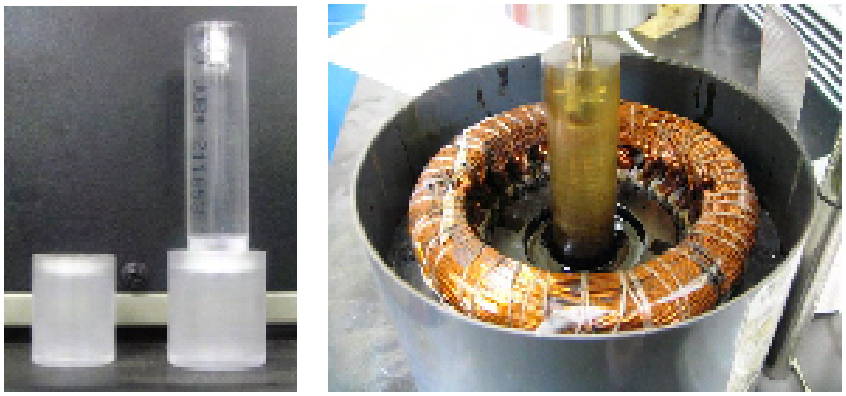

Figure 4-8: Polycarbonate spindle design to avoid confounding ferrofluid torque with induced eddy current torques. Left hand side: Polycarbonate hollow spindle for spin-up torque. Right hand side: Container and solid spindle centered inside of three phase stator winding.

flows and is now broadly used in fluid mechanical measurements. The principal advantages of the method are summarized by Takeda [70], being most relevant to our work the possibility of obtaining spatiotemporal information of the flow field and the fact that it can be applied in opaque liquids.

Bulk velocity profiles reported in Chapters 5 and 6 were measured by the UVP method using a Signal Processing DOP2000 ultrasound velocimeter (Signal Processing, Lausanne, Switzerland). This technique allows measurement of velocity profiles in opaque liquids, such as ferrofluids. An ultrasonic pulse is emitted periodically from a transducer and sent through the fluid. Echoes due to tracer particles are recorded by the same transducer. The equipment measures the component of the velocity vector parallel to the direction of beam propagation, with the spatial location being determined from the time delay between emitted burst and recorded echo, and the velocity is obtained from the corresponding Doppler frequency shift. The velocity signal is positive when tracers are moving away from the probe. Assuming that flow is purely in the azimuthal direction, an assumption that is supported by our experiments, the relation between parallel and azimuthal velocities is given by

$$v_{\parallel} = v_{\theta} \cos \varphi. \tag{4.11}$$

From the geometry of the problem, illustrated in Fig. 4-9, $\cos \varphi$ can be expressed as a function of the radius of the external cylinder R_O and the angle β between the propagation

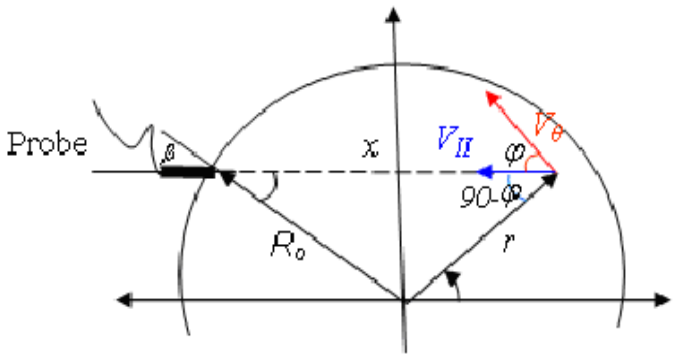

Figure 4-9: Sketch of experimental geometry used to obtain the relation between parallel and azimuthal velocity components in a cylindrical container, assuming there is no radial flow.

direction of the ultrasonic beam and the diagonal of the cylinder resulting in $\cos\varphi = R_O \sin\beta / r$. Replacing this expression in Eqn. (4.11), the azimuthal component v_θ of the velocity can be related to the measured velocity by:

$$v_\theta = v_\parallel \frac{\sqrt{R_O^2 + x_p^2 - 2R_O x_p \cos\beta}}{R_O \sin\beta} \tag{4.12}$$

Minute amounts of polyamide powder were used as tracers, such that the estimated weight fraction of tracer particles was less than 0.00015, in order to prevent phenomena such as is found in so-called inverse ferrofluids [71–74]. These micro-particles had a mean diameter of $15-20\mu$m and a density close to that of our ferrofluid, to avoid settling or buoying. In addition, these polyamide particles reflect ultrasound efficiently as their acoustical impedance is different from that of the ferrofluid [75].

Container design

In the design of the containers used for measurements of velocity profiles several factors were taken into account:

i) Container material: polycarbonate was chosen as the material for the containers because its acoustic impedance is similar to that of the ferrofluid as can be seen in Table 4.5. This avoids reflection of acoustic energy at the wall-fluid interface, producing saturation of the transducer

receiver and loss in resolution.

ii) Ultrasound probe position: we placed the probes external to the flow. This avoids the perturbation of the flow field due to a protruding probe. The design is provided with slots in the outside of the container, each slot at a specific angle with respect to the diagonal. It is necessary to take into account the diffraction of the ultrasound beams in the polycarbonate-ferrofluid interface. In obtaining the correct angle β we used the Snell-Descartes Law

$$\frac{\sin\vartheta}{c_p} = \frac{\sin\beta}{c_f},$$

where ϑ is the angle of incidence, β is the angle of refraction, c_p is the speed of sound in the polycarbonate and c_f is speed of sound of the fluid contained in the container. Table 4.4 summarizes the values for the incident (machined in the container) and refracted angle for both ferrofluid types and Appendix B details the way in wich the angles of the machined slot were measured. The value of the β angle is used in the figures of Chapters 5 and 6 as the angle of the ultrasound beams for each ferrofluid.

iii) Container size: The inner diameter and height of the container are 49.4 mm and 63.5 mm respectively. The diameter is limited by the stator winding diameter and the length of the ultrasound probe as can be observed in the right hand side of Fig. 4-10.

iv) Cover: This was used in some experiments to suppress surface effects such as those observed by [17]. This cover was made with a convex inner surface. A vent tube was placed in the center to avoid air bubbles at the interface. In addition, other covers were made that allowed placing an axial probe to carry out velocity measurements in the axial direction and the inclusion of an inner cylinder for measurements of velocity profile in the annular geometry.

4.3.4 Limitations of the DOP 2000

The limitations of the UVP method are the inability of obtaining measurements within 5 to 8 mm of the ultrasonic transducer and inaccuracies in the velocity measurements at the far wall (in the boundary of the container). The first limitation is due to the ringing effect of the ultrasonic transducer which follows immediately after the emission of the pulse. This results in saturation of the transducer preventing measurements at depths located just a few millimeters

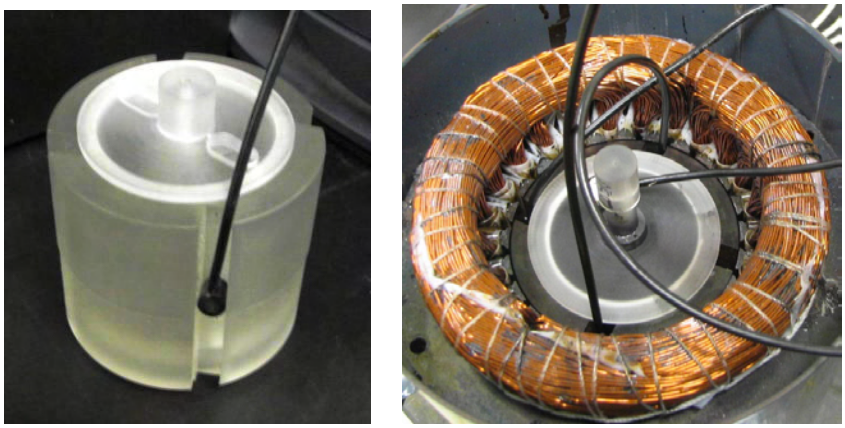

Figure 4-10: Left: photographic showing the designed polycarbonate container and cover used in order to obtain velocity profile measurements in the spin up geometry. Right: Experimental setup to obtain velocity profiles in annular geometry.

Table 4.4: Values for three different ultrasound beams incident angles machined in the polycarbonate container and refracted beams for glycerol, water and kerosene based ferrofluids.

Incidence Angle	$\boldsymbol{\beta}$ **for Glycerin**	$\boldsymbol{\beta}$ **for EMG705**	$\boldsymbol{\beta}$ **for EMG900-1**
$\vartheta_1 = 9.98$	$\beta_1 = 9.31$	$\beta_1 = 7.08$	$\beta_1 = 5.22$
$\vartheta_2 = 16.55$	$\beta_2 = 15.42$	$\beta_2 = 11.70$	$\beta_2 = 8.60$
$\vartheta_3 = 20.19$	$\beta_3 = 18.80$	$\beta_3 = 14.21$	$\beta_3 = 10.43$

Table 4.5: Acoustic properties of plastic and liquid involucre in the flow experimental setup.

Material	**c** [mm/ μs]	**z** [**MRayls**][1,2]	ρ[g/ cm^3]
water to 25 °C	1.497	1.49	0.998
Kerosene	1.324	1.07	0.810
Polycarbonate	2.270	2.77	1.220
Nylon 6/6	2.600	2.90	1.120
Steel Stainless	5.790	45.70	7.890

[1]Impedance acoustic is given by $z = \rho c$

[2]Typical units of z is **MRayls** $=10^6\,\mathrm{kg\,s^{-1}\,m^{-2}}$

This properties value were taken from [76]

from the surface of the transducer. The second limitation is due to the influence of the far wall. This phenomenon can be explained using the illustration of the right hand side in Fig 4-11. The ultrasonic beam BC reflected by the far interface transform this interface in a transmitter. The same particles contained in the liquid will backscatter energy a second time in the direction of the transducer. The depth associated to the path ABC is located outside the flowing liquid. Imaginary velocity components are added to the real velocity profile affecting the measurements of velocities near the far interface. This phenomenon explains why it is impossible to obtain a zero velocity value at the far wall. Reflections of the ultrasonic wave travelling inside of the container wall can also be registered by the transducer as is exemplified in the right hand side of Fig. 4-11. This phenomenon appears if the difference in the acoustic impedance between the liquid and the interface is high, introducing additional saturation of the transducers and loss in depth resolution [77, 78].

4.3.5 Operating parameters

Transducers used in the experiments had an emission frequency of 4 MHz, a case diameter of 8 mm, and a length of 10 mm. With few exceptions, we used a pulse repetition frequency of

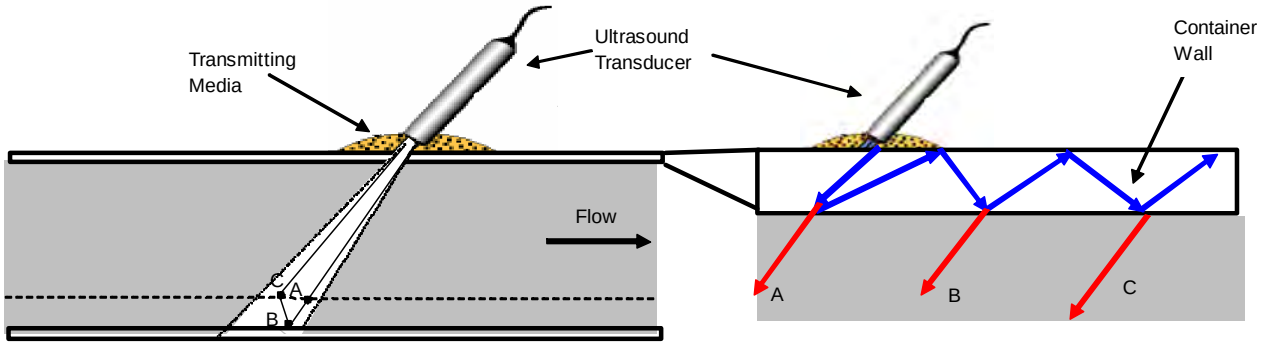

Figure 4-11: Influence of interfaces on velocity profiles. Left, illustrate the effect of the far away wall which is transformed in a transmitter resulting in imaginary velocity values outside of the boundary that contain the fluid. Right, illustrate the effect of internal reflections inside of the container wall that arisen as consequence of higher difference between the acoustic impedance of fluid and that of the container material resulting in longer saturation of the ultrasonic probe and lost resolution depth. This figure was taken and modified of the DOP2000 user's manual.

200 Hz, taking 100 emissions per profile and averaging over 70 profiles to obtain our reported results. The spatial resolution in the DOP2000 is defined as the distance between the center of adjacent sampling volumes and not as the thickness of the sampling volume. The physical resolution which is directly linked to the burst direction (display resolution) was chosen as 0.363 mm in all experiments. If the longitudinal size of the sampling value is shorter than the display resolution, then exist areas in the profile where no information is received (holes). If the opposite case occurs the sampling volumes overlap and all the way along the direction of beam propagation velocity is sampled. As can be seen in Table 4.6 for all our experiments the sampled volumes overlap. The spatial resolution transverse to beam propagation is set by the diameter of the emitter element and was approximately 3 mm. The set of parameters used in our measurements is summarized in Table 4.6.

4.3.6 Accuracy and reproduction of the velocity profiles

The DOP2000 does not require calibration using a standard velocity profile because the velocity is obtained from echo information. However, we verified the correct operation of the experimental setup by measuring the velocity profile for glycerin in a cylindrical Couette flow geometry. Figure 4-12 shows velocity profiles obtained using the experimental setup described above and

Table 4.6: Paremeters used in the DOP2000 in order to obtain velocity profile measurements of EMG705 and EMG900-1 ferrofluids.

Emitting frequency	4 MHz
Wavelength in water ($\lambda = c_{EMG705}/f_e$)	0.363 mm
Wavelength in Kerosene ($\lambda = c_{EMG900}/f_e$)	0.288 mm
Pulse repetition frequency (F_{frp})	200 Hz
Maximum measurable Velocity $V_{\max} = F_{frp}c_{EMG705}/(2f_e)$	18.12 mm/ s for EMG705
Maximum measurable Velocity $V_{\max} = F_{frp}c_{EMG900}/(2f_e)$	14.38 mm/ s for EMG705
Number of emitted cycles	8 Cycles
Length emitted burst	8 Cycles/$f_e = 2 \times 10^{-6}$ s
Sampling Volume: Longitudinal size for EMG705	2×10^{-6} s $* c_{EMG705} = 1.45$ mm
Sampling Volume: Longitudinal size for EMG900	2×10^{-6} s $* c_{EMG900} = 1.15$ mm
Sampling Volume: Lateral size	3 mm

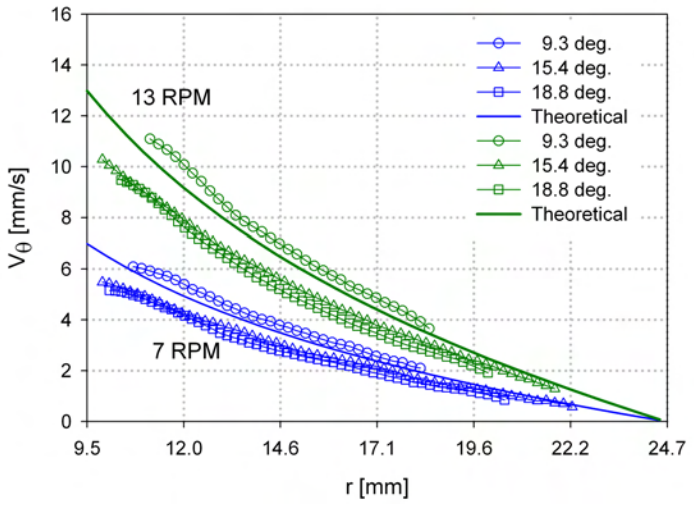

Figure 4-12: Theoretical and experimental velocity profiles for glycerin in Couette geometry for 7 **RPM** and 13 **RPM** rotation rate of the inner cylinder. The ultrasound probes were placed to three different incident angles at half of height of the container.

placing three probes at mid-heigt of the container at three different angles as reported in Table 2.6. The rotation rate of the inner spindle was selected 7 **RPM** and 13 **RPM** which allow us to obtain velocities of magnitude similar to those obtained with ferrofluids in Chapters 5 and 6.

These velocity profiles show that the shape of the profile is well reproduced for all positions of the probes. The small difference between the velocity profiles for the different angles can be due to the rotation of the inner cylinder, which may not be perfectly centered. In addition, the fact that the inner cylinder is rotating induce negative effects that contributed to change the shape of the profile near to the inner cylinder [79]. In spite of these, velocity profile were found in good agreement with the theoretically predicted values.

Chapter 5

Experimental measurements of torque and velocity profile for ferrofluid in a cylindrical container under rotating magnetic field

5.1 Velocity profile measurements

Conventional techniques used for characterization of flow profiles are based on optical methods such as Laser-Doppler Anemometry (LDA), or flow visualization techniques, such as Particle Image Velocimetry (PIV). Unfortunately, these are not applicable to opaque liquids such as ferrofluids in which light does not penetrate. It is because of this limitation that prior research has focused on the free surface of open containers [17, 18, 28, 32]. Surface velocity profile measurements have been made using tracers suspended in the surface of the ferrofluid to visualize the flow. Velocities of tracers suspended on the surface of the ferrofluid are registered by means of a video camera placed overhead. The displacement of the tracers in a determined time interval can be obtained and hence a distribution of velocities [26]. This technique has been shown to be inadequate for the study of ferrofluids because of free-surface effects in rotating magnetic fields. Velocity profiles were measured for the ferrofluid in a cylindrical container made

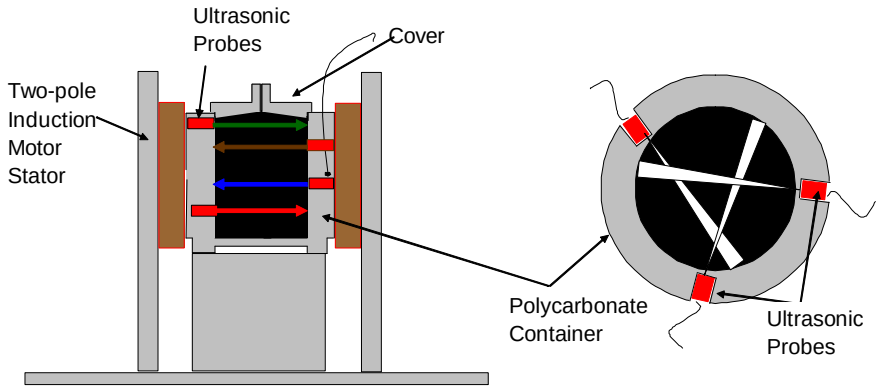

Figure 5-1: Illustration of the experimental setup for measurements of velocity profiles of ferrofluids in a cylindrical container and subjected to a uniform rotating magnetic field. Left: Container with transducers located inside a two-pole induction motor stator. Right: Top view showing transducers at different incident angles. The transducers are separated from the ferrofluid by a thin polycarbonate wall.

of polycarbonate and with dimensions of 49.4 mm inner diameter and 60 mm height. Our apparatus design permitted simultaneous measurement of velocity profiles relative to ultrasonic beams propagating at three distinct angles (using three ultrasonic transducers) relative to the diagonal, as illustrated in Fig. 5-1. A cover was used to eliminate the free surface and thereby avoid interfacial effects which could confound our measurements.

The rotating magnetic field was generated using the three-phase, two-pole magnetic induction motor stator winding described in Chapter 4. Experiments were carried out for field frequencies between 20 and 120 Hz and amplitudes between 8.3 mT rms and 14.3 mT rms.

The first set of experiments was made in such a way as to allow us to verify the existence, direction, and uniformity of the flow in the bulk of the fluid. To this end, we used three transducers, at angles of 7.1°, 11.7°, and 14.2° placed at half the height of a container with cover. In this experiment the direction of field rotation was set counterclockwise so that a positive velocity measurement implied co-rotation of field and fluid. As is observed in Fig. 5-2 and for the whole interval of frequencies and amplitude of the magnetic field studied, we always found co-rotation of field and fluid in the bulk of the fluid and a linear dependence of the velocity with radial position (i.e., rigid-body-like motion) over most of the fluid.

In addition, the velocity profiles measured by each one of the transducers superimpose,

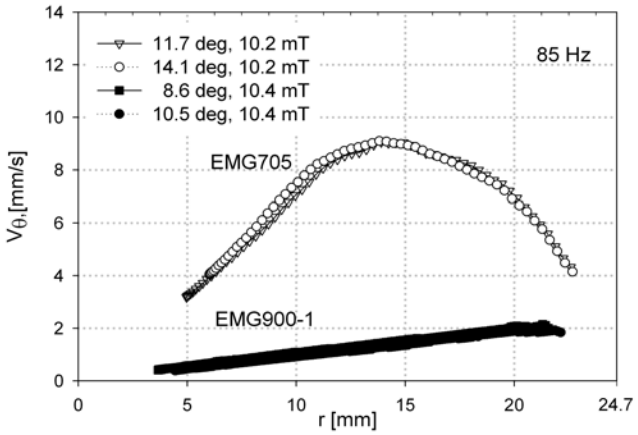

Figure 5-2: Experimental velocity profiles for EMG705 and EMG900-1 ferrofluids. Ultrasonic transducers were placed at half the height of the container. Angles are with respect to the diagonal.

indicating that the flow is uniform and azimuthal in the plane. Another important observation of these experiments (Fig. 5-2), is that the velocity maximum occurs at different radial positions for the two fluids, even under identical experimental conditions. This is important as the expression for flow obtained by Pshenichnikov *et al.* [31] does not predict variation in the maximum position with fluid type. The results of similar experiments at various field frequencies and amplitudes are shown in Figs. 5-3 and 5-4, where a single probe angle is shown for simplicity as all three probes provide similar results.

Next, we measured the azimuthal velocity profiles at four different heights by using probes at h, $3/4h$, $1/2h$ and $1/4h$ ($h = 63.5\,\mathrm{mm}$ being the container height), and the axial velocity profile v_z using probes placed on the cover of the container at $r = 0$ and at $r = 1/2R_O$. Representative results are shown in Figs. 5-5 and 5-6 respectively. These measurements show that the direction of flow is maintained throughout the container and that the axial velocity component is negligible in comparison with the azimuthal velocity even for the small aspect ratio of the container ($l/d = 1.2$).

The observation of uniform flow throughout the bulk and negligible axial velocity is indicative that though the magnetic field generated in the stator varies by as much as 21% along the

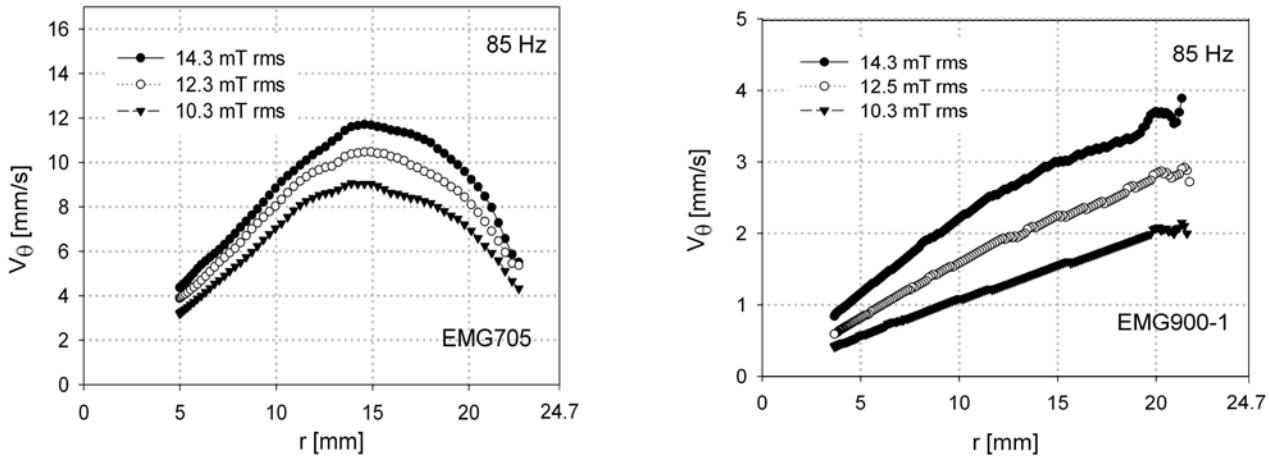

a) b)

Figure 5-3: Velocity profile measurements as a function of the magnitude of the applied magnetic field for a) EMG705 and b) EMG900-1

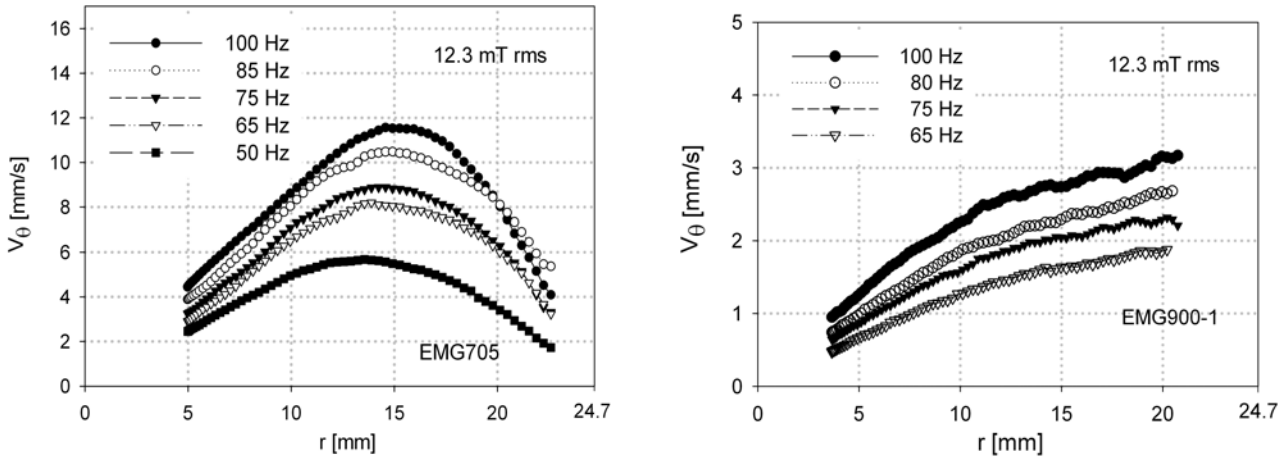

a) b)

Figure 5-4: Velocity profile measurements as a function of the frequency of the applied magnetic field for a) EMG705 and b) EMG900-1

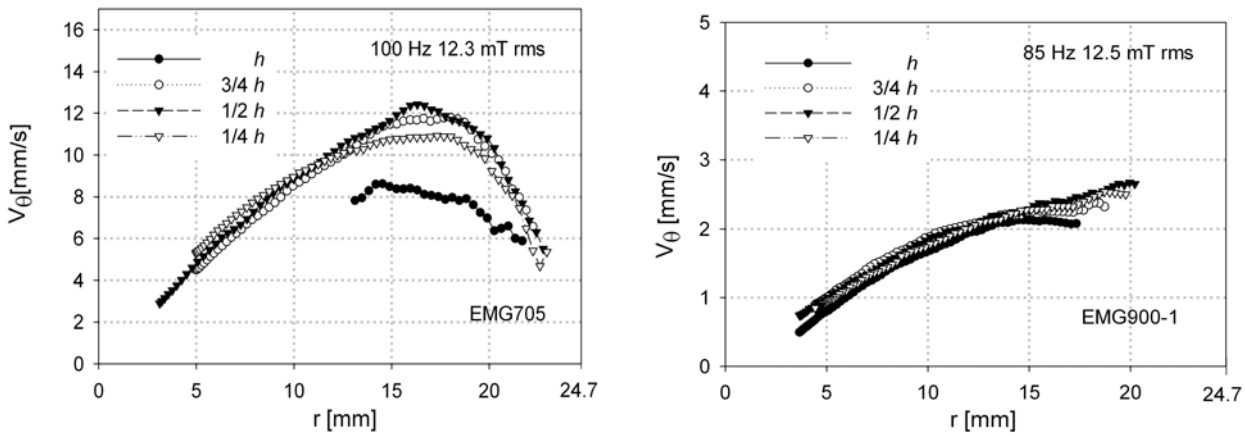

a) b)

Figure 5-5: Velocity profiles for EMG705 ferrofluid using probes placed at four different heights of the container axis with cover.

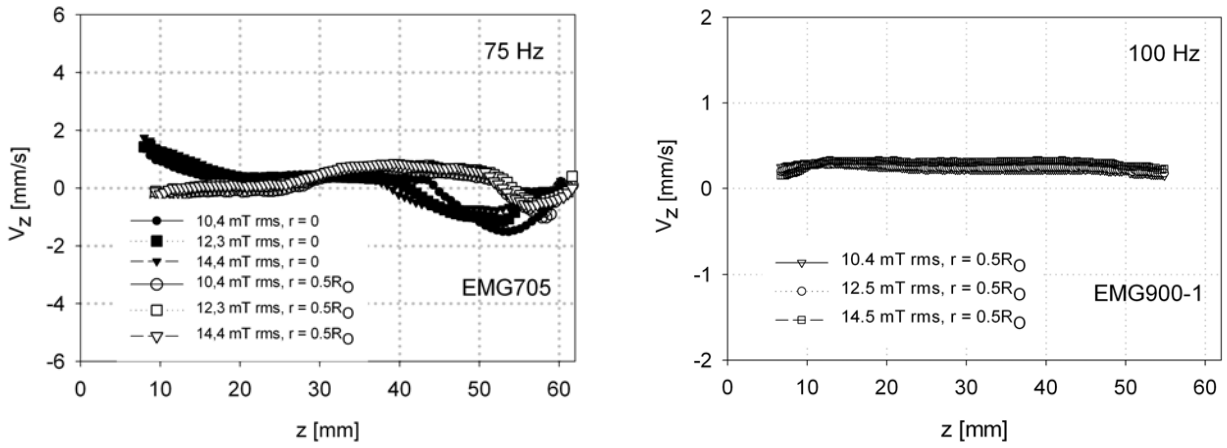

a) b)

Figure 5-6: Axial velocity component measured for a) EMG705 and b) EMG900-1 ferrofluids using a probe placed on the fixed top cover (z-measured downward from the top).

vertical axis (4% throughout most the fluid), this variation does not induce appreciable flow in the axial direction. Furthermore, as noted before, the location of the velocity maximum is different for the two fluids, which is contrary to what would be expected if the flow were driven by a field inhomogeneity which is concentrated close to the container wall (*i.e.*, close to the slots). Hence it is unlikely that our observations are the result of field in-homogeneity.

Temperature measurements were made for field amplitudes of 10.4, 12.5 and 14.5 mT rms for the frequencies of 50, 65, 75, 85, 100, and 125 Hz during a time interval of 56 min. Three temperature sensors were placed in the mid height of the cylinder at $r = 0$, $r = 0.5Ro$ and $r = Ro$. We found a temperature increase of 4 °C over the duration of the experiment, and a maximum radial temperature variation of 0.2 °C. Clearly, radial temperature gradients are negligible, hence the mechanism explained by Pshenichnikov *et. al.* [31] is not at work in our experiments. Furthermore, if dissipative effects were responsible for the observed flow, one would expect a time delay between turning on the magnetic field and start of the flow. To verify this we made measurements of the flow startup by taking velocity profiles at intervals of 2 s for a period of 100 s. The results are presented in Fig. 5-7 where only a few profiles are shown for better illustration. The poor quality of the velocity profiles of Fig. 5-7 is because these are instantaneous velocity measurements, whereas the others flow measurements reported herein correspond to steady flow for which the average of over 70 profiles are reported. The transient experiment was carried out at three different frequencies. The measurements demonstrate that steady state flow is obtained after approximately 30 s, with an immediate response to the startup of magnetic field rotation.

A third series of experiments was carried out under the same conditions but using an open container. In these experiments, the top probe was placed 4 mm below the free surface, as measured from the probe center. The velocity profiles in Fig. 5-8 show a transition from co-rotation of field and fluid in the bulk to counter-rotation close to the free surface. These observations are in agreement with the measurements of Rosensweig *et al.* [17] but they demonstrate that the bulk flow is not negligible in comparison to the surface flow. Both the surface driven flow and the body-couple induced flow coexist under our experimental conditions. These experiments further show that surface velocity profile measurements are inappropriate in assessing theoretical analyses of the bulk flow as these do not represent the flow behavior in the bulk of

the fluid.

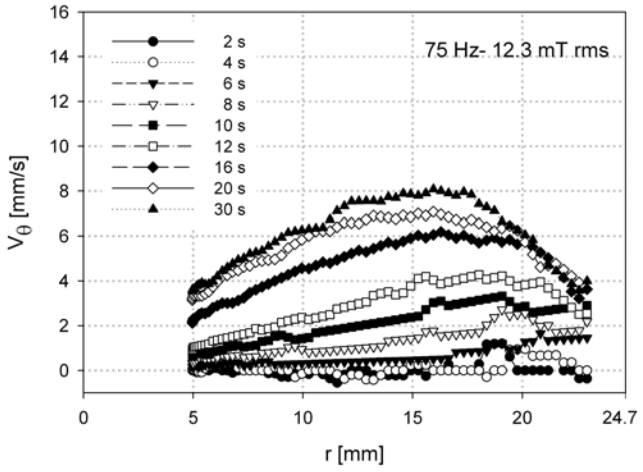

Figure 5-7: Startup of spin up flow. These velocity profiles were taken at 2 s intervals for 100 s. The firts profile corresponds to the instant the magnetic field was switched on.

5.2 Torque measurements

The experimental setup used to generate the magnetic field and obtain the torque measurements was described in Chapter 4. The torque required to restrain the spindle from rotating was measured for field frequencies from 25 Hz to 500 Hz rotating in clockwise direction and field amplitudes from 0 to 17.0 mT rms, for the two different volumes of fluid. This series of measurements was made for both ferrofluids and their dilutions. Fig. 5-9 presents typical measurements of torque as a function of applied magnetic field amplitude and frequency for the EMG705 ferrofluid using a spindle with 12 ml of ferrofluid.

5.3 Comparison between theoretical predictions and experimental measurements

Glazov [21] analyzed the phenomenon of spin-up flow using a set of equations similar to Eqns. (2.3) to (2.14), but setting $\eta' = 0$. The result was that no flow is expected when ferrofluid in a

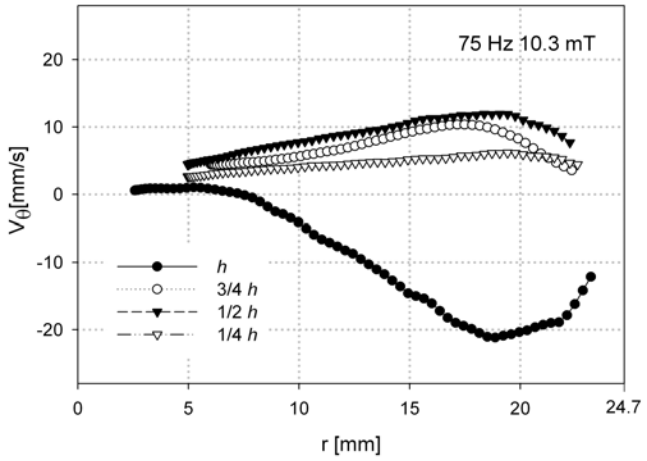

Figure 5-8: Velocity profiles for EMG705 at different heights in a container without a cover. In this $h = 63\,\text{mm}$ is the height of the container.The negative velocities indicate counter-rotation of fluid and field.

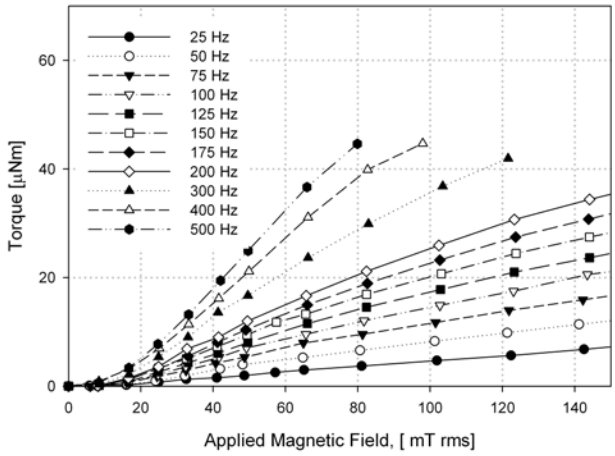

Figure 5-9: Torque measurements for 12 ml of EMG705 in hollow spindle as a function of frequency and amplitude of the magnetic field.

cylindrical container is subjected to a uniform rotating magnetic field. Glazov then attributed the experimental observations of Moskowitz and Rosensweig [8] to field inhomogeneity. To demonstrate this, Glazov obtained a general solution for flow using higher spatial harmonics, $m \neq 1$ in Eqn. (2.2), to simulate the rotating magnetic field generated in a multi-pole magnetic induction machine stator for two asymptotic cases: $\alpha \ll 1$ and $\alpha \gg 1$. Only a qualitative comparison of the predictions for the case of $\alpha \ll 1$ can be made with our experimental measurements, as our experiments were made at moderate amplitudes of the magnetic field ($0.4 \lesssim \alpha \lesssim 1.25$). The velocity profiles predicted by Glazov's theory are of similar shape to the measured velocity profiles for EMG705, however Glazov's theory cannot describe the boundary layer character of the velocity profiles for EMG900. In addition, Glazov predicts that the flow direction reverses, becoming contrary to the field direction, when $\phi_h > 0.12$, being ϕ_h the hydrodynamic volume fraction of particles. Velocity profiles measured using EMG900-2 with $\phi_h = 0.16$, showed that the fluid co-rotates with the magnetic field even for this hydrodynamic volume fraction of magnetic particles[1].

From our measurements it is clear that the bulk fluid co-rotates with the magnetic field, therefore the results of Kaloni [29] for a slip boundary condition in the translational velocity do not agree with the experiments. Furthermore, the experimental results described above show that thermal effects are not responsible for the observed flow hence the theories presented by Shliomis [44] and Pshenichnikov *et al.* [31] do not explain the observed flow. Finally, as can be seen in Fig. 5-8 even though surface effects dominate at the free surface, as observed by Rosensweig *et al.* [17], the bulk flow is not negligible in comparison. These observations leave us presently with the original spin diffusion theory of Zaitsev and Shliomis [19] as the only published model in (at least qualitative) agreement with our measurements.

In order to compare our theoretical extension of the spin diffusion theory with our experimental flow measurements, the translational and spin velocity of our asymptotic analysis for zeroth, first, and composite solution are shown in Fig. 2-4. As was discussed in Chapter 2, the analysis for zeroth order predicts a rigid-body-like azimuthal velocity profile co-rotating with the field through most of the fluid and decreasing to zero near the container wall. Thus, our

[1] This value was determined using the relation $\phi_h = \phi\left(\frac{d_p+2\delta}{d_p}\right)$, where δ is the thickness of the surfactant layer which is generally assumed 2 nm and ϕ is the magnetic volume fraction reported in the Table 4.1.

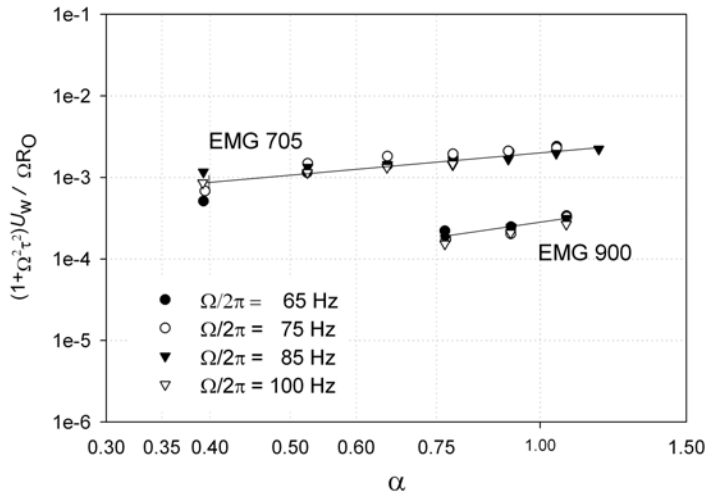

Figure 5-10: Log-log plot of the experimental extrapoled wall velocity vs Langevin parameter for EMG705 and EMG900-1

composite solution for flow predicts co-rotation with field in agreement with the experimental bulk velocity profiles.

The analysis predicts a square power dependence of flow on amplitude and linear dependence on dimensionless frequency of the applied magnetic field for zeroth order. Log-log plots of the dimensionless extrapolated wall velocity $\left(1+\tilde{\Omega}_f^2\right) U_{w,o}/\left(\Omega_f R_O\right)$ versus the applied magnetic field amplitude (made dimensionless using the Langevin parameter) were obtained (Fig. 5-10) for EMG705 and EMG900 ferrofluids in order to determine the dependence of the measured flow on magnetic field amplitude. Using a power law analysis we determined a power of one dependence on magnetic field amplitude for the EMG705 ferrofluid and a power of 1.6 dependence for the EMG900 ferrofluid. This difference between theoretical and experimental dependence on amplitude of applied magnetic field can be due to moderate saturation of the ferrofluid at the magnetic fields used in the experiments.

Log-log plots were similarly used to determine the dependence of the experimental torque measurements on the amplitude of the applied magnetic field. The experimental torque data

$L_{\exp}$was normalized using the zeroth-order torque expression $\left(L_{\exp}/\tilde{L}_{th}\right)$

$$L_{th} = -\mu_0 K^2 V_f \frac{\chi_i \tilde{\Omega}}{1+\tilde{\Omega}^2} + \mathcal{O}(\varepsilon) \tag{5.1}$$

and plotted (Fig. 5-11) versus the amplitude of the magnetic field, made dimensionless using the Langevin parameter, for both ferrofluids and their dilutions. We use the zeroth-order torque expression because the principal contribution to torque is due to antisymmetric stresses as was discussed in relation to Eqn. (2.97). These plots show that data for the two fluid volumes and different volumetric particle fractions are well described by the theoretical expression for torque, indicating that Eqn. (2.96) predicts the correct magnitude for the theoretical torque, specially for the EMG900 ferrofluid. From a power analysis we determined that the dependence of torque on applied magnetic field with 95% confidence interval is $1.11 \leq 1.16 \leq 1.21$ for the water based ferrofluid whereas for the kerosene based ferrofluid it is between $1.59 \leq 1.75 \leq 1.92$, in contrast with the theoretical predictions.

As has been previously mentioned, definitive estimates or experimental measurements of the spin viscosity η'or the dimensionless parameter κ are not available. The first estimate obtained by [19] from dimensional analysis predicts that $\kappa \sim 10^6$ implying that spin diffusion effects are negligible. More recently, Feng *et al.* [80] neglected η' arguing that the functional form of the spin viscosity depends on the square of particle diameter

$$\eta' \sim \eta_o \, d_p^2 \, f\ (\phi_h)\,, \tag{5.2}$$

suggesting that this effect is negligible for ferrofluids ($d_p \sim 10\,\mathrm{nm}$). However, the bulk flow measurements presented in the previous sections, which are in agreement with the theoretical predictions obtained from the spin diffusion theory, indicate that this phenomenon is important in driving the flow. In order to obtain an estimate for κ from our flow experiments for the EMG900 ferrofluid (as this shows the better agreement between theoretical predictions and experimental measurements), we used the concept of the extrapolated wall velocity $\tilde{U}_{w,o}$, given

by the dimensionless zeroth order vorticity [22] evaluated at $\tilde{r} = 0$

$$\tilde{U}_{w,o} = \frac{1}{2}\tilde{\Omega}_{z,0} = \frac{\zeta}{4\eta^* \left(1 + \tilde{\Omega}_f^2\right)} \left\{1 - \frac{1 + I_2(\kappa)}{I_0(\kappa)}\right\}. \tag{5.3}$$

Introducing the translational velocity scale, the definition of χ_i, and the definition of the Langevin parameter α in Eqn. (5.3) we obtain

$$\frac{\left(1 + \Omega_f^2 \tau^2\right)}{\Omega_f R_o} U_{w,o} = \frac{\phi \tau k_B T}{12 V_c \eta^*} \left\{1 - \frac{1 + I_2(\kappa)}{I_0(\kappa)}\right\} \alpha^2. \tag{5.4}$$

Thus from the slope of a plot of $\left(1 + \Omega_f^2 \tau^2\right) U_{w,o} / \left(\Omega_f R_O\right)$ versus α^2 and using Eqn. (5.4) we obtained a value of $\kappa = 33.7$ for the EMG900 ferrofluid. This value yields an estimated spin viscosity of $\eta' = 5.8 \times 10^{-10}\,\mathrm{kg\,m\,s^{-1}}$ which is nine orders of magnitude higher than expected by dimensional analysis. Note however, that expression (5.2) is a dilute-limit result applicable for suspensions of hard spheres in a newtonian fluid and does not take in to account the fact that ferrofluids are typically stabilized by surfactants layers and hence have significant free surfactant concentrations in solution.

5.4 Conclusions

Since Moskowitz and Rosensweig [8] first observed spin up flow, only surface velocity profiles have been available to evaluate the various theories describing the phenomenon. However, as shown above, surface velocity profiles are not suitable to evaluate bulk theories as flow of the fluid near the air-fluid interface is dominated by surface effects and is therefore not representative of the bulk flow. It is no surprise that surface velocity profile measurements have resulted in confusion in testing the spin diffusion theory, as the theory could not explain the observed counter-rotation between flow and field directions [9, 17]. In stark contrast, our bulk flow measurements show that the flow co-rotates with the field in the bulk even when fluid near the air-fluid interface counter-rotates with the field as a consequence of surface effects. Critical comparison of our experimental observations and the models proposed by Glazov [21], Kaloni [29], and Pshenichnikov *et al.* [31] indicates that none of these models adequately explain the

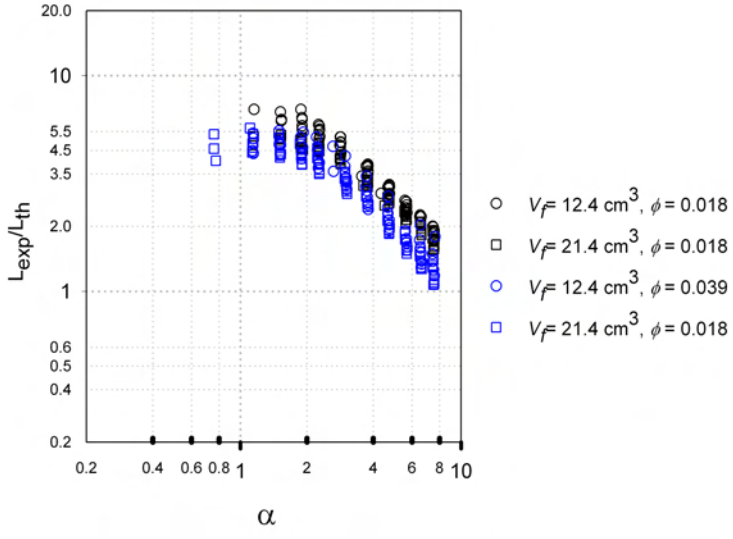

a)

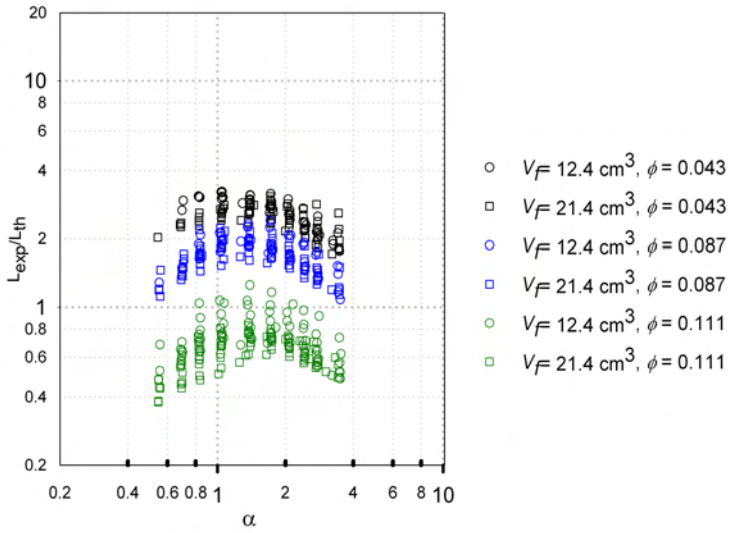

b)

Figure 5-11: Log-log plots of the experimental normalized torque vs frequency for a) EMG705 and b) EMG900 ferrofluids and all their dilutions.

observations. Furthermore, our experiments with a top free surface indicate that though surface stresses dominate at the air-ferrofluid interface, the bulk flow is not negligible in comparison.

Our azimuthal velocity profiles are in qualitative agreement with the spin diffusion theory of Zaitsev and Shliomis [19]. However, the dependence of flow measurements on amplitude of the magnetic field was found to be 1.16 and 1.75 power for water and kerosene based ferrofluids respectively, in contrast to the power of two dependence predicted by our first order asymptotic solution. Experimental torque data showed that the dependence on amplitude of magnetic field agrees with theoretical predictions. Direct quantitative comparison between theoretical results and experimental measurements is not possible as the perturbation parameter of our asymptotic analysis is $\varepsilon \sim 1$ for the range of amplitude of the applied magnetic field used in the experimental measurements. Still, we estimate from comparing the experimental measurements and predictions of the extrapolated wall velocity of the asymptotic analysis a value of $\eta' = 5.8 \times 10^{-10}$ kg m s^{-1} for the spin viscosity of the kerosene-based ferrofluid.

We realize that this is a controversial value, since the majority of the current literature on the subject tacitly assumes this dynamical parameter to be negligible. The result underscores the need for a more thorough consideration of possible origins for a couple stress in ferrofluids or alternate constitutive equations capable of capturing the observed flow phenomena.

Chapter 6

Experimental results of ferrofluid between coaxial cylinders under rotating magnetic fields

In the assessment of theories on the annular flow of ferrofluid induced by a rotating magnetic field, experimental data such as torques and surface velocity profiles have been used [17, 18, 32] because of the inherent difficulty in obtaining experimental bulk velocity profiles by conventional methods. In addition, all current theories assume $\eta' = 0$ and consistently predict no flow when both cylinders are held fixed. This result disagrees with the theoretical predictions obtained in Chapter 3, where flow is predicted under these conditions using the spin diffusion theory.

We present the first experimental evidence of bulk flow of ferrofluid in an annular gap with both cylinders stationary using the ultrasound velocity profile method. A series of measurements similar to those used to characterize spin up flow in Chapter 5 and torque measurements for several values of Υ were carried out in order to obtain experimental data that allows comparison with theoretical predictions obtained from the spin diffusion theory in Chapter 3. We found good agreement between theoretical results and velocity profiles for kerosene based ferrofluid. In contrast, torque and flow measurements for water based ferrofluid show deviations from the expected behavior predicted by the spin diffusion theory.

6.1 Previous work

Flow measurements for ferrofluid in annular geometry have been limited to surface velocity profile and torque measurements. A limited set of velocity data were obtained by Rosensweig *et al.* [17] using aluminium particles as tracers on the surface of a ferrofluid filling the annular gap between two coaxial cylinders. These experimental measurements were used to compare to a theoretical solution obtained from the spin diffusion theory. However, this analysis did not consider the non-uniformity of the magnetic field in the annular region originating from the presence of the inner cylinder. Their experimental measurements showed flow changing direction within the annulus, similarly to our theoretical predictions. However, the flow direction in the annular gap is essentially counter rotating with field direction, changing to co-rotation near the external cylinder, opposite to our predictions. Using the same procedure, Kikura *et al.* [18] obtained surface velocity profiles for water based ferrofluid in a cylindrical container and annular geometry. Nevertheless, they used a four-pole stator machine to generate the rotating magnetic field. Clearly, this case does not represent the theoretical situation analyzed in Chapter 3, where we simulated the field generated by a two-pole stator machine. In conclusion, limited experimental data is available in the literature that allows a conclusive evaluation of these theories.

6.2 Velocity profile measurements for ferrofluid in annular gap

A series of flow measurements similar to those carried out for spin up flow in Chapter 5, were carried out for flow of ferrofluid in the annular geometry. Velocity profiles were measured for the ferrofluid filling the annular space between coaxial cylinders for values of $\Upsilon = 0.38$ ($R_O = 24.7\,\text{mm}$ and $R_I = 9.35\,\text{mm}$ with wall to wall distance of $15.35\,\text{mm}$) and $\Upsilon = 0.2$ ($R_O = 24.7\,\text{mm}$ and $R_I = 5\,\text{mm}$ with wall to wall distance of $19.7\,\text{mm}$).

Our apparatus design, illustrated in Fig. 6-1, uses the same polycarbonate container used in experiments of spin up flow allowing us to obtain simultaneous measurements of velocity profiles relative to ultrasonic beams propagating at three distinct angles (using three ultrasonic transducers) relative to the diagonal. New covers were built that allow centering the inner cylinder inside the container. All velocity profile measurements in this Chapter were made

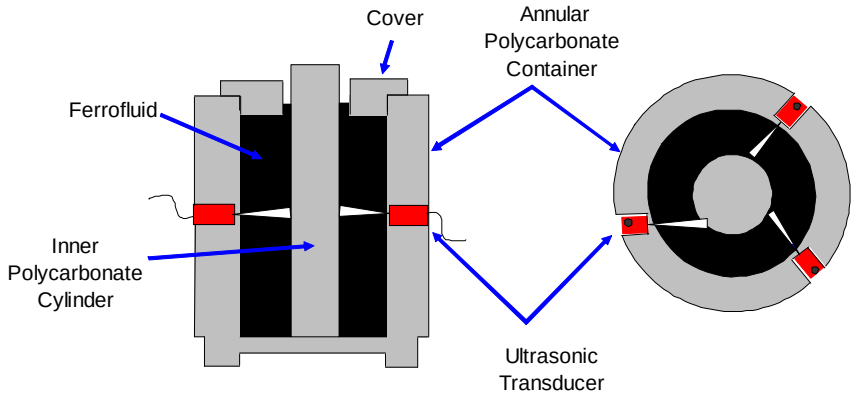

Figure 6-1: Illustration of the experimental setup for measuring torques and velocity profiles of ferrofluids filling an annular space and subjected to a rotating magnetic field. Left: Annular container with ultrasonic transducers located inside a two-pole induction motor stator. Right: Top view showing transducers at different incident angles. The transducers are separated from the ferrofluid by a thin polycarbonate wall.

using a cover.

Experiments were carried out for field frequencies between 20 and 120 Hz and amplitudes between 8.3 mT rms and 14.3 mT rms for EMG705 whereas for the EMG900-1 ferrofluid measurements were taken to frequencies between 85 and 150 Hz and amplitudes between 12.4 mT rms and 16.3 mT rms. This in order to obtain better quality measurements for the EMG900-1 ferrofluid as its flow magnitude is lower that of the EMG705 ferrofluid for the same frequency and amplitude of the magnetic field.

In order to avoid thermal effects influencing the flow measurements, radial temperature gradients were measured during the experiments finding variations of less than 0.2 °C. In order to do this, one thermometer was placed in the middle of annular space, and two thermometers were placed adjacent to the inner and outer cylinder walls. Measurements were taken for time intervals equal to that required to obtain a velocity profile in the range of frequencies and amplitudes studied of the applied magnetic field.

The values of the angles of the ultrasound beam used to obtain the azimuthal velocity component from parallel velocity component reported by DOP2000, were determined from Table 4.4. A counterclockwise rotating field was applied such that a positive velocity measurement implied co-rotation of field and fluid. Figure 6-2 compares the velocity profiles for EMG705

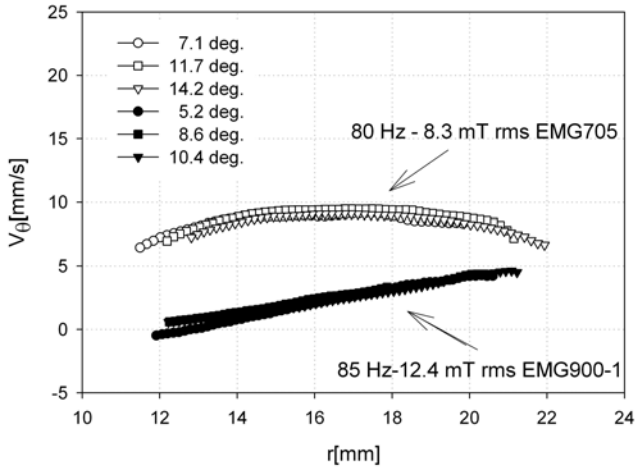

Figure 6-2: Velocity profiles for ferrofluid filling the annular gap between stationary coaxial cylinders, obtained with three transducers at different angles with respect to the diagonal for EMG705 and EMG900-1. The external radius is 24.64 mm, and the internal radius is 9.4 mm.

to frequency of 80 Hz and 8.3 mT rms of magnetic field amplitude with velocity profiles for EMG900-1 to 85 Hz and 12.4 mT rms. Clearly, bulk flow is observed with both cylinders stationary, contrary to the predictions of [15, 27, 64]. However, there is a noticeable difference between the shape of the velocity profiles for both fluids. As can be observed in Fig. 6-2, the annular bulk flow is unidirectional co-rotating with the field in the annular space that can be measured by DOP2000 machine for the EMG705, being unlikely that the flow direction changes near the wall of the inner cylinder. A different situation is observed for the velocity profiles for EMG900-1 which show a possible change of direction near the wall of the inner cylinder. A comparison between the experimental velocity profiles of Fig. 6-2 with theoretical velocity profiles of Fig. 3-3 show that the better qualitative agreement is obtained for velocity profiles of the EMG900-1.

Observing the complete set of experimental velocity profiles in Appendix C, it can be seen that velocity profiles taken with different probe angles do not overlap exactly for EMG900-1, however the assumption of azimuthal flow can be taken as valid as this variation is negligible. Figure 6-2 also illustrates that the velocity is fairly uniform in magnitude in the gap for the EMG705 whereas velocity profiles for EMG900-1 are in agreement with the predictions of

the spin diffusion theory. These observations are indicative of the fact that azimuthal field inhomegeneities due to the use of an imperfect two-pole stator winding are not responsible for the observed flow. If they were, one would expect the fluid to be accelerated close to the outer cylinder (where the effects of azimuthal inhomogeneities in the winding would be relevant) and monotonically decelerate to zero velocity at the inner cylinder. The velocity profiles show that this is clearly not the case.

Another series of experiments studied the variation of velocity profile with axial position by using probes at h, $\frac{3}{4}h$, $\frac{1}{2}h$ and $\frac{1}{4}h$ ($h \approx 63.5$ mm being the container height) for the EMG705 ferrofluid. Simultaneously, the axial velocity profiles were measured using a probe placed in the middle of the annular space. Figure 6-3 shows that the velocities measured at the middle of the container are slightly higher than those measured at $\frac{1}{4}h$, $\frac{3}{4}h$, and h. This slight variation is not due to misalignment of the inner spindle axis with the outer container and stator axis as we have used three probes placed at 120 ° from each other to verify that the flow does not have an azimuthal variation as would be expected with an eccentric inner cylinder. We therefore attribute the slightly higher velocity in the middle to the effect of viscous drag exerted by the top and bottom surfaces of the container. Figure 6-4 shows that the axial velocity is negligibly small compared to the azimuthal velocity. The observation of negligible axial velocity is indicative that though the magnetic field generated in the stator varies by as much as 21% along the vertical axis (4% throughout most the fluid), this variation does not induce appreciable flow in the axial direction.

Figure 6-5 shows the effect of frequency on velocity profiles measured at a magnetic field amplitude of 12.5 mT for EMG705 and EMG900-1 ferrofluids. One can observe in Fig. 6-5, that the dependence of both fluids on frequency is not the same, being almost negligible for the EMG900-1 ferrofluid. The effect of magnetic field amplitude and inner cylinder radius on velocity profiles for EMG705 and EMG900-1 are shown in Fig. 6-6. As can be noted from Fig. 6-6a, under similar conditions of amplitude and frequency of the applied magnetic field, the ferrofluid contained in the narrower annular gap was observed to rotate at a faster rate for EMG705 ferrofluid whereas, the faster rotation rate for the EMG900-1 is observed for the flow obtained in the wide annular gap as illustrated Fig. 6-6b. The first is counterintuitive, as one would expect the flow to be retarded as the surface-to-volume ratio in the gap increases. Similar

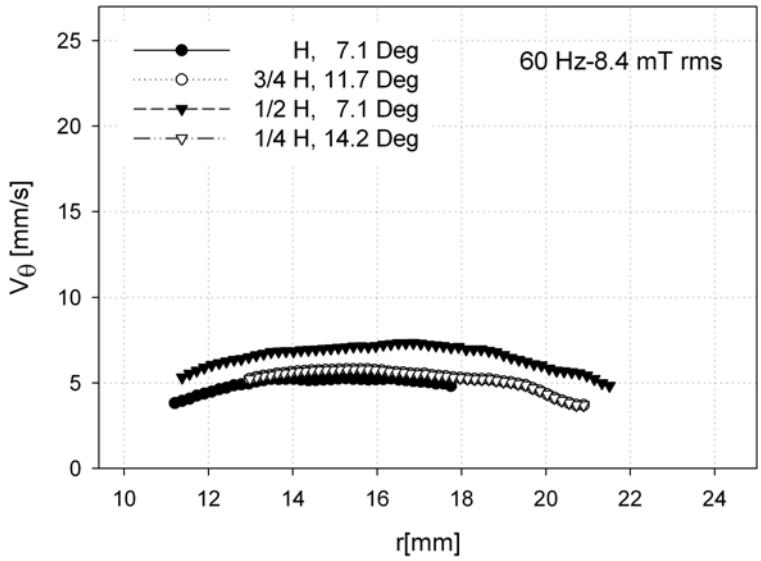

Figure 6-3: Velocity profile in the azimuthal direction using fixed transducers placed at four different heights ($h = 63.5\,\text{mm}$) of the container for 60 Hz frequency and 8.3 mT rms amplitude of the applied magnetic field

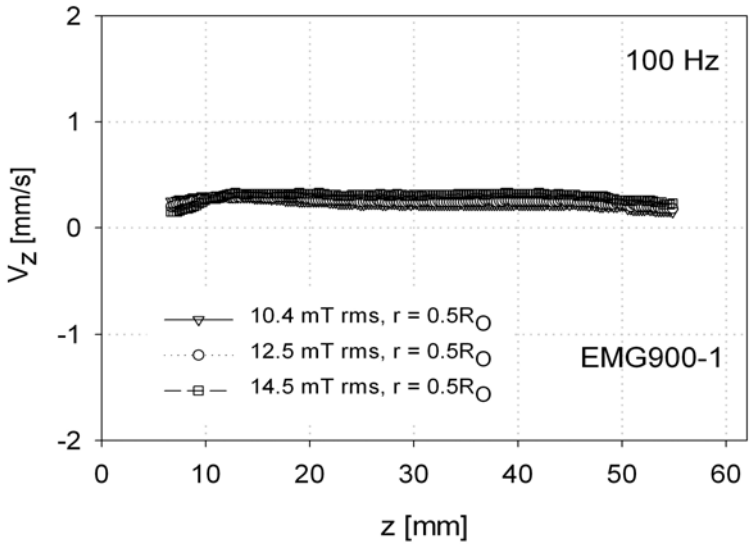

Figure 6-4: Axial velocity profile obtained using transducers placed in the cover of the container in the middle of the annular gap ($r = 17.2\,\text{mm}$) .The external radius is 24.64 mm and the internal radius is 9.4 mm

observations were made for the free surface driven flow in cylindrical container by Rosensweig *et al.* [17], result that it is in agree with the predictions of the analysis carried out in Chapter 2. Nevertheless, observations of Fig. 6-6a are contrary to the predictions of spin diffusion theory for annular flow as is determined by comparison with Fig. 3-5. The observations of Rosensweig for surface flow in a cylindrical container can be explained by considering that the surface flow is induced by a narrow region close to the container wall, corresponding to the meniscus region, in which the interfacial balance of asymmetric stresses induces fluid motion. However in our experiments for annular flow no such free surface exists.

6.3 Torque measurements for ferrofluid in annular gap

In order to obtain the experimental torque data, we use the experimental setup described in Chapter 4 to generate the rotating magnetic field. The relevant dimensions of the apparatus are the inner (spindle) and outer (container) radii, R_I and R_O respectively, and the submerged spindle length l. Four values of the radial aspect ratio $\Upsilon = R_I/R_O$ were studied: $\Upsilon_1 = 0.32$ ($R_I = 9.36\,\text{mm}$ and $R_O = 29.62\,\text{mm}$), $\Upsilon_2 = 0.52$ ($R_I = 12.70\,\text{mm}$ and $R_O = 24.64\,\text{mm}$), $\Upsilon_3 = 0.64$ ($R_I = 19.05\,\text{mm}$ and $R_O = 29.62\,\text{mm}$), and $\Upsilon_4 = 0.77$ ($R_I = 19.05\,\text{mm}$ and $R_O = 24.64\,\text{mm}$). The submerged spindle length was $l \approx 58\,\text{mm}$ for all experiments. In order to obtain the experimental torque measurements, the polycarbonate container was centered in the gap of a two-pole, three-phase induction motor stator winding and subsequently the spindle was centered inside the container. In all experiments, the angular velocity of the inner spindle was set to zero and the direction of the rotating field was set counterclockwise in order to obtain positive torque measurements and thereby utilize the full instrument range.

The torque required to restrain the spindle from rotating was measured for field frequencies from 25 to 500 Hz and field amplitudes from 0 to 17.0 mT rms, for the four different values of the aspect ratio Υ. This series of measurements was made for the EMG705 and EMG900 ferrofluids and their dilutions. Figure 6-7, presents typical measurements of torque as a function of applied magnetic field amplitude and frequency for the EMG705 ferrofluid. The complete series of torque measurements is shown in Appendix B.

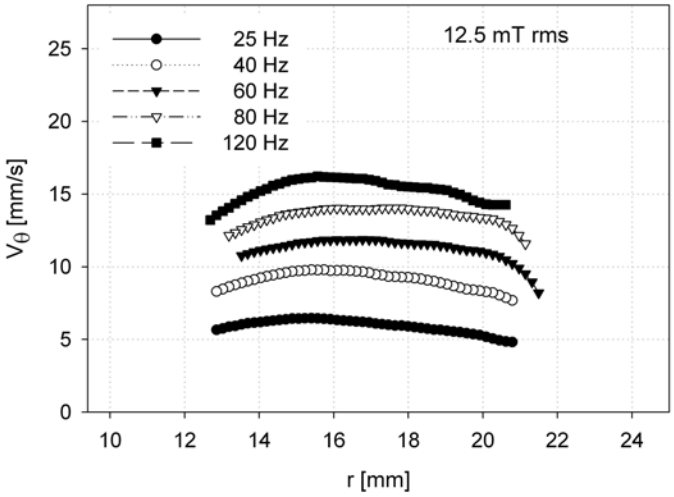

a)

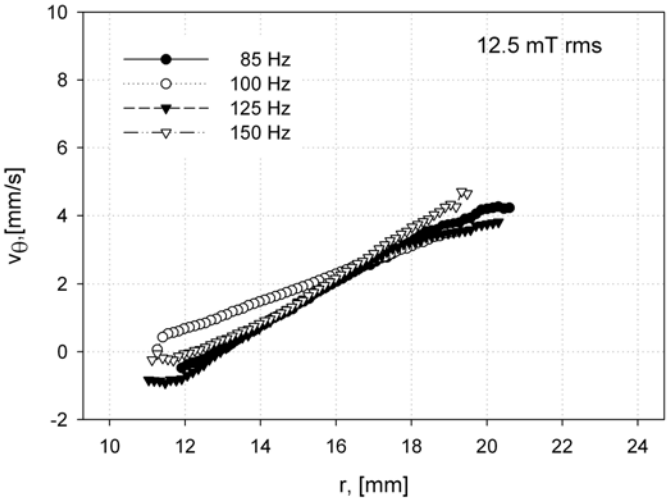

b)

Figure 6-5: Velocity profile dependence on magnetic field frequency with constant amplitude of 12.5mT rms for a) EMG705 and b) EMG900-1 ferrofluids

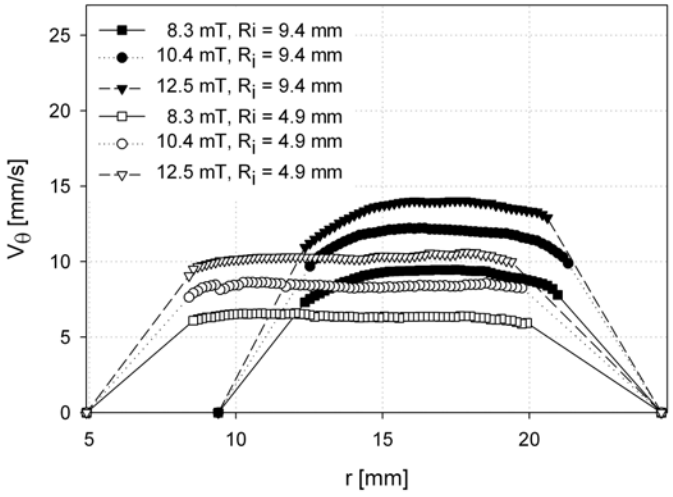

a)

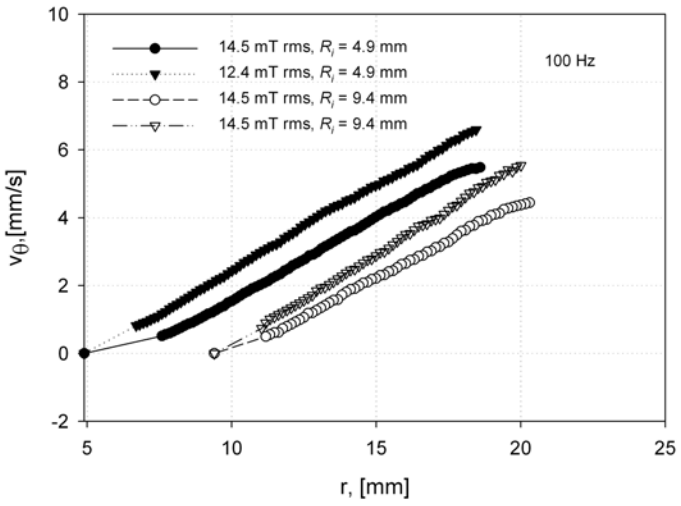

b)

Figure 6-6: Velocity profile dependence on magnetic field amplitude at a constant frequency of 80Hz for two distinct inner cylinder radii. Dashed lines added to aid in distinguishing between the two inner and outer radii. The external radius is 24.64 mm

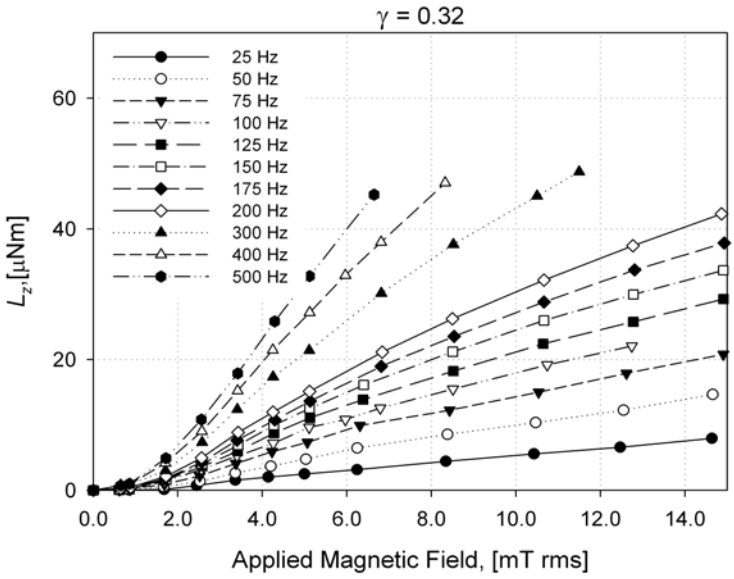

Figure 6-7: Torque required to restrain the spindle from rotating when sorrounded by ferrofluid filling the annular space between the spindle and outer container, as a function of magnetic-field amplitude and frequency, and for radial aspect ratio of $\Upsilon = 0.32$.

6.4 Scaling analysis of torque and flow measurements

6.4.1 Comparison of experimental torque data with torque expression with $\eta' = 0$

Since the angular velocity of the spindle was set to zero in our experiments, the torque measured by the viscometer should correspond to the result given by Eqn. (3.1) for the case of $\eta' = 0$. Applying this limit is reasonable since η' was estimated to be $\sim 10^{-10}$ in Chapter 5. This torque is due to the viscous shear stress on the spindle resulting from the magnetic-field induced flow of the ferrofluid around the spindle. Because the viscous stress tensor in ferrofluids is asymmetric in the presence of rotating fields, this shear stress has two contributions, illustrated in Fig. 6-8. As the particles rotate counterclockwise a clockwise torque is induced on the spindle, corresponding to the anti-symmetric component of the stress (Fig. 6-8a). As the fluid co-rotates with the field a counterclockwise torque is induced on the spindle, corresponding to the symmetric component of the stress (Fig. 6-8b).

In our experiments the anti-symmetric stresses dominate. This can be verified by estimating

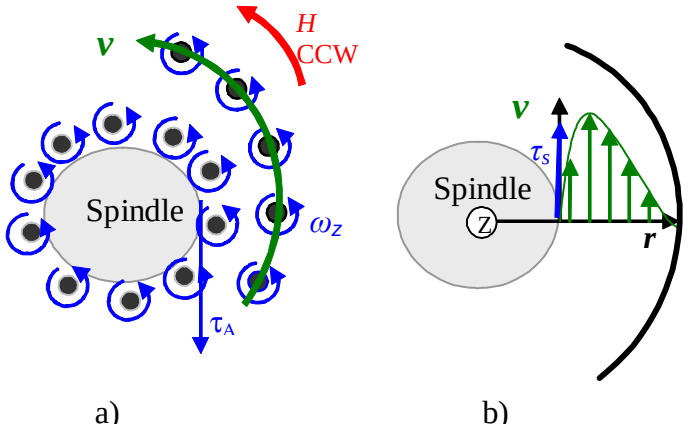

Figure 6-8: Phenomenological model of ferrofluid torque on cylindrical walls in a rotating magnetic field H. a) Axially directed torque induced by rotation of magnetic nanoparticles and b) torque produced by viscous shear stress at the spindle due to magnetic field induced flow.

the contribution of the symmetric stresses to the torque by assuming that the velocity goes from a measured value U to zero in a boundary layer of thickness δ_t close to the inner cylinder. The corresponding torque is, $2\pi R_I l \tau^s|_{R_I}$ where we assume a linear velocity profile to estimate the symmetric stress. As an example, for a measured velocity of 15 mm/ s and $R_I = 4.9\,\text{mm}$, corresponding to the conditions of Fig. 6-6a, assuming the velocity goes to zero linearly in a layer of thickness $\delta_t = 1\,\text{mm}$, the contribution of the symmetric stress is estimated to be 0.32 $\mu\text{N m}$ which is negligibly small in comparison to the measured torques ($\approx 20\,\mu\text{N m}$).

Figure 6-9 shows torque measurements L_{exp} normalized using the theoretical torque L_{th} according to Eqn. (3.1) as a function of the dimensionless field frequency $\tilde{\Omega}_f$, and as a function of magnetic field amplitude, made dimensionless using the Langevin parameter α.

Comparison of the results for the various aspect ratios and for two volumetric fractions shows that the dimensionless torque collapses the data set well. The dispersion seen at low fields corresponds to the lowest torques, which are most susceptible to measurement error. As can be seen in Fig. 6-9, the normalized data is close to order unity $(1 - 10)$, indicating that Eqn. (3.1) predicts the right order of magnitude for the torque. Because the only estimated parameter in using Eqn. (3.1) is the Brownian relaxation time, this is an indication that our

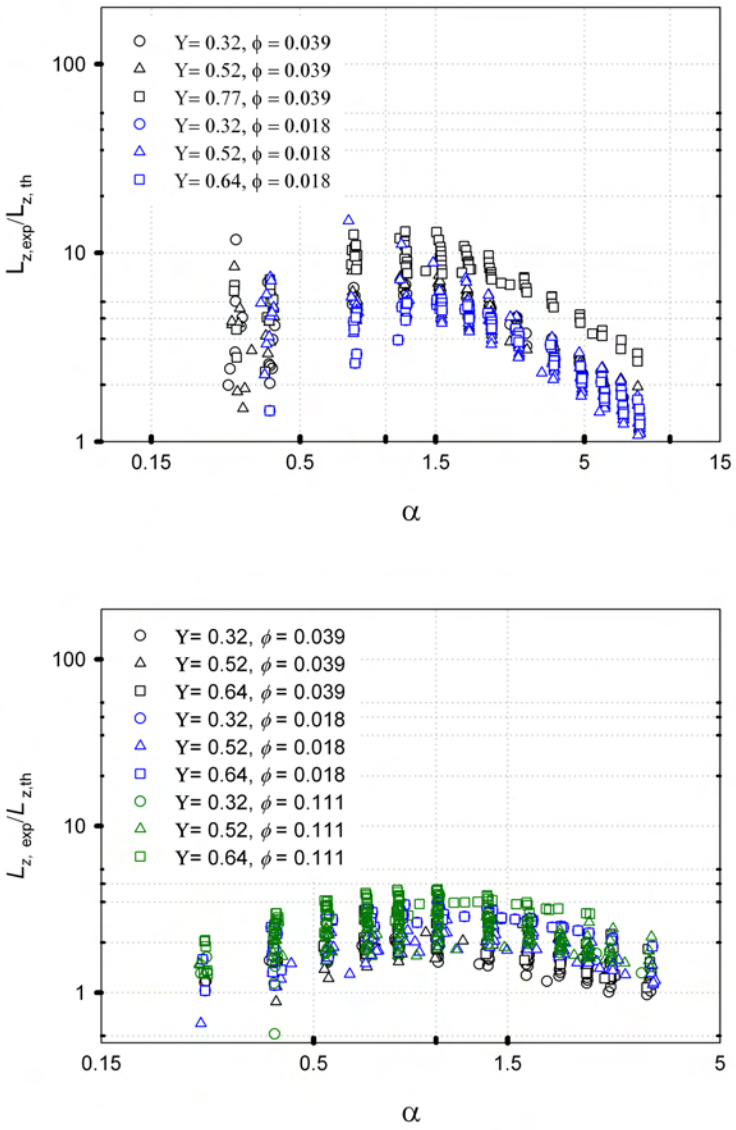

Figure 6-9: Log-log plot of the complete dimensionless torque data set normalized using Eqn. (3.1) versus dimensionless amplitude of the magnetic field for a) EMG705 and b) EMG900 and their dilutions.

Table 6.1: Torque dependence on the applied magnetic field for EMG700 and EMG900 ferrofluids and their dilutions reported with 95 percent confidence interval. Experimental data was normalized using Eqn. (3.1).

Ferrofluid	$\boldsymbol{\alpha}$	**Torque Dependence on Magnetic Field Amplitude**
EMG705	$\alpha > 1$	$1.09 \leq 1.14 \leq 1.18$
EMG900	$\alpha < 1$	$2.31 \leq 2.40 \leq 2.48$
EMG900	$\alpha > 1$	$1.84 \leq 1.87 \leq 1.90$

estimated values, shown in Table 4.2 are of the right order of magnitude. The dependence of the torque on both ferrofluids is reported in the Table 6.1 for the EMG705 and EMG900 ferrofluids. Dependence of torque data of the kerosene based ferrofluid presents different behavior for low ($\alpha < 1$) versus high ($\alpha > 1$) fields.

Equation (3.1) predicts a power-of-one dependence with field frequency, but a power-of-two dependence with field amplitude. However, Eqn. (3.1) is strictly applicable in the linear magnetization limit, for which the field is small and the Langevin parameter much smaller than unity. As can be seen in Fig. 6-9 our experiments were carried out at moderate field amplitudes, for which the Langevin parameter is of order unity, hence saturation effects will have begun to affect the field amplitude dependence of the torque. It is expected that as the fluid magnetically saturates the torque dependence with field amplitude should decrease to power unity.

6.4.2 Comparison of experimental torque data with torque expression with $\eta' \neq 0$

In this case, the torque expression given by Eqn. (3.101) includes viscous shear stresses and couple stress contributions. However, this torque expression is strictly applicable to values of $\varepsilon \ll 1$ and $\alpha \ll 1$ as the solution obtained of the ferrohydrodynamics problem in Chapter 3 only contains the zeroth order contribution. In spite of this, log-log plots of the $L_{\exp}/L_{th}$, versus the Langevin parameter α were obtained for the EMG705 and EMG900 ferrofluids and their dilutions in order to determine the dependence of the data on amplitude of the field and verify the agreement of the experimental torque data to the torque expression given by Eqn.

Table 6.2: Dependence of the torque on the applied magnetic field for EMG700 and EMG900 ferrofluids and their dilutions reported with 95 percent confidence interval. Experimental data was normalized using Eqn. (3.101).

Ferrofluid	$\boldsymbol{\alpha}$	**Torque Dependence on Magnetic Field Amplitude**
EMG705	$\alpha > 1$	$1.05 \leq 1.11 \leq 1.16$
EMG900	$\alpha < 1$	$1.97 \leq 2.17 \leq 2.37$
EMG900	$\alpha > 1$	$1.34 \leq 1.44 \leq 1.54$

(3.101), Fig.6-10. In calculating the L_{th}, we used the spin viscosity value $\kappa = 33$ obtained for the EMG900-1 ferrofluid in Chapter 5.

As can be seen in Fig. 6-10 the experimental data collapses well, specially for the kerosene based ferrofluid. Nonetheless the significance of this result is that ratify that the value of spin viscosity estimated is in the right order. Figure 6-10a shows that the experimental torque data for the EMG705 is one order of magnitude higher than theoretically expected using $\kappa = 33$. Using a power analysis in Fig 6-10, we determined the dependence of the water based ferrofluid and the kerosene based ferrofluid which are reported in Table 6.2 with 95% confidence interval. Thus, experimental measurements of torque for cylindrical and annular geometry obtained using water based ferrofluid are more consistent in displaying the greater divergence from the theoretical predictions than the experimental data obtained using kerosene based ferrofluid.

A similar scaling analysis was made for the velocity using the value at $r = 17.2$ mm for all profiles obtained using the EMG705-1 and EMG900 ferrofluids. The characteristic velocity $v_\theta \sim \Omega_f R_O$ was used to plot the scaled velocity $\tilde{v}_\theta = v_\theta / (\Omega_f R_O)$ as a function of the Langevin parameter in Fig. 6-11. The scaled velocity was found to have roughly power-of-one dependence on the applied field amplitude and frequency for EMG705 whereas that dependence for the EMG900 ferrofluid is in agreement with the power two dependence expected of the analysis. This is an interesting result in light of the fact that all available analyses, including the asymptotic analysis shown above, predict a negligible azimuthal velocity in the annular gap when both cylinders are held fixed.

Having already analyzed the experimental results for flow and torque for both geometries

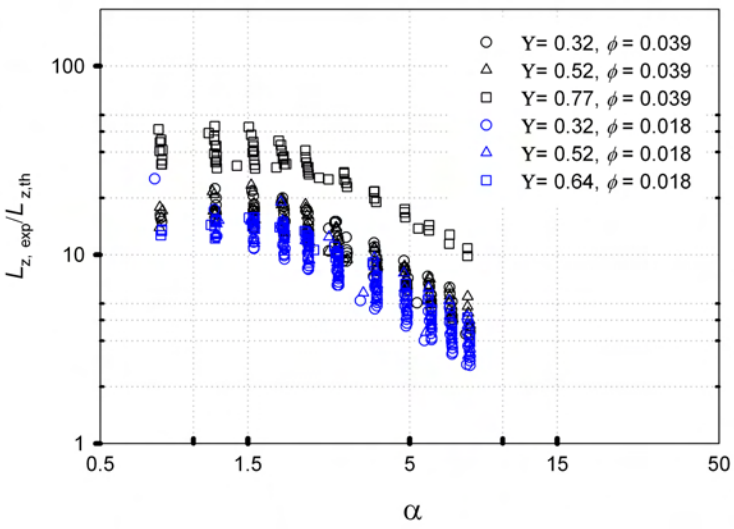

a)

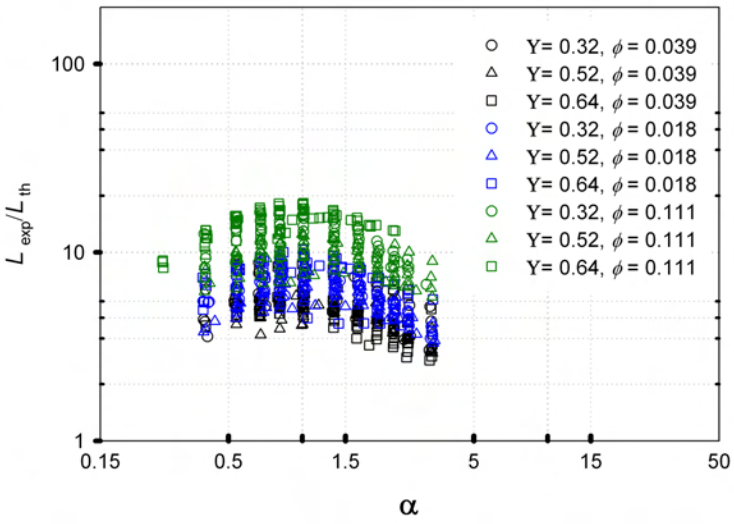

b)

Figure 6-10: Log-log plot of the complete dimensionless torque data set normalized using Eqn. (3.101) versus dimensionless amplitude of the magnetic field for a) EMG705 and b) EMG900 and their dilutions.

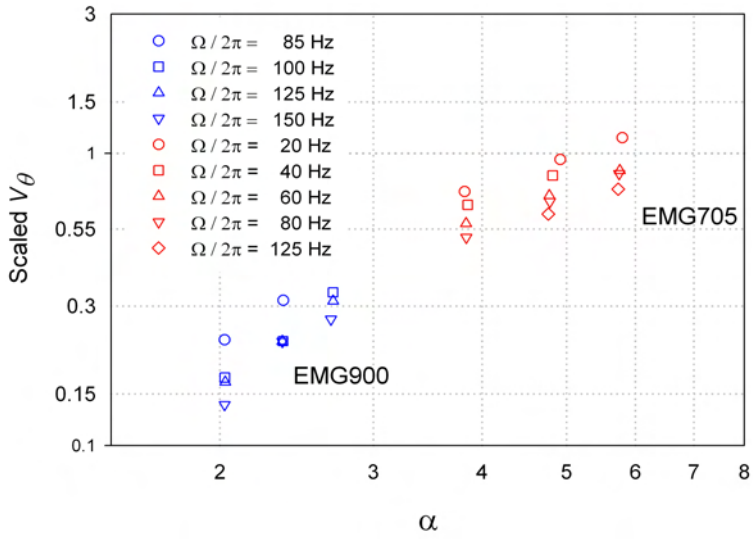

Figure 6-11: Log-log plot of the scaled azimuthal velocity at $r = 17.2\,\text{mm}$ for EMG705 and $r = 17.2\,\text{mm}$ for EMG900-1 ferrofluids, plotted versus Langevin parameter.

it is clear now that results obtained for the kerosene based ferrofluid were found in qualitative agreement with the predictions obtained from the spin diffusion theory. The Reynolds number R_e for annular flow using EMG705 and EMG900-1 were determined to be 210 and 28 respectively.

6.5 Conclusions

Torque and flow measurements demonstrate the existence of bulk flow of ferrofluid contained in an annular gap and subjected to a rotating magnetic field, for the case when both cylinders are held stationary. The experiments were carried out under conditions such that energy dissipation and radial temperature gradients are negligible. The observation of bulk azimuthal flow with negligible axial velocity is in stark disagreement with the analysis of Pshenichnikov and Lebedev [15] and with the asymptotic analysis presented by Chaves *et al.* [64]. Both analyses were done in the linear magnetization, zero spin viscosity limits, and predict zero bulk flow with both cylinders stationary. Arguably, the asymptotic analysis presented in Chaves *et al.* [64] could be

extended to second order in the perturbation parameter $\varepsilon = \tilde{\Omega}_f$ however the resulting velocity would be expected to have a power-of-four dependence with field amplitude. The measurements presented above clearly show that both the torque and azimuthal velocity have a power-of-one dependence with field frequency and amplitude. Similar observations were made in Chapter 5 (Chaves *et al.* [45]) for the situation of ferrofluid in a cylindrical container subjected to a uniform rotating magnetic field. In that case, the only explanation available in the literature which agreed with the experimental observations was the spin diffusion theory of Zaitsev and Shliomis [19]. It is likely that the mechanism that drives the flow in the annular gap experiments reported herein is the same as that which drives the flow in the experiments reported in Chapter 5 (Chaves et al. [45]). Unfortunately, the analysis of Zaitsev and Shliomis [19] hinges on the existence of couple stresses and the spin viscosity, which is commonly regarded to be negligibly small based on dimensional arguments of the hydrodynamic interactions occurring at the particle scale [80]. Further work is needed to elucidate if other mechanisms are responsible for the observed flow, such as spin-magnetization coupling in the magnetization relaxation (neglected in all analyses discussed above). Alternatively, other forms of the magnetization relaxation equation, valid far from equilibrium, could be tested.

Chapter 7

Concluding remarks

7.1 Thesis contributions

We present the first experimental evidence of the existence of bulk flow of ferrofluid in a cylindrical container induced by a uniform rotating magnetic field. This is contrary to the current literature consensus that predicts no bulk flow under these conditions. In 1990 Rosensweig *et al.* [17] carried out a comparison between several theories for the bulk flow of ferrofluid based on experimental evidence obtained in the free surface of the fluid. They found that the spin diffusion theory can explain several observations of the phenomenon; however, they claim that "*The spin diffusion theory suffers from a fatal flaw-we find that the direction of flow is the reverse in each instance from which is predicted*",concluding that the spin diffusion cannot be the cause of the observed flow. In contrast, we always observed the fluid co-rotating with the field in the bulk independent of the shape of the air-fluid interface. This observation demonstrates that spin diffusion predicts the correct flow direction and that volumetric effects and couple stresses are active in the phenomenon. The experimental evidence presented here demonstrates that volumetric and surface effects can coexist under the same conditions. This reveals that surface velocity profiles used in the literature for the testing of bulk flow theories are inadequate as they misrepresent the bulk flow. Comparison of flow and torque measurements with different theories present in the literature showing the better agreement with the extension of the spin diffusion theory of Zaitsev and Shliomis [19] obtained here. Nevertheless, the magnitude of flow is several orders of magnitude lower when the spin viscosity value obtained from dimensional

analysis is used.

Our flow measurements made in annular geometry are the first experimental evidence of bulk flow of ferrofluid in a cylindrical annular gap induced by a magnetic field rotating perpendicular to the cylinder axis. This observation is remarkable as none of the existent theories predict flow when both cylinders are fixed. An analytical solution for this problem was obtained for the zeroth order term of the regular perturbation expansion using spin diffusion theory. This analysis presumed linear dependence of the magnetization on the applied magnetic field ($\alpha \ll 1$). The results were found in good qualitative agreement with velocity profiles taken at moderate amplitudes of the applied magnetic field using the kerosene based ferrofluid. These results add weight to the spin diffusion theory as the mechanism responsible for the flow.

A review of the experimental results consistently show that measurements of torque and flow obtained using kerosene based ferrofluid are better described by the theoretical predictions than those obtained using the water based ferrofluid. This is more noticeable for the velocity profile obtained in annular geometry were the behavior between water and kerosene based ferrofluid are clearly different. This shows that experimental work used in assessment of theories must be made using oil based ferrofluid over water based ferrofluid.

7.2 Future work

Although recent studies has assumed the effect of couple stresses as negligible setting $\eta' = 0$, the experimental evidence presented here indicate that in the case of ferrofluids its effect is important. The significant difference between the estimated experimental value for η' and the obtained from dimensional analysis by Zaitsev and Shliomis show that effects such as inter-particle interactions or effects of substances used in the stabilization of the ferrofluids must be considered in order to obtain an estimate for η'. Nevertheless, due to the inherent difficulty in obtaining an analytical solution, numerical solution could be used. A practical and more reliable estimated that the reported herein for η' can be obtained using the expression for the torque on the wall of a cylindrical container Eqn. (2.96) adjusting torque data obtained with a more sensible torque meter that permit to take measurements to amplitudes of the magnetic field less than $\alpha < 0.8$ or in order to used the torque measurements obtained herein is necessary

to obtain a numerical solution for the torque that permit to include effects of saturation of the magnetization with the field.

An other rheological parameter used in the ferrohydrodynamic equations is the vortex viscosity which characterize the effect of antisymmetric stresses. The actual theoretical expression for ζ was obtained by Brenner and recently verified numerically by Feng assuming that couples stresses are negligible in the limit of diluted solutions. This confirms the necessity of more research that permit quantification of this rheological parameter.

In order to explain the difference in the behavior between the water and kerosene based ferrofluid a hydrodynamic (or may be ferrohydrodynamic) stability analysis must be carried out. The conditions predicted for stability or instability can be verified using the ultrasound velocity profile method.

Our flow measurements in open container show volumetric and surface effects present in the phenomenon; however, our measurements and analytical work were focused in the bulk flow. More effort must be directed to study and quantification of the effect of magnetic surface stresses on the macroscopic flow and torque measurements.

As we mentioned in Chapter 4, the polydispersity effect of the particle size on mechanism of relaxation must be taken in account in order to obtain better estimates of the relaxation times. Nevertheless, as can be seen in Table 4.3 for the EMG900 and their dilutions, the $\tilde{\tau}_N < \tilde{\tau}_B$ when the effect of particle polydispersity is taken in account. However of the comparison between experimental and theoretical results, agreement is obtained by the order of magnitude of $\tilde{\tau}_B$. This suggests, that alternatives to a parallel relaxation process must be studied as mechanism of relaxation.

Finally, practical applications of flow of ferrofluid induced by rotating magnetic fields in microfluidic or microdevices must be explored.

Appendix A

Stator winding specifications

The two pole motor stator winding used to generate the rotating magnetic field was obtained from a commercial pump motor of 1.5 hp of power, National Stock Number (NSN) k246. The specifications of the motor are

Pump duty motor	
Motor type	3 phase
Power	1 1/2 hp
Voltage	200-230/460
RPM	3450
Full load amps	4.8-4.2/2.1
Manufacturer	GE motors & industrial systems

This motor was disassembled and the stator winding was used as show Fig. A-1. Next, we connected the terminals of the stator in their low voltage configuration according to the instructions of the manufacturer.

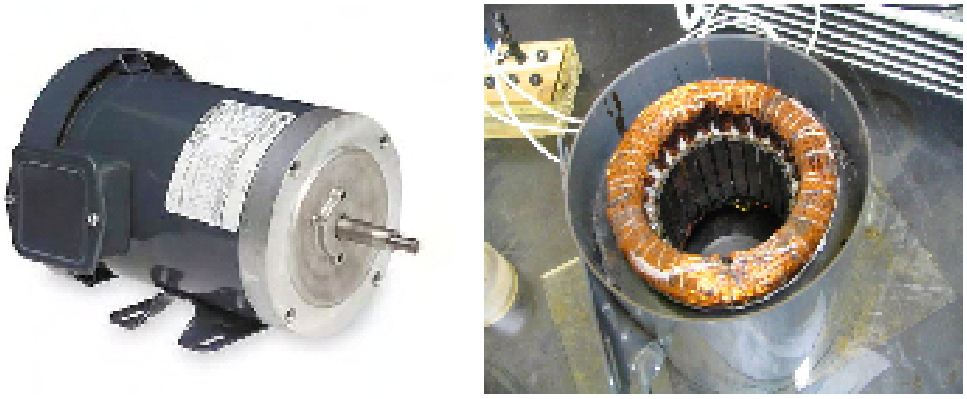

a) b)

Figure A-1: a) The electric motor as was obtained from the manufacturer. b) The stator winding as it is used in our setup for generate a rotating magnetic field.

Appendix B

Measurements of the slot angles in the polycarbonate container

The polycarbonate container used to obtain the experimental flow measurements was originally designed with four slots with angles of 10 ° and 15 ° with respect to the diagonal. However, when experimental azimuthal velocity profiles were obtained from the parallel velocity reported by the DOP 2000 using the relation

$$v_\theta = v_\parallel \frac{\sqrt{R_O^2 + x_p^2 - 2R_O x_p \cos\beta}}{R_O \sin\beta}, \tag{B.1}$$

we observed that velocity profiles taken on the same slot overlapped whereas velocity profiles on different slots did not. This can be due to inaccuracies in the value of the angle β. In order to obtain the correct value for the angle β, we took a print of the surface of the container on a paper. This allow us to reproduce in the better form the surface of the container in Autocad® in then to obtained the right value for each slot angles as is shown in Fig. B-1. Table B.1 summarize the value for each slot.

Using these new angle values velocity profile measurements taken with different slots overlapped for the case of glycerol in Couette geometry with exception of the angle measured for slot 1-2. This angle is more difficult to obtain due possibly to that is a small angle doing difficult the measure.

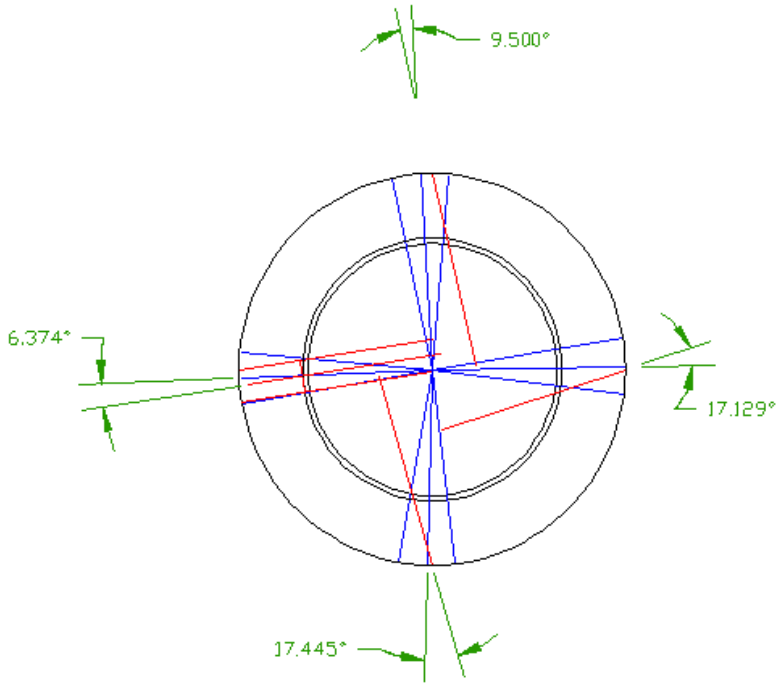

Figure B-1: Surface of the polycarbonate container reproduced in Autocad in order to measure the angle that make each slot with respect to the diagonal.

Table B.1: Expected and measured angles for slots of the polycarbonate container used in to obtain the experimental velocity profiles. First column are label used for each one of the slots in the container.

Slot	**Expected angle**	**Measured angle**
1-2	10 °	10.74 °
3-4	10 °	9.98 °
5-6	15 °	16.55 °
7-8	15 °	20.19 °

Appendix C

Velocity profile measurements for ferrofluid in a cylidrical container

C.1 Velocity profile measurements for EMG705 ferrofluid

C.2 Velocity profile measurements for EMG900-1

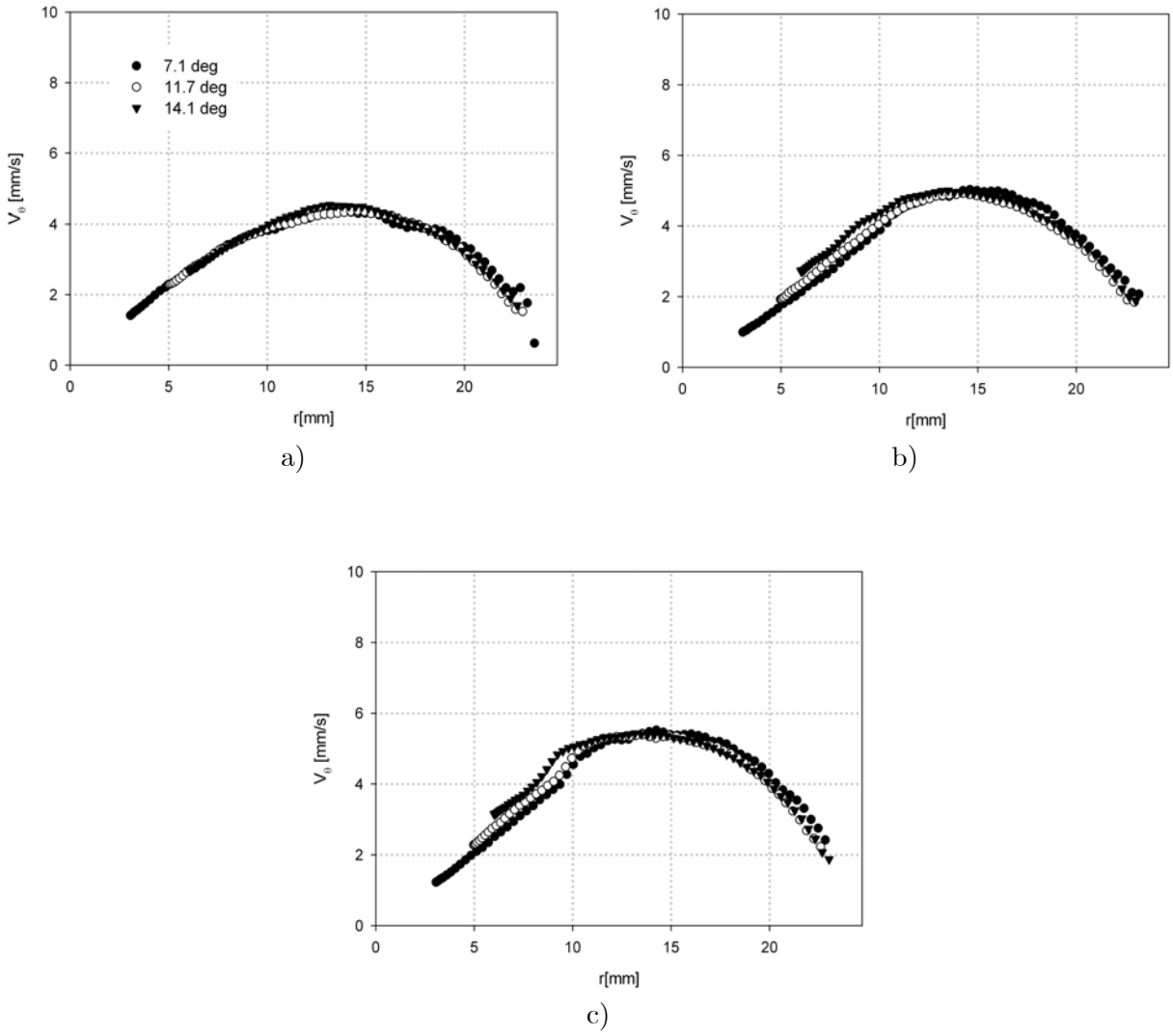

Figure C-1: Velocity profiles for EMG705 ferrofluid to frequency of 40Hz and a) 10.2mT rms b) 12.2mT rms and c) 14.4mT rms amplitude of the applied magnetic field.

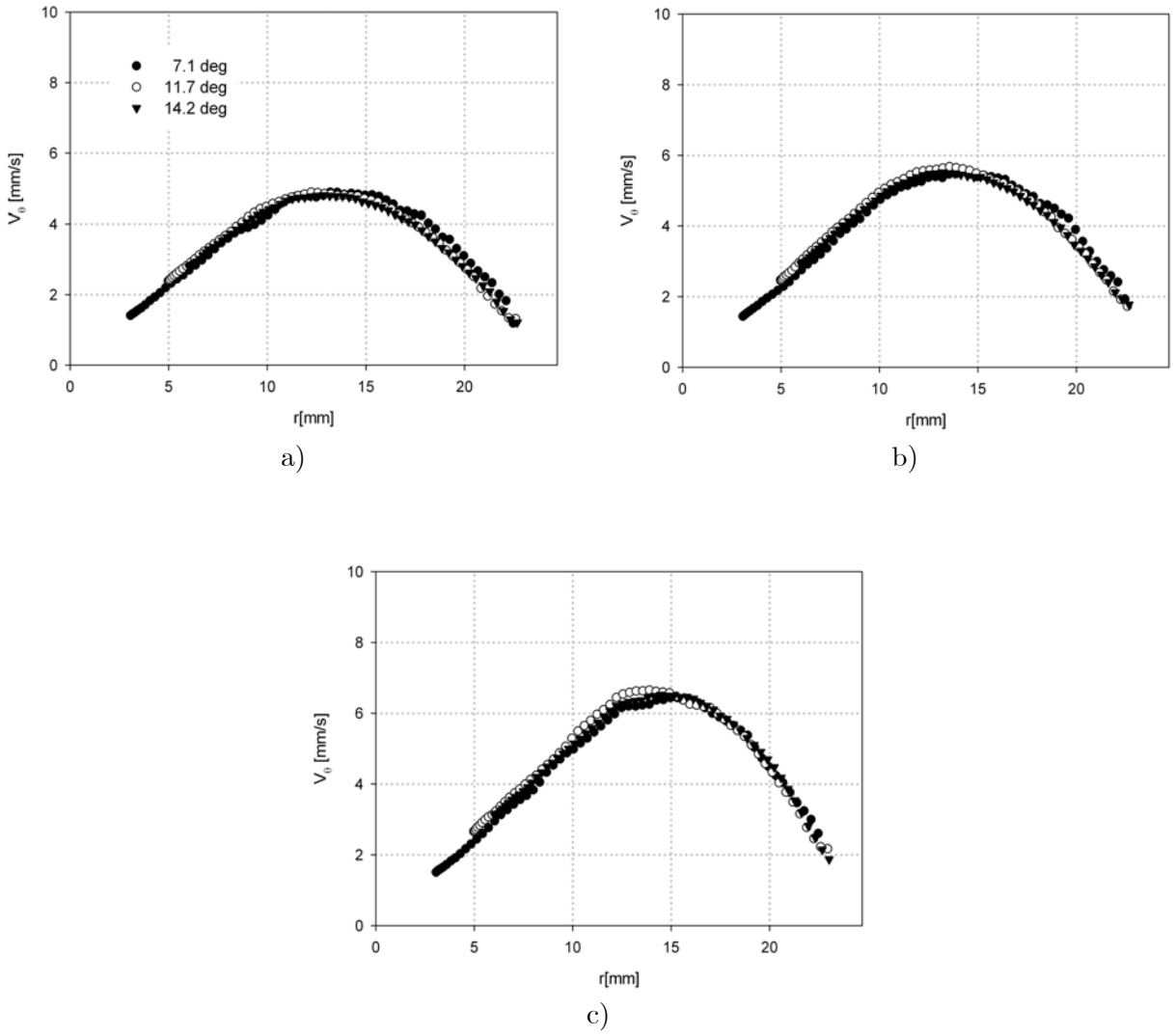

Figure C-2: Velocity profiles for EMG705 ferrofluid to frequency of 50Hz and a) 10.2mT rms b) 12.2mT rms and c) 14.4mT rms amplitude of the applied magnetic field.

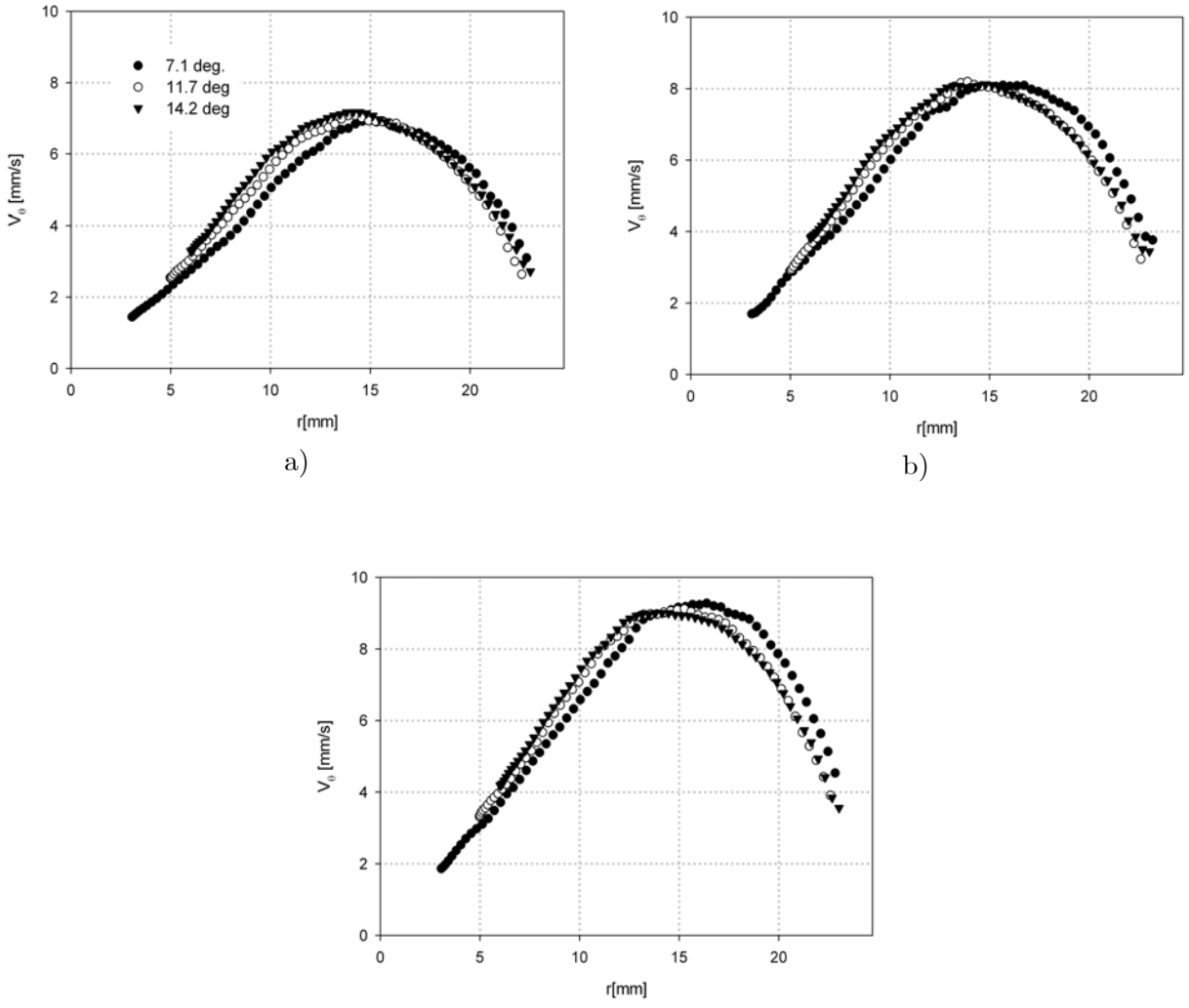

Figure C-3: Velocity profiles for EMG705 ferrofluid to frequency of 65Hz and a) 10.2mT rms b) 12.2mT rms and c) 14.4mT rms amplitude of the applied magnetic field.

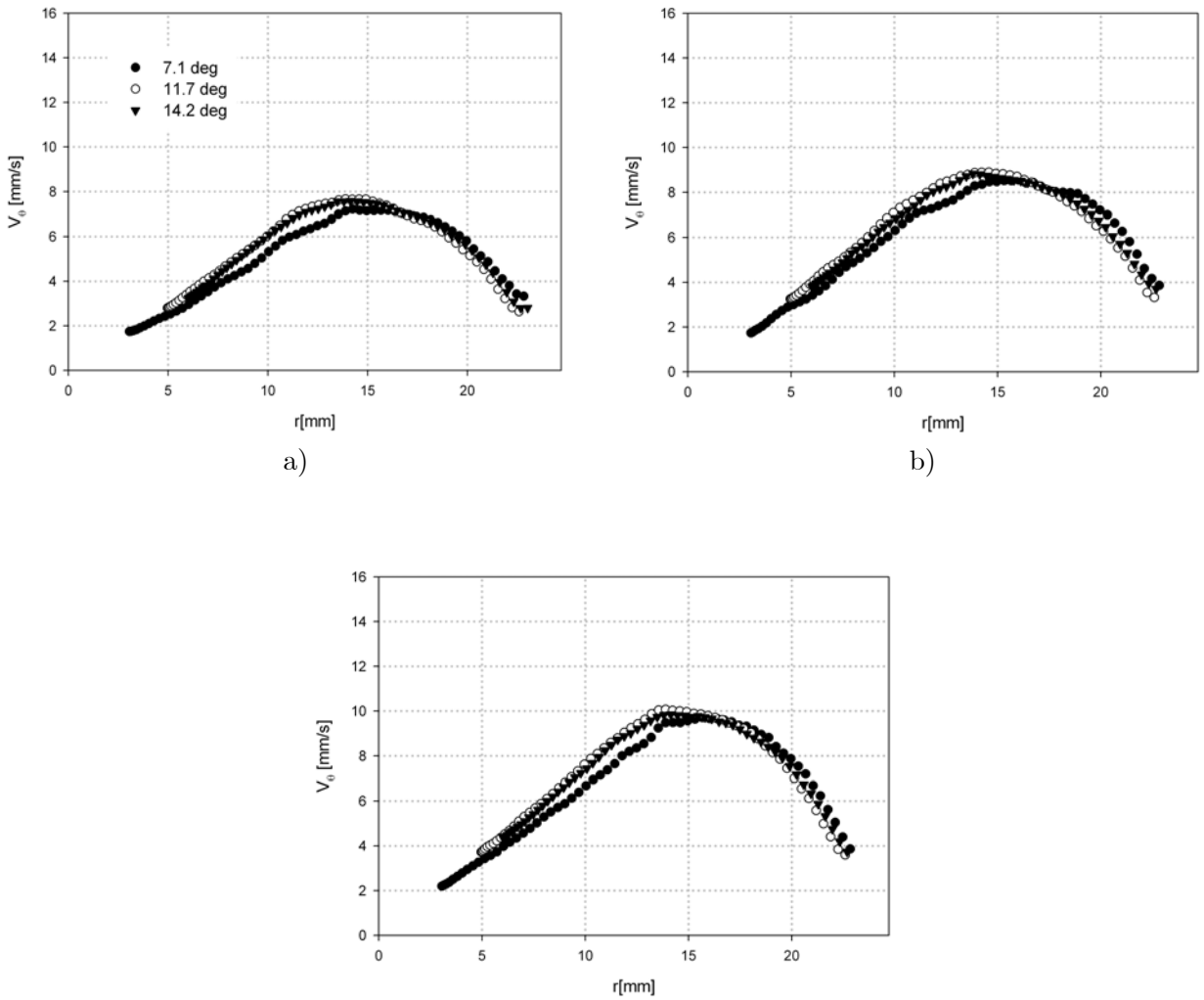

Figure C-4: Velocity profiles for EMG705 ferrofluid to frequency of 75Hz and a) 10.2mT rms b) 12.2mT rms and c) 14.4mT rms amplitude of the applied magnetic field.

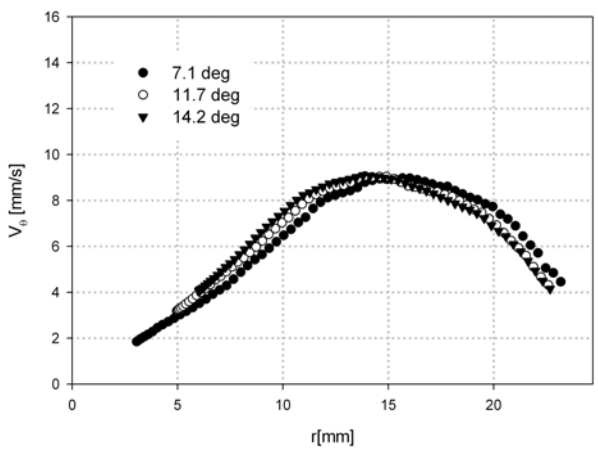

a)

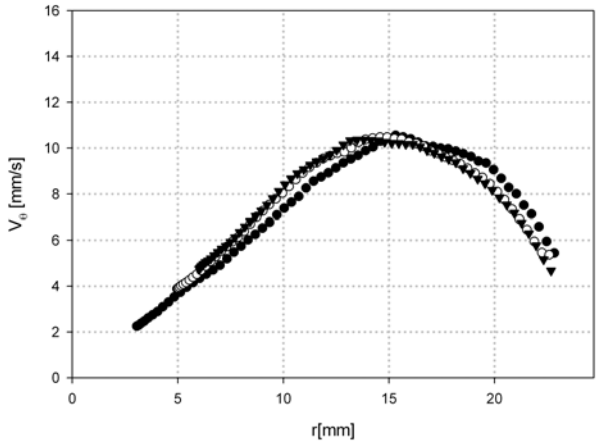

b)

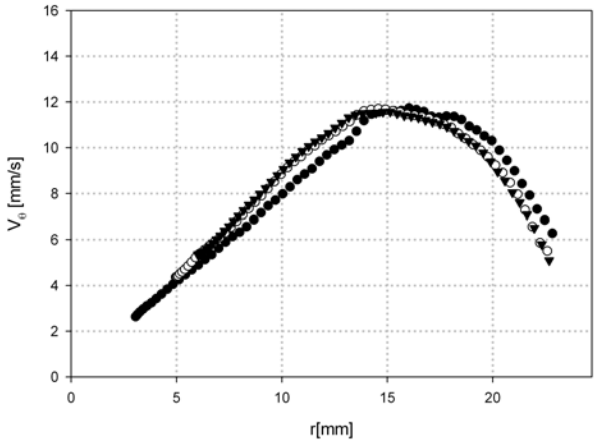

c)

Table C.1: Velocity profiles for EMG705 ferrofluid to frequency of 85Hz and a) 10.2mT rms b) 12.2mT rms and c) 14.4mT rms amplitude of the applied magnetic field.

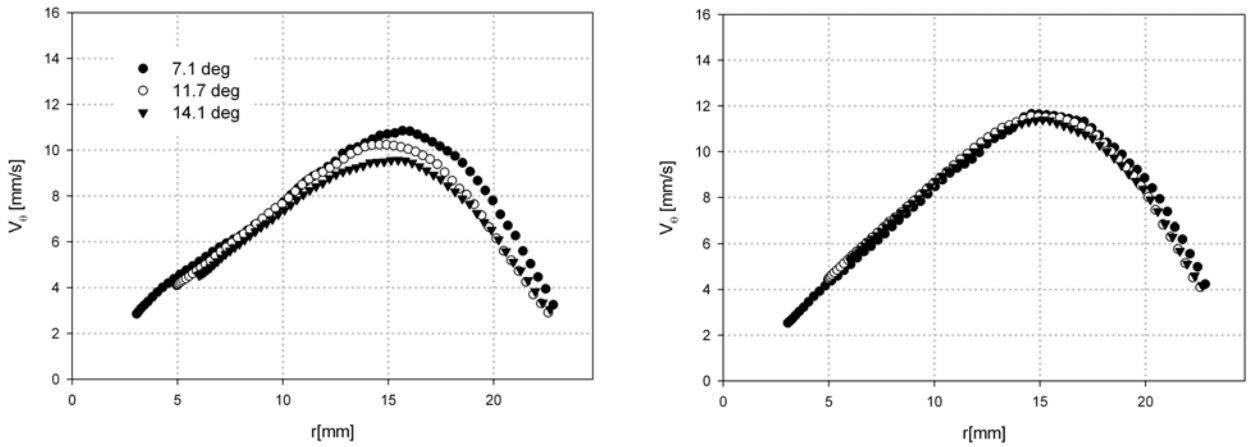

a) b)

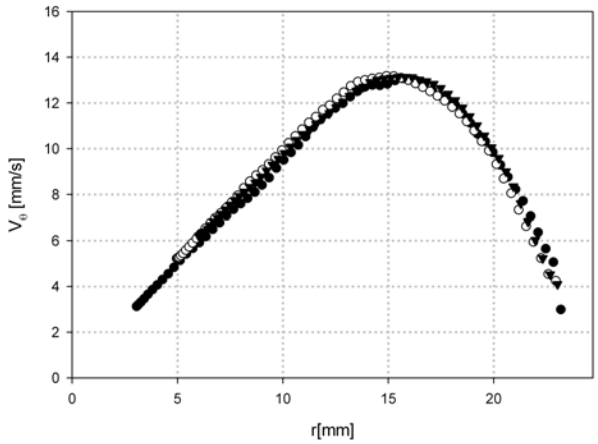

c)

Figure C-5: Velocity profiles for EMG705 ferrofluid to frequency of 100Hz and a) 10.2mT rms b) 12.2mT rms and c) 14.4mT rms amplitude of the applied magnetic field.

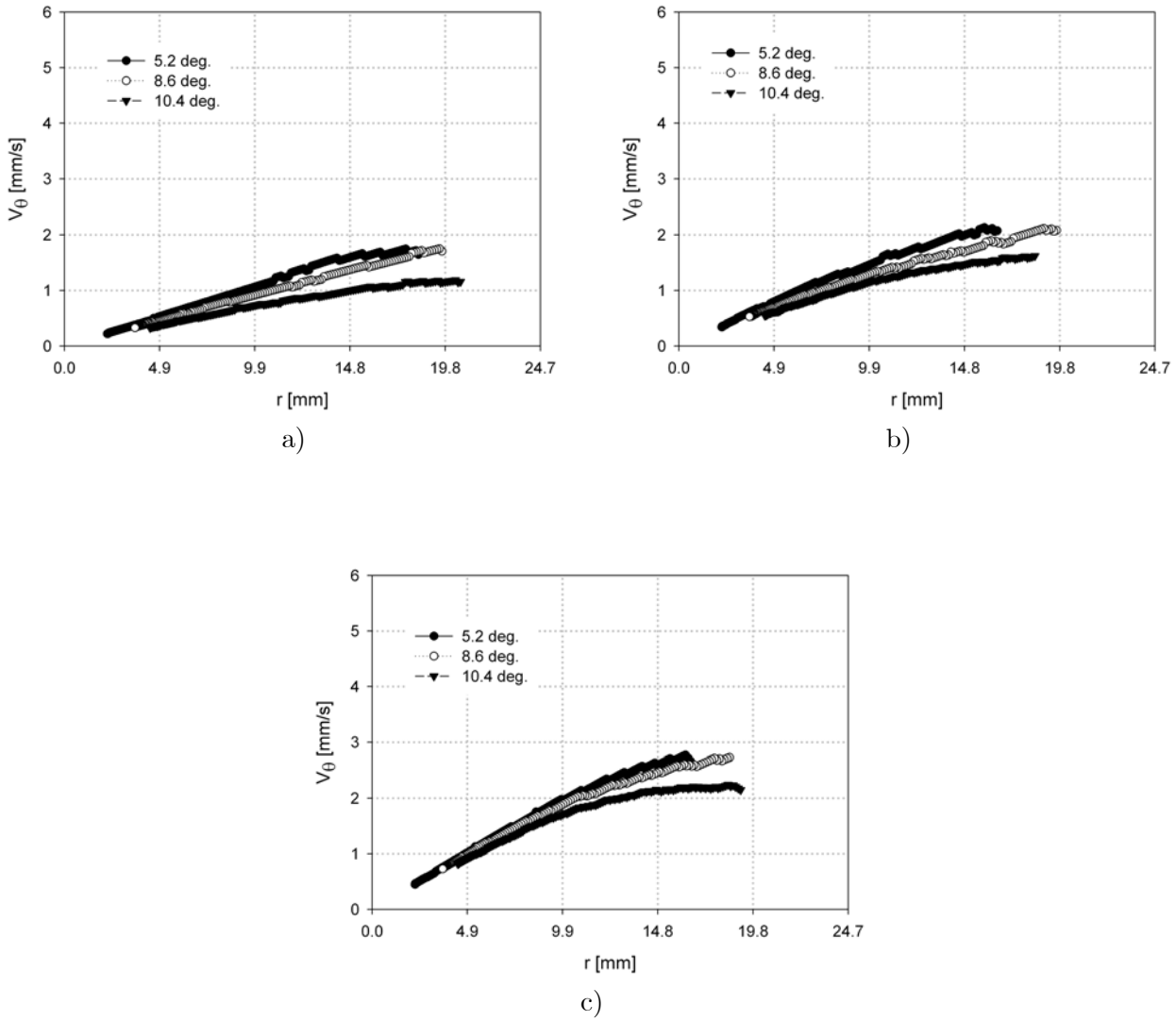

Figure C-6: Velocity profiles for EMG900-1 ferrofuid to frequency of 65Hz and a) 10.4mT rms b) 12.5mT rms and c) 14.6mT rms amplitude of the applied magnetic feld.

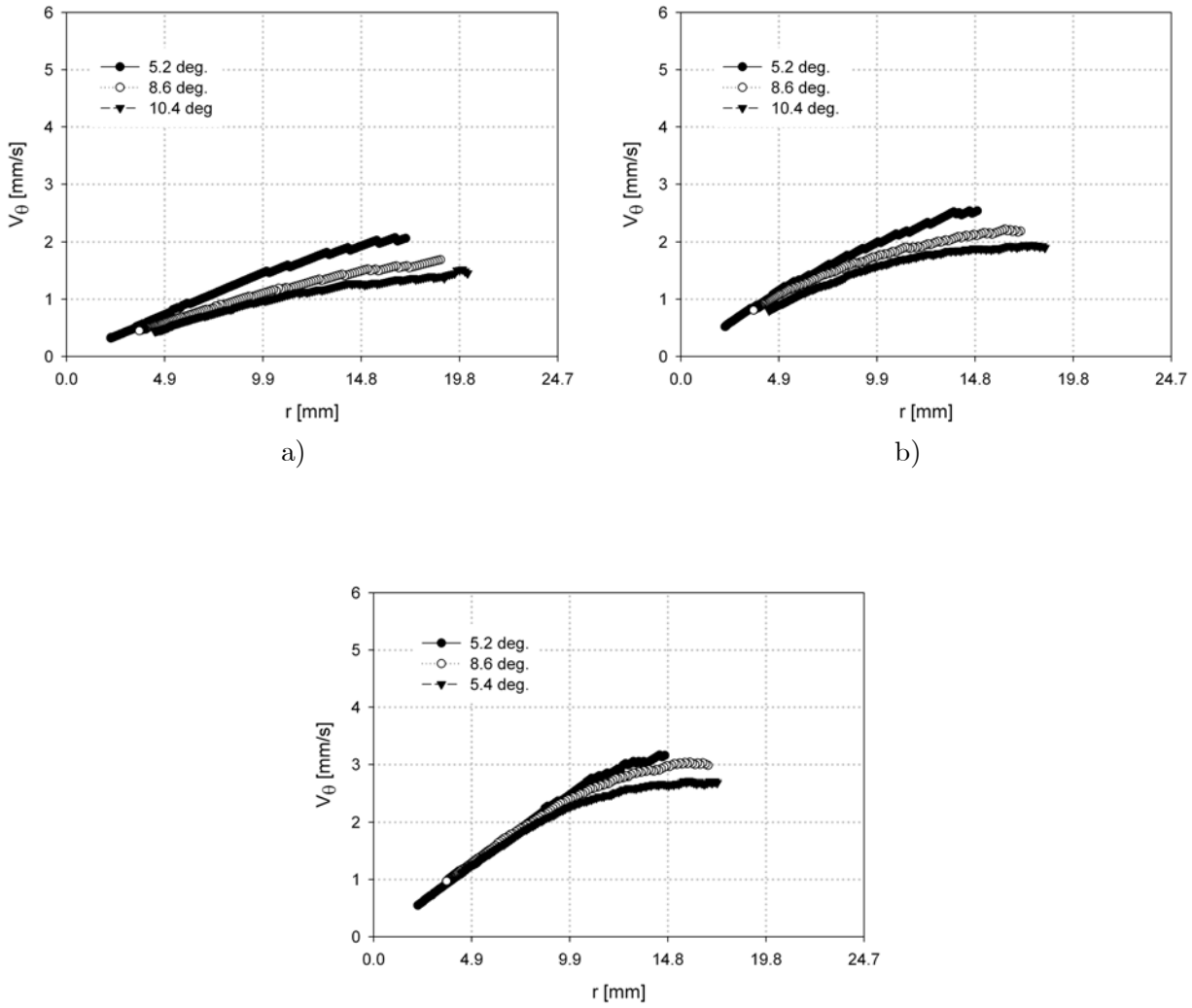

Figure C-7: Velocity profiles for EMG900-1 ferrofuid to frequency of 75Hz and a) 10.4mT rms b) 12.5mT rms and c) 14.6mT rms amplitude of the applied magnetic feld.

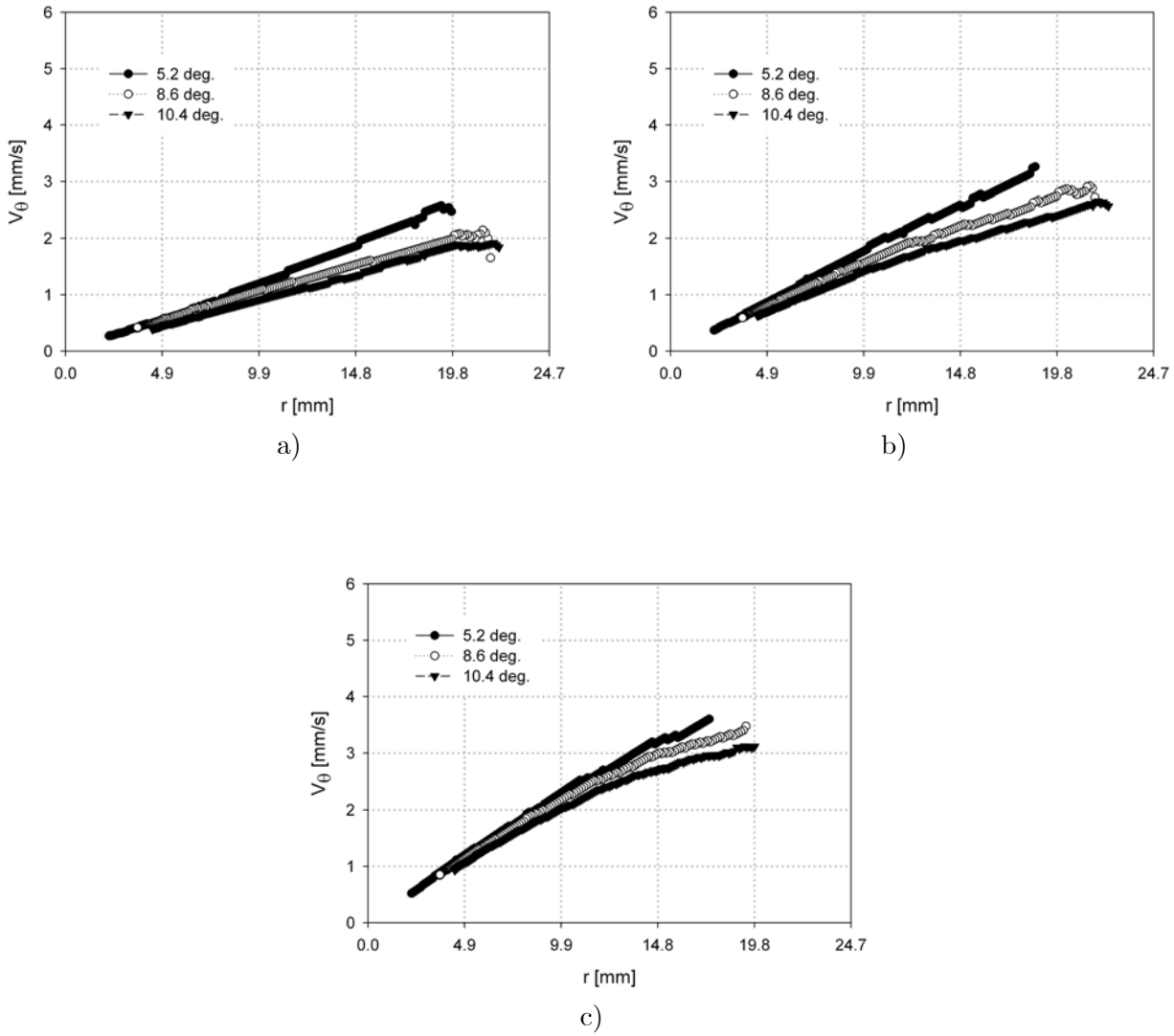

Figure C-8: Velocity profiles for EMG900-1 ferrofuid to frequency of 85 Hz and a) 10.4mT rms b) 12.5mT rms and c) 14.6mT rms amplitude of the applied magnetic feld.

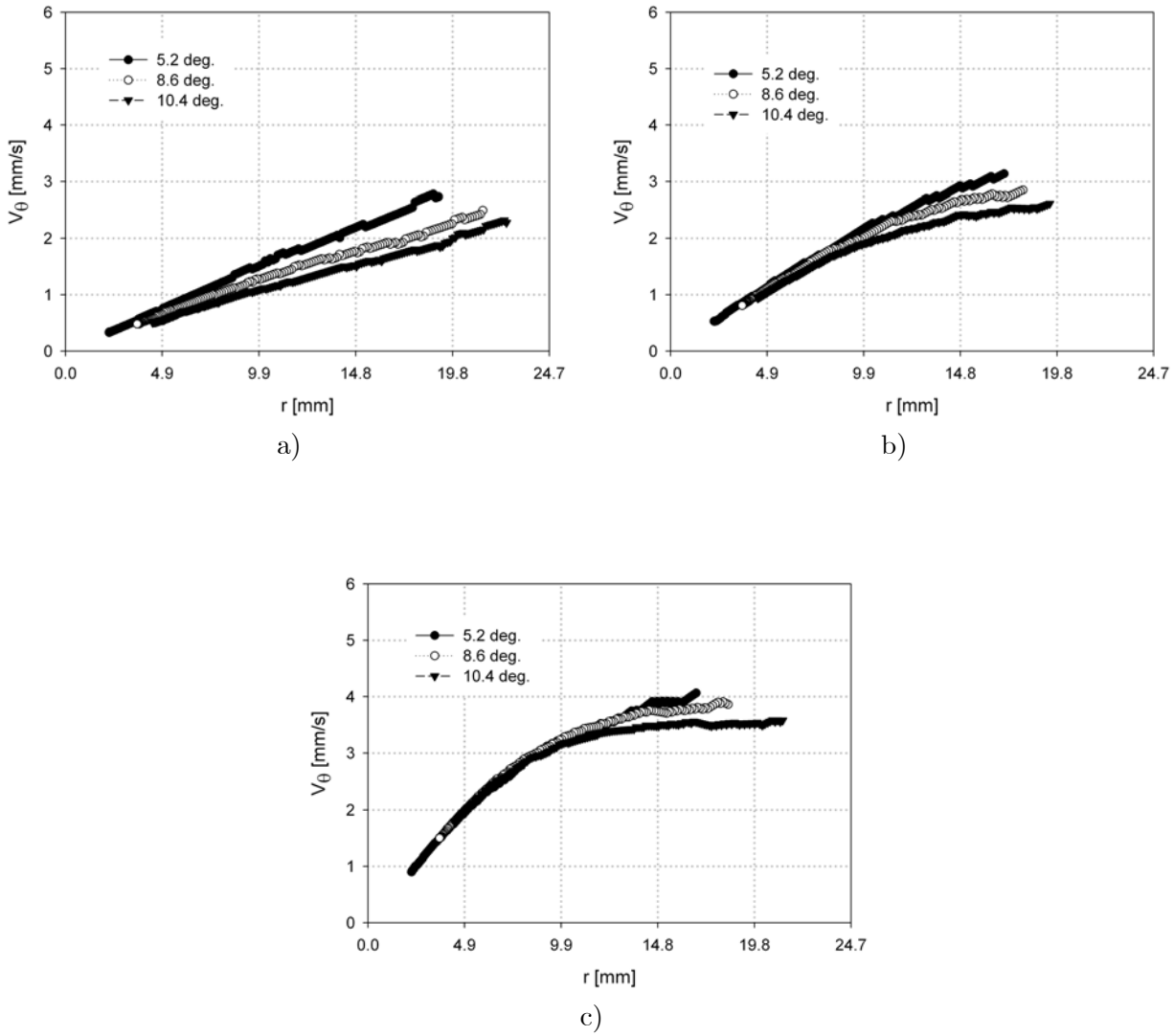

a) b)

c)

Figure C-9: Velocity profiles for EMG900-1 ferrofuid to frequency of 100Hz and a) 10.4mT rms b) 12.5mT rms and c) 14.6mT rms amplitude of the applied magnetic feld.

Appendix D

Torque measurements in spin up geometry

D.1 Torque measurements for EMG705 ferrofluid and its dilutions.

D.2 Torque measurements for EMG900 ferrofluid and its dilutions

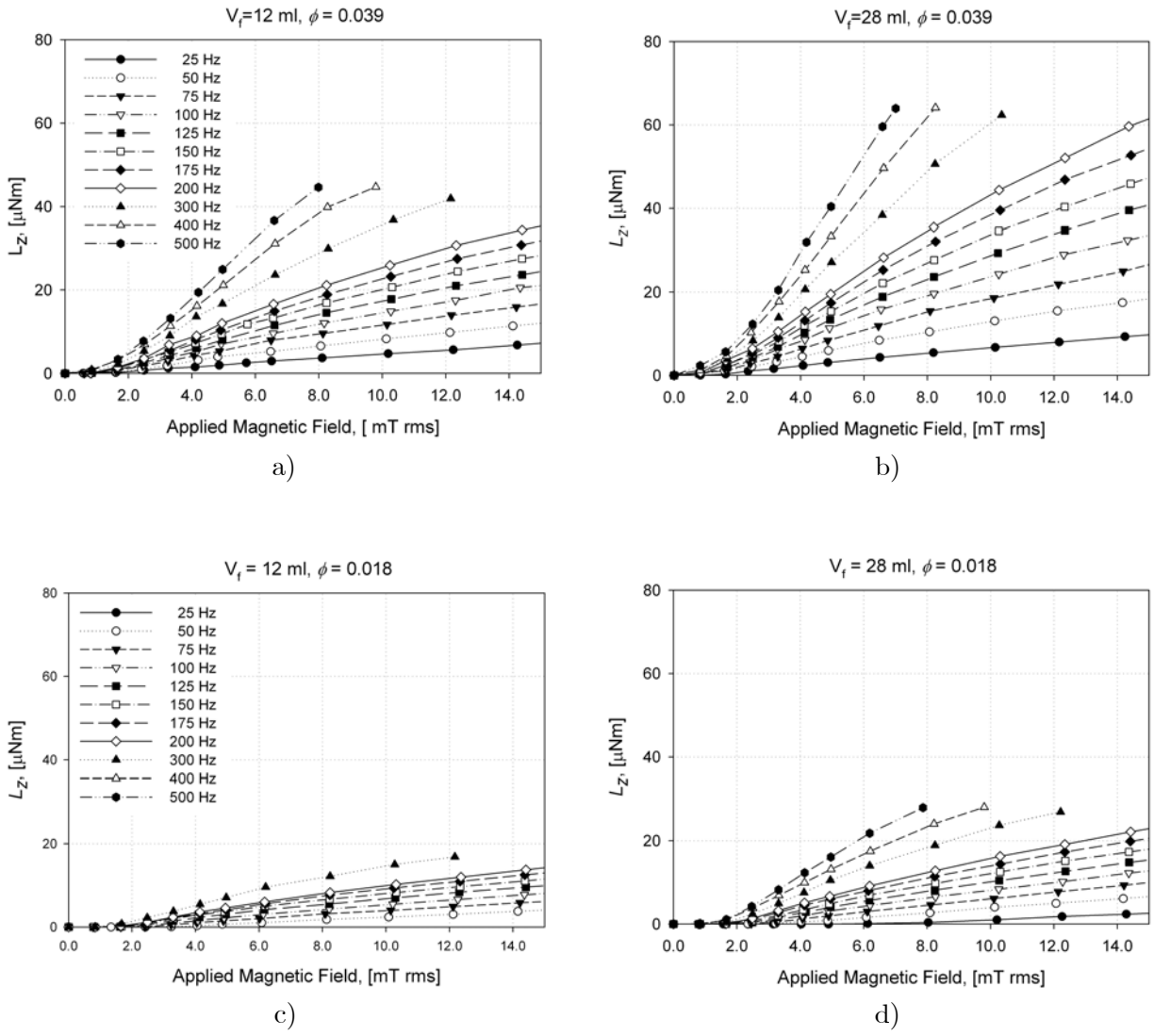

Figure D-1: Spin up torque measurements as function of the applied magnetic field and frequency for EMG705 and EMG705-1

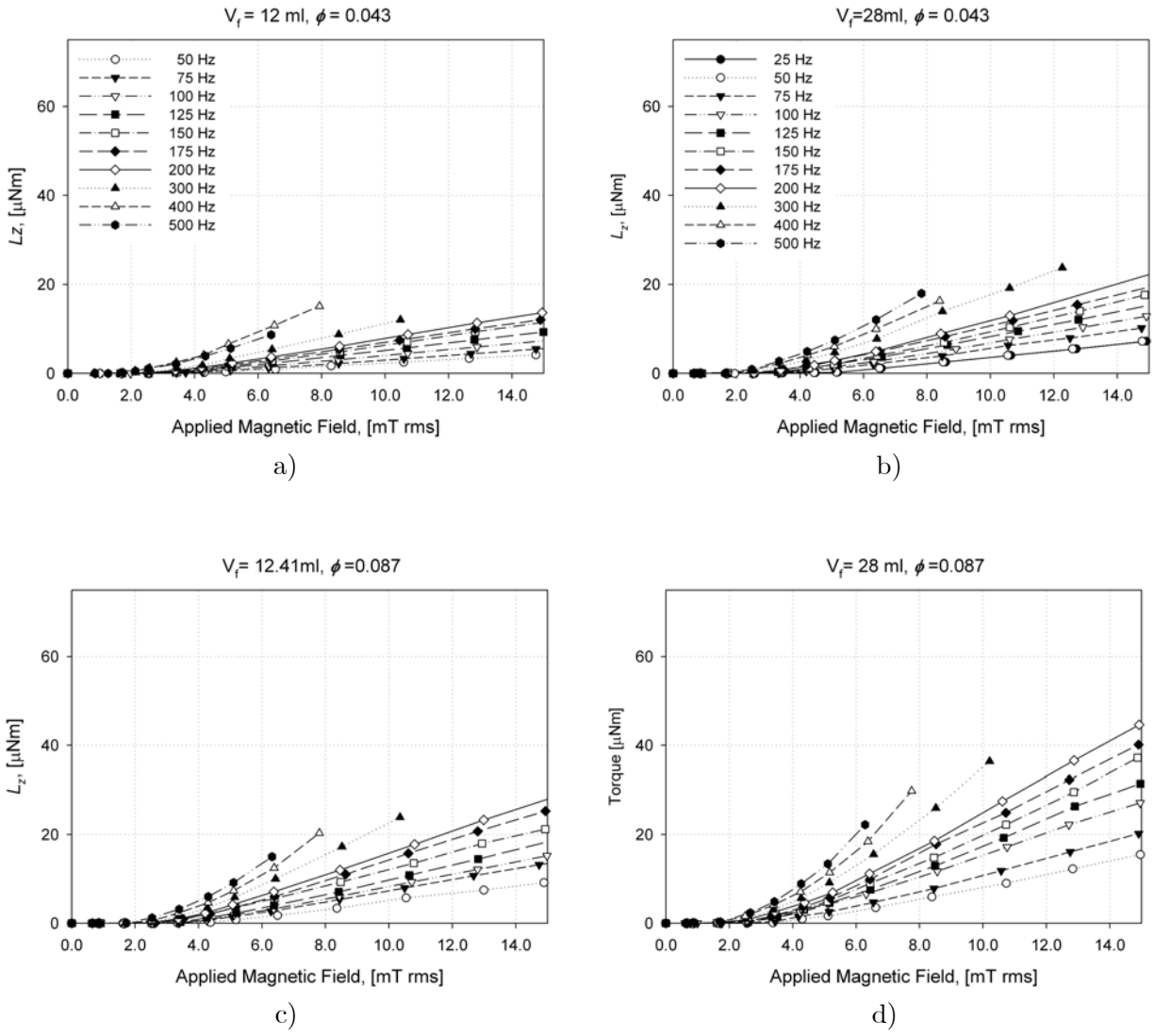

Figure D-2: Spin up torque for EMG900-1 and EMG900-2 as function of the applied magnetic field and frequency

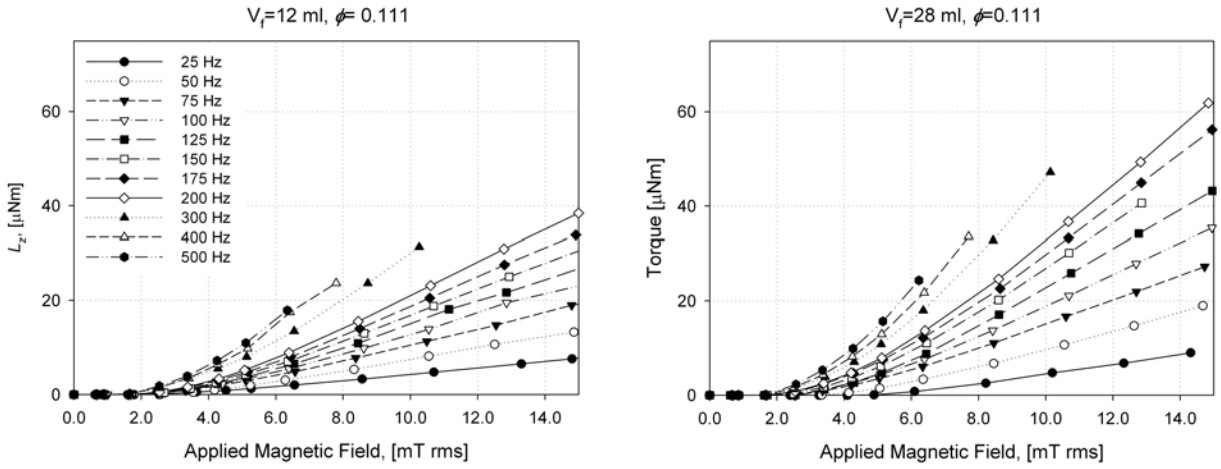

Figure D-3: Spin up torque for EMG900-3 as funtion of the applied magnetic field and frequency.

Appendix E

Velocity profile measurements for ferrofluid between coaxial cylinders

Velocity profiles measurements were carried out using probes placed in middle height of the container to tree different angles with respect to the diagonal and for frequencies of 85 Hz, 100 Hz, 125 Hz, and 150 Hz and amplitudes of 12 mT, 14.5 mT and 16.5 mT

E.1 Velocity profiles for EMG900-1 ferrofluid using $R_i = 9.3\,\mathrm{mm}$

E.2 Velocity profiles for EMG900-1 ferrofluid using $R_i = 4.9\,\mathrm{mm}$

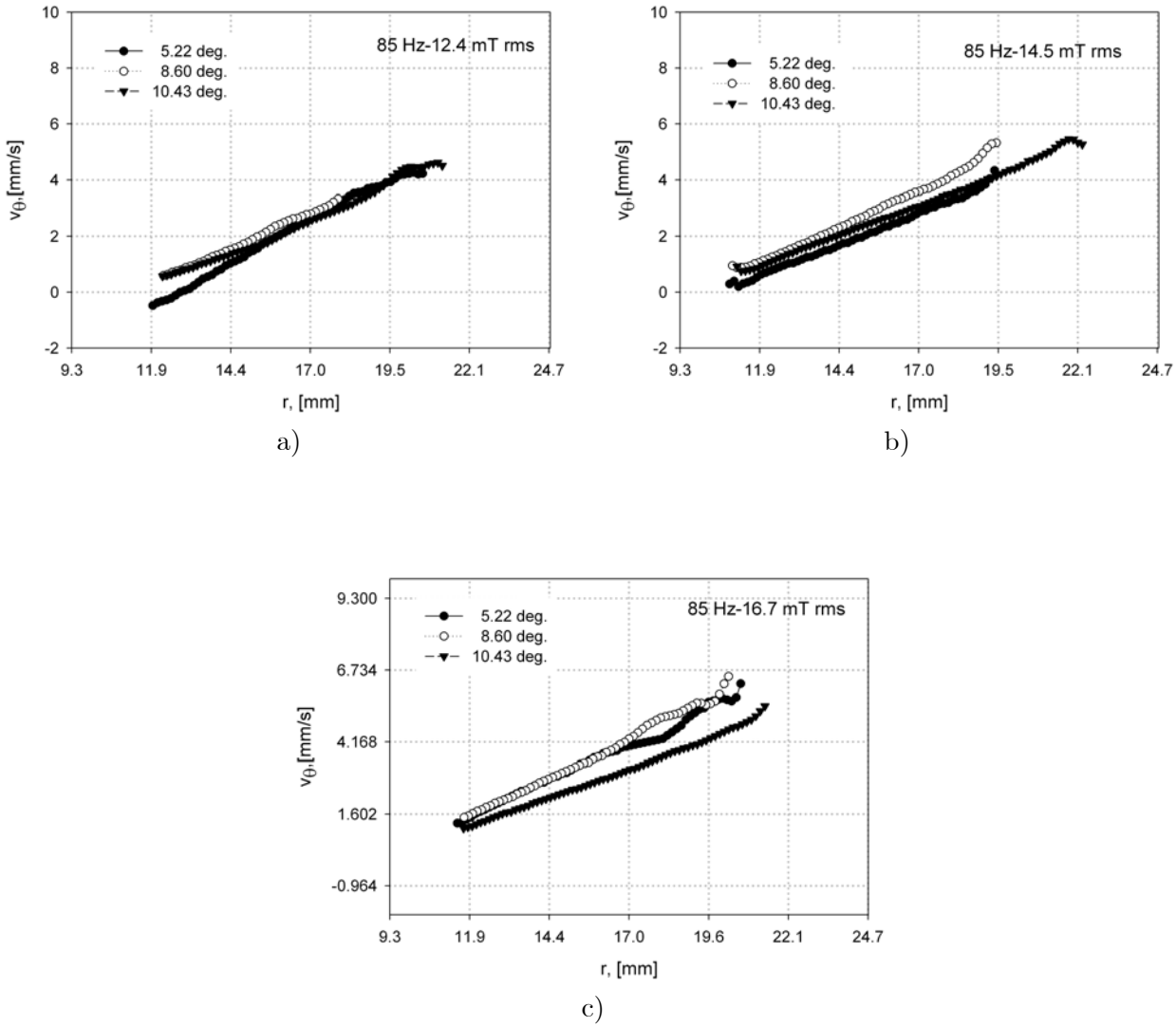

Figure E-1: Annular velocity profile for kerosene bsed ferrofluid for 85 Hz and a) 12.4 mT rms, b) 14.5 mT rms and c) 16.7 mT rms amplitudes of the applied magnetic field.

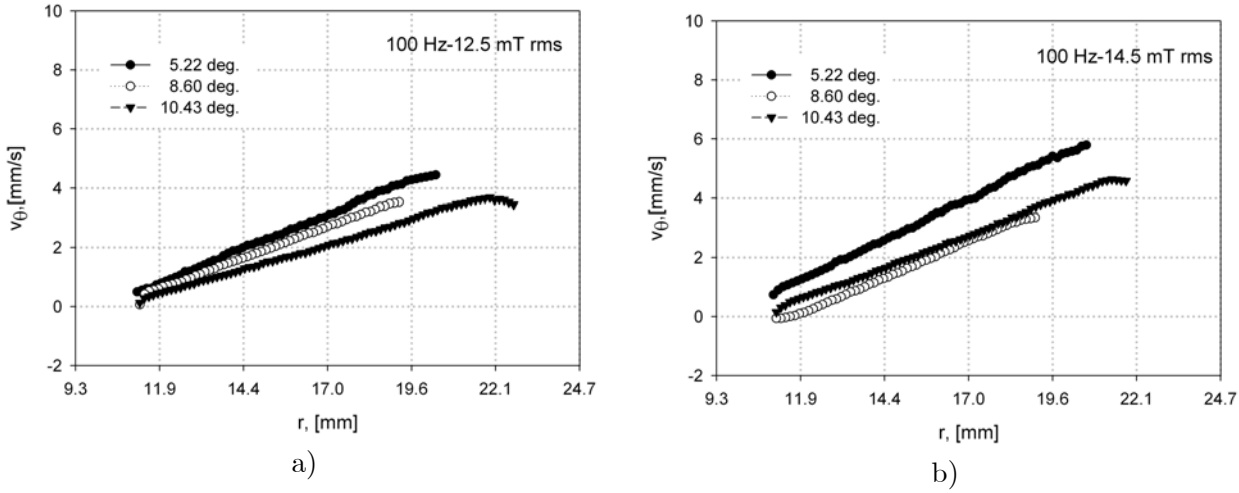

a)

b)

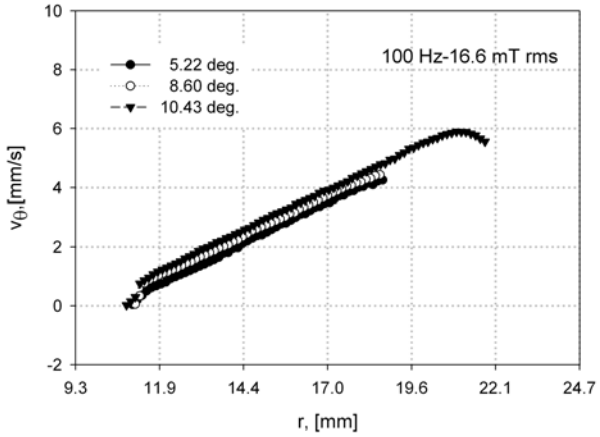

c)

Figure E-2: Annular velocity profile for kerosene bsed ferrofluid for 100 Hz and a) 12.5 mT rms, b) 14.5 mT rms and c) 16.6 mT rms amplitudes of the applied magnetic field. The internal diameter radius is 9.3 mm.

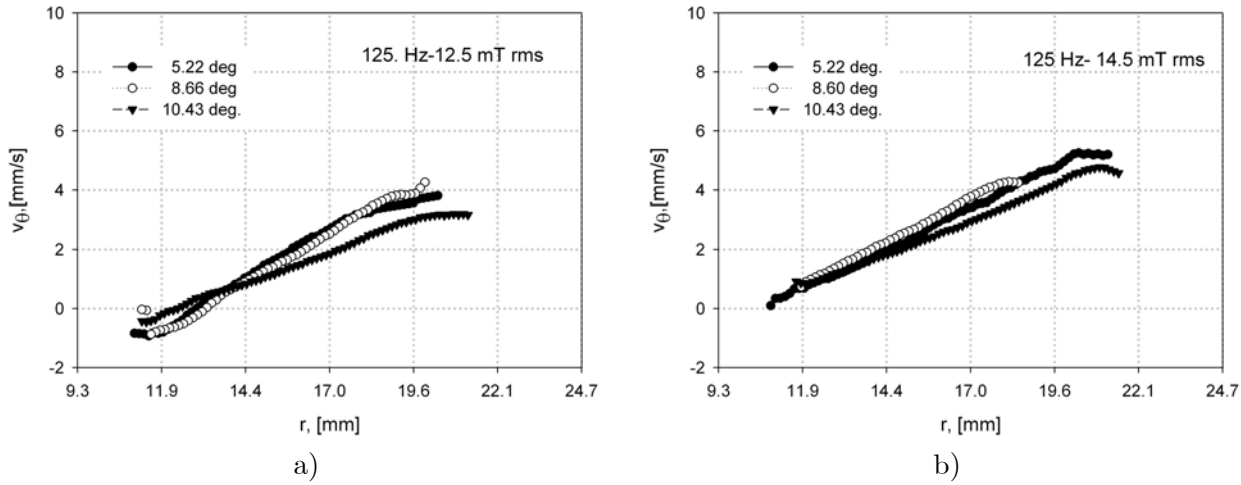

Figure E-3: Annular velocity profile for kerosene bsed ferrofluid for 125 Hz and a) 12.5 mT rms, b) 14.5 mT rms and c) 16.6 mT rms amplitudes of the applied magnetic field. The internal diameter radius is 9.3 mm.

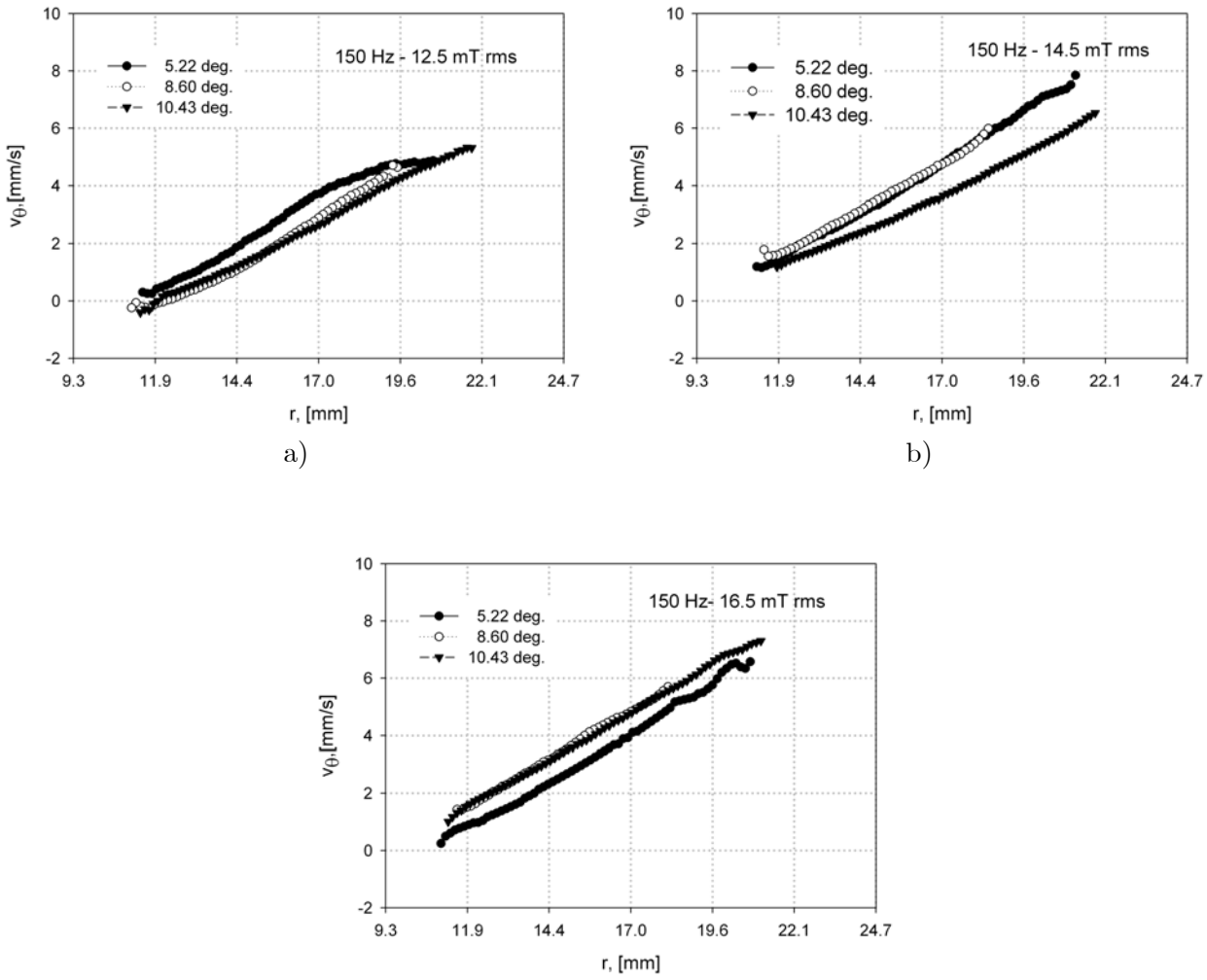

Figure E-4: Annular velocity profile for kerosene bsed ferrofluid for 150 Hz and a) 12.5 mT rms, b) 14.5 mT rms and c) 16.5 mT rms amplitudes of the applied magnetic field.

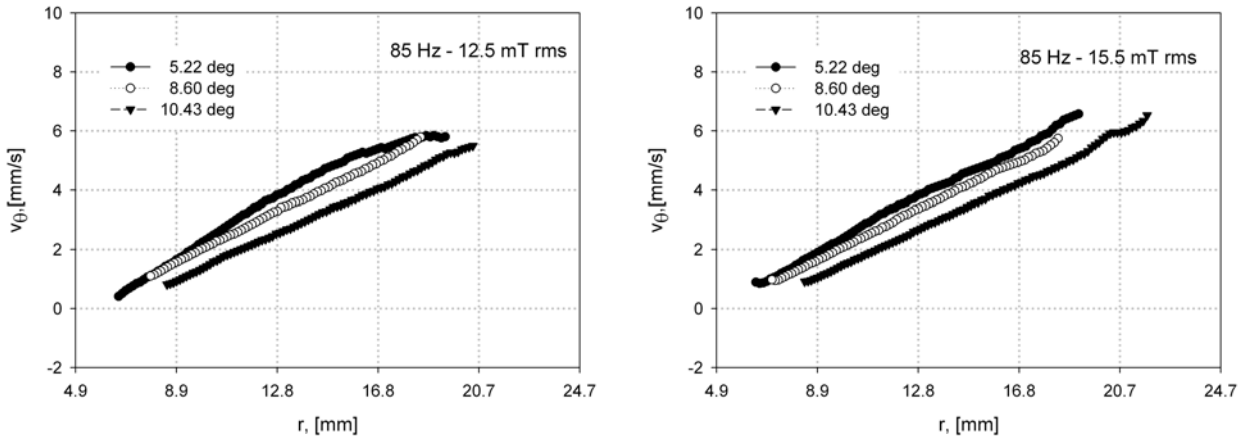

a)

b)

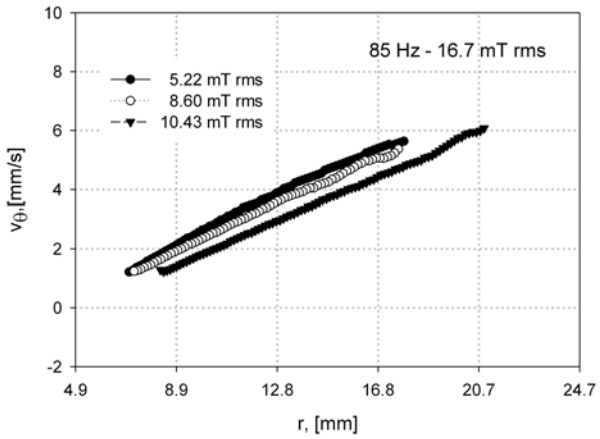

c)

Figure E-5: Annular velocity profile for kerosene bsed ferrofluid for 85 Hz and a) 12.5 mT rms, b) 14.5 mT rms and c) 16.6 mT rms amplitudes of the applied magnetic field. The internal diameter radius is 4.9 mm.

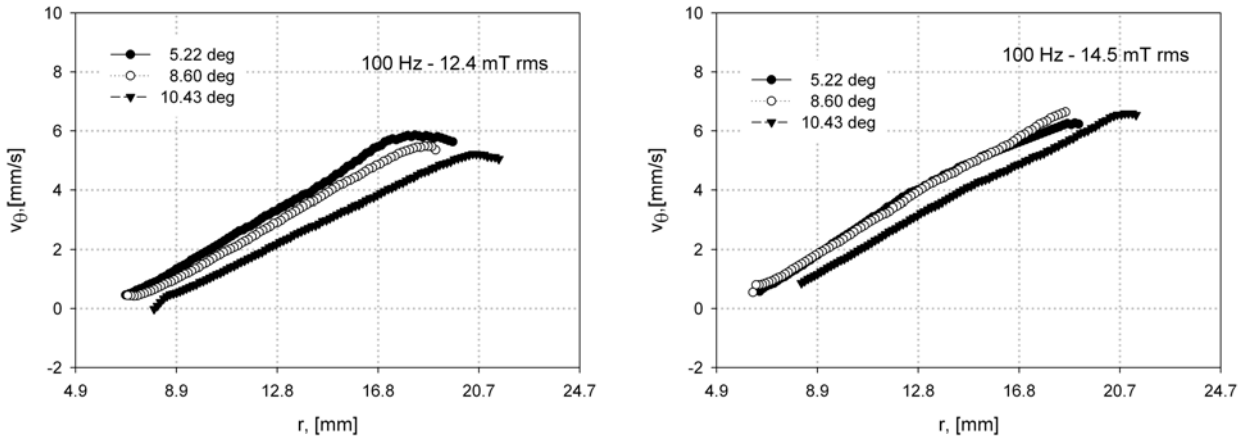

a)

b)

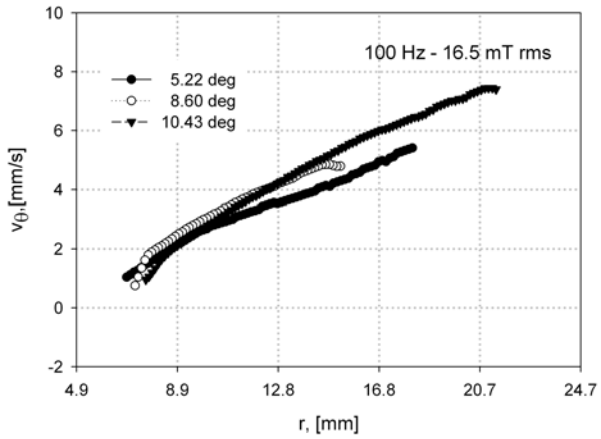

c)

Figure E-6: Annular velocity profile for kerosene bsed ferrofluid for 125 Hz and a) 12.5 mT rms, b) 14.5 mT rms and c) 16.6 mT rms amplitudes of the applied magnetic field. The internal diameter radius is 4.9 mm.

Appendix F

Experimental torque measurements in annular geometry

F.1 For EMG705 ferrofluid and their dilutions

F.2 For EMG900 ferrofluid and their dilutions

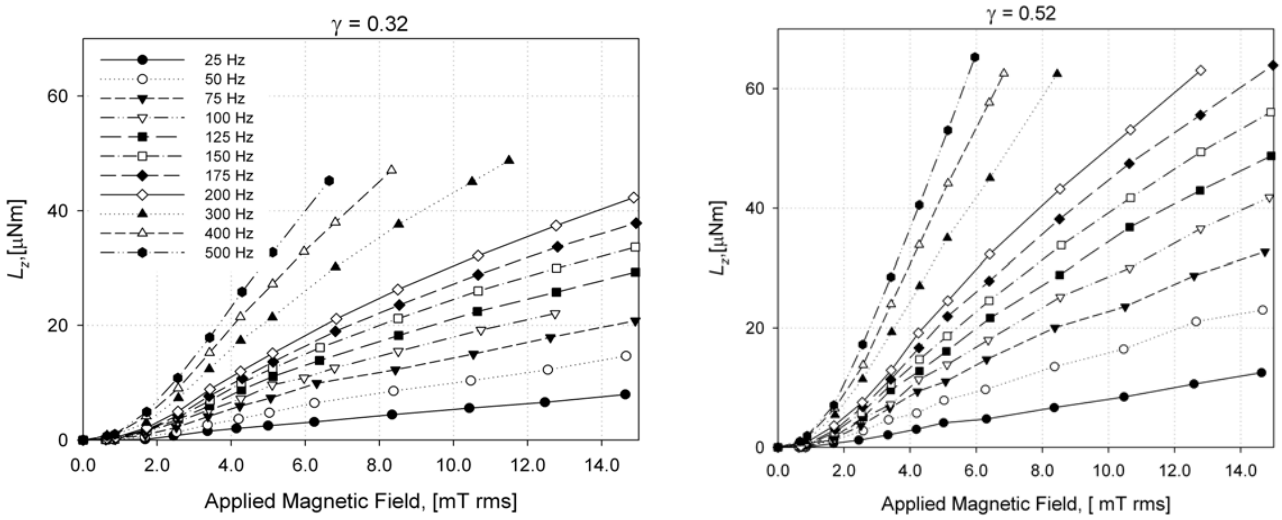

a) b)

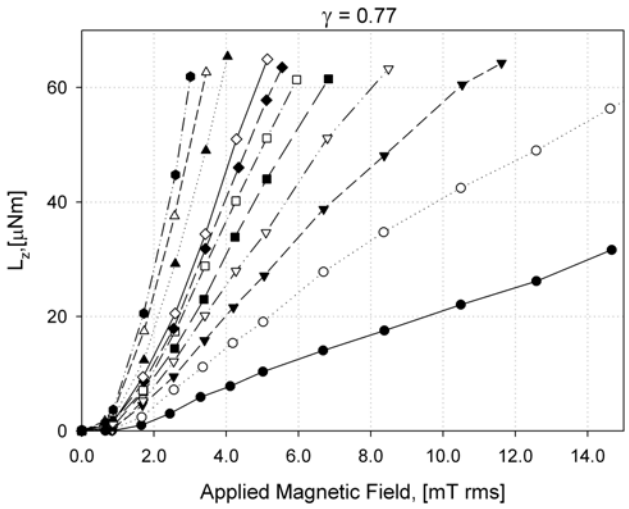

c)

Figure F-1: Torque measurements in annular geometry for EMG705

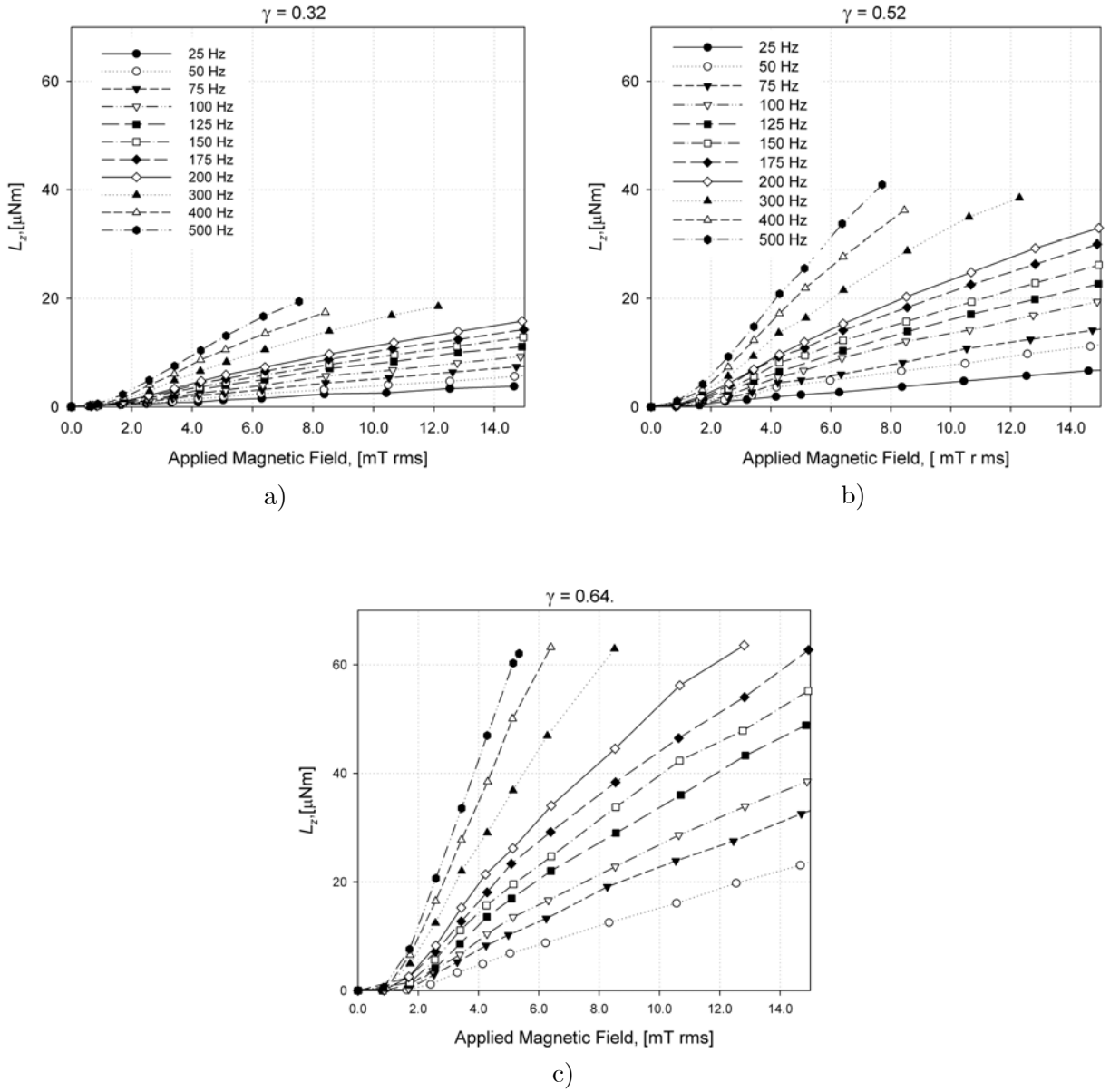

Figure F-2: experimental annular torque measurements for EMG705-1

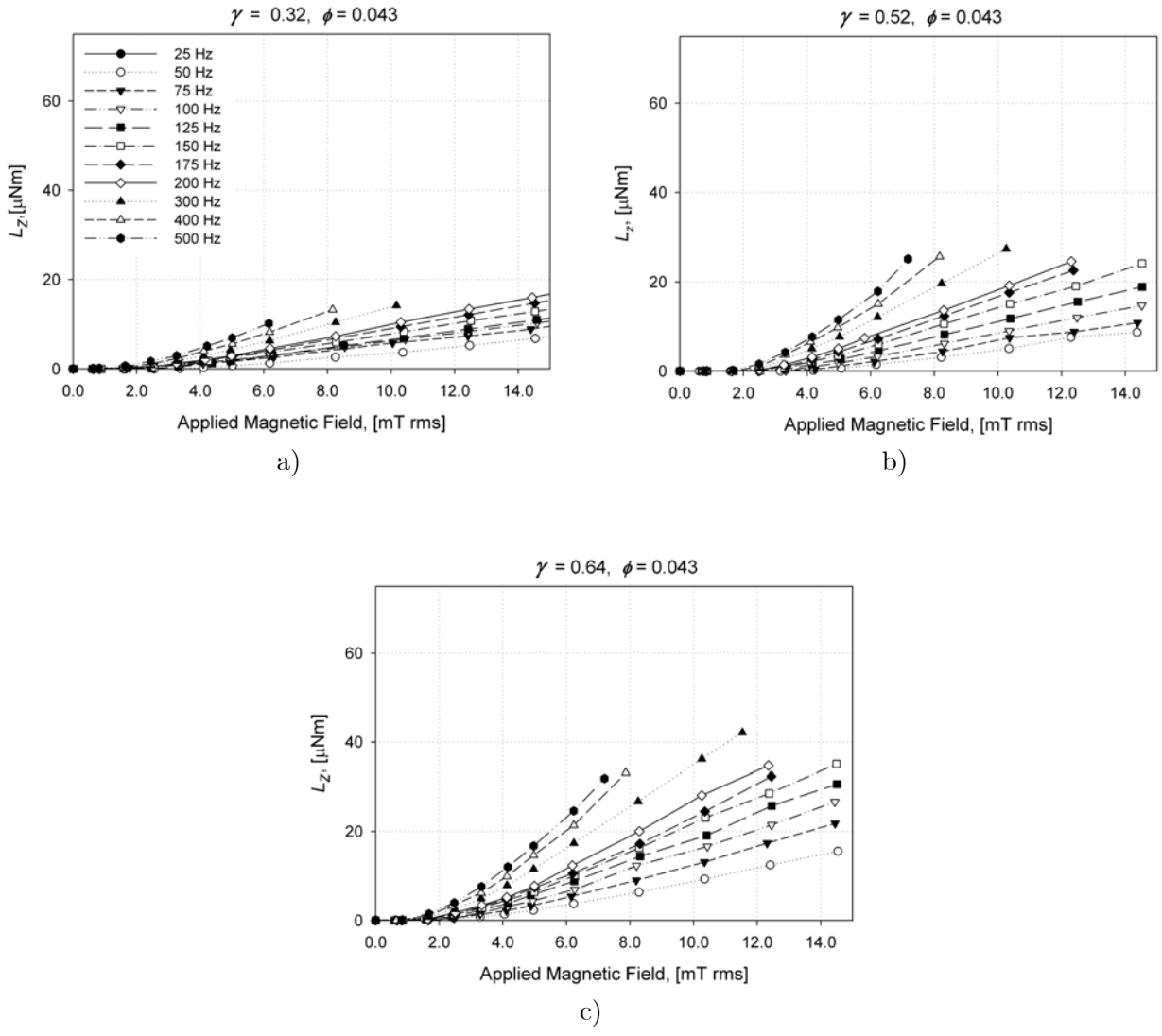

Figure F-3: Annular torque measurements for EMG900-1as function of the applied magnetic field and frequency

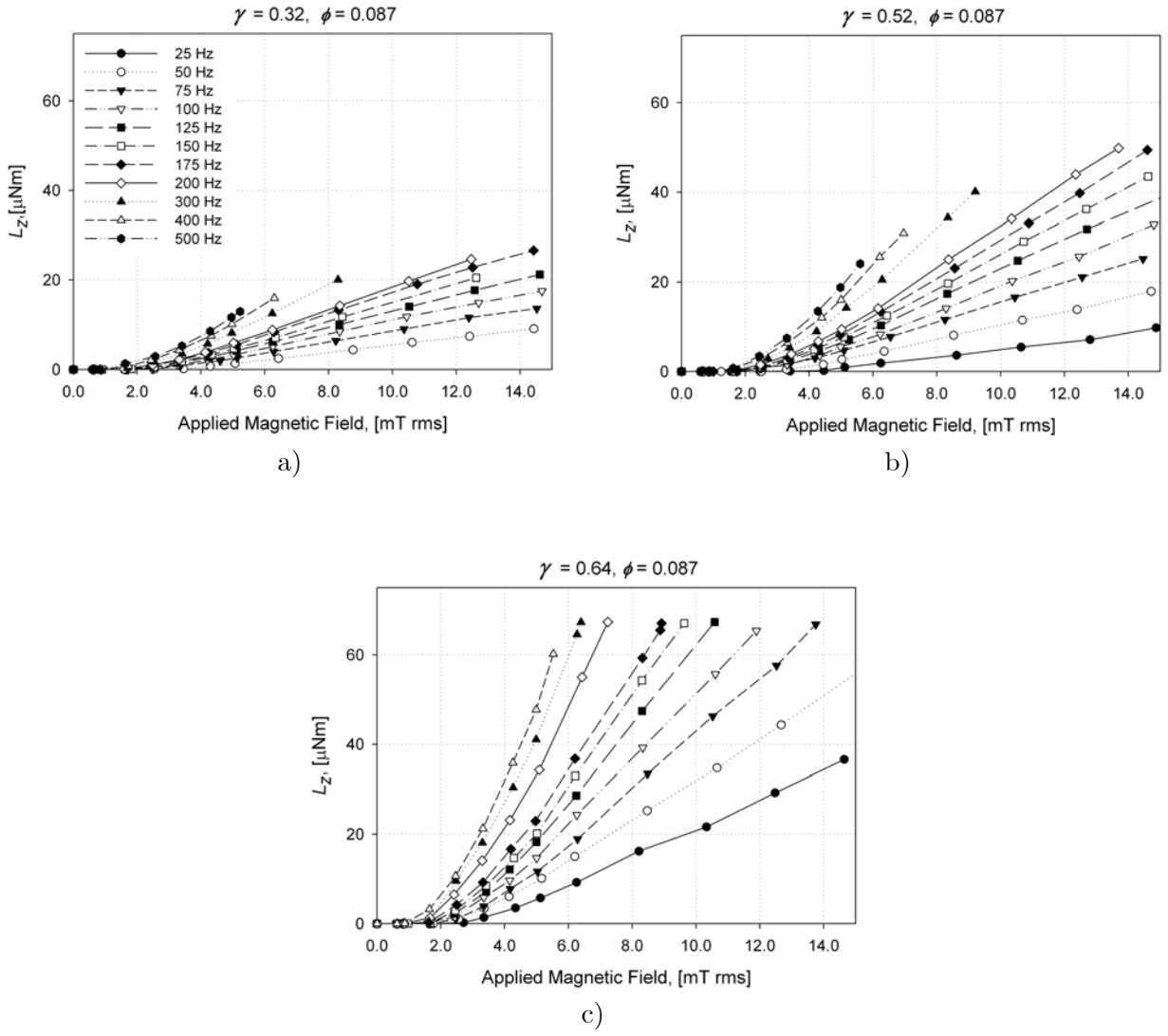

Figure F-4: Annular torque measurements for EMG900-2 as a function of amplitude and frequency of the applied magnetic field

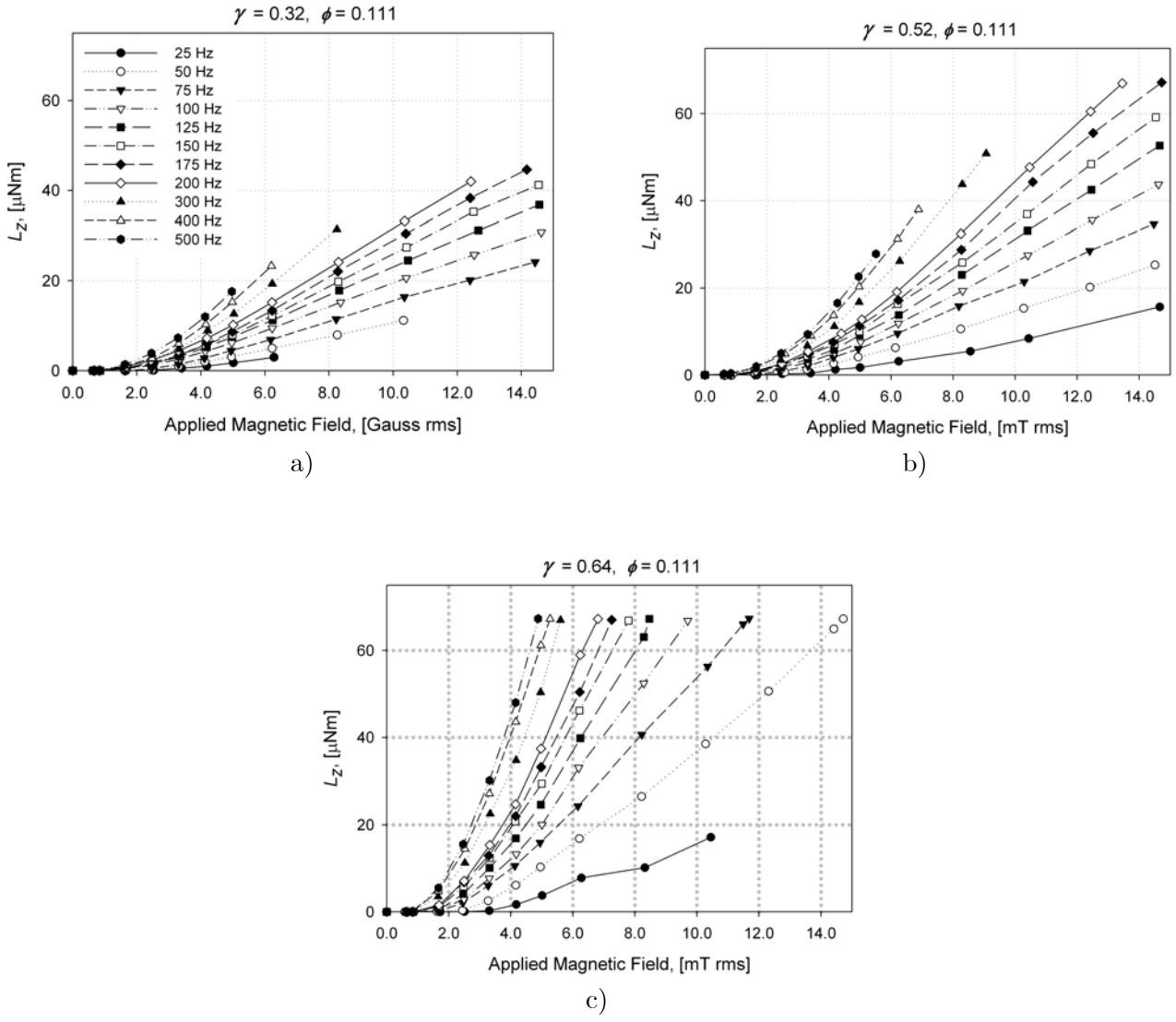

Figure F-5: Torque in annular geometry for EMG900-3 as function of the amplitude and frequency of the applied magnetic field.

Bibliography

[1] Rosensweig, R. E., *Ferrohydrodynamics*, Dover Publications, Mineola, NY, 1997.

[2] Rosensweig, R. E., "Magnetic fluids," *Annuals Reviews of Fluid Mechanics*, Vol. 19, 1987, pp. 437–463.

[3] Neuringer, J. and Rosensweig, R. E., "Ferrohydrodynamics," *The Physics of Fluids*, Vol. 7, No. 12, 1964, pp. 1927–1937.

[4] Odenbach, S., *Magnetoviscous effects in ferrofluids*, Vol. 71 of *Lecture notes in physics, Monographs*, Springer-Verlag, Germany, 2002.

[5] Hall, W. and Busenberg, S., "Viscosity of magnetic suspensions," *The Journal of Chemical Physics*, Vol. 51, 1969, pp. 137–144.

[6] Shliomis, M. I. and Morozov, K. I., "Negative viscosity of ferrofluid under alternating magnetic field," *Physics of Fluids*, Vol. 6, No. 8, 1994, pp. 2855–2861.

[7] Bacri, J. C. and Perzynsky, R., ""Negative-viscosity" Effect in a magnetic fluid," *Physical Review Letters*, Vol. 75, No. 11, 1995, pp. 2128–2131.

[8] Moskowitz, R. and Rosensweig, R., "Nonmechanical torque-driven flow of a ferromagnetic fluid by an electromagnetic field," *Applied Physics Letters*, Vol. 11, No. 10, 1967, pp. 301–303.

[9] Brown, R. and Horsnell, T. S., "The wrong way round," *Electrical Review*, Vol. 183, 1969, pp. 235–236.

[10] Raj, R., Moskowitz, B., and Casciari, R., "Advances in ferrofluid technology," *Journal of Magnetism and Magnetic Materials*, Vol. 149, 1995, pp. 174–180.

[11] Roger, J., Pons, J., Massart, R., Halbreich, A., and Bacri, J., "Some biomedical applications of ferrofluids," *The European Physical Journal of Applied Physics*, Vol. 5, 1999, pp. 321–325.

[12] Shliomis, M. I., *Ferrohydrodynamics: Retropective and issues, in "Ferrofluids, magnetically controllable fluids and their applications"*, Vol. 594 of *Lecture Notes in Physics*, Springer, Berlin, 2002.

[13] Rosenthal, A. D., Rinaldi, C., Franklin, T., and Zahn, M., "Torque measurements in spin-up flow of ferrofluids," *Journal of Fluids Engineering*, Vol. 126, 2004, pp. 198–205.

[14] Tsebers, A. O., "Interfacial stresses in the hydrodynamics of liquids with internal rotation," *Magnitnaya Gidrodynamika*, Vol. 11, No. 1, 1975, pp. 79–82.

[15] Pshenichnikov, A. F. and Lebedev, A. V., "Tangential stresses on the magnetic fluid boundary and the rotational effect," *Magnetohydrodynamics*, Vol. 36, No. 4, 2000, pp. 254–263.

[16] Rinaldi, C., Gutman, F., He, X., Rosenthal, A. D., and Zahn, M., "Magnetoviscosity and torque measurements on ferrofluid cylinder in rotating magnetic fields," *Journal of Magnetism and Magnetic Materials*, Vol. 289, 2005, pp. 307–310.

[17] Rosensweig, R. E., Popplewell, J., and Johnston, R. J., "Magnetic fluid motion in rotating field," *Journal of Magnetism and Magnetic Materials*, Vol. 85, 1990, pp. 171–180.

[18] Kikura, H., Sawada, T., and Tanahashi, T., "Transportation of a magnetic fluid by rotating magnetic field," *Third international ISEM symposium on the application of electromagnetic forces.*, edited by J. T. T. Tani, Electromagnetic forces and applications. Elsevier Science Ltd., Sendai, Japan., 28-30 January 1991, pp. 103–106.

[19] Zaitsev, V. M. and Shliomis, M. I., "Entrainment of ferromagnetic suspension by a rotating field," *Journal of Applied Mechanics and Technical Physics*, Vol. 10, 1969, pp. 696–700.

[20] Jenkins, J., "Some simple flows of a para-magnetic fluid," *Journel de Physique.*, Vol. 32, 1971, pp. 931.

[21] Glazov, O. A., "Motion of a ferrosuspension in rotating magnetic fields," *Magnitnaya Gidrodynamika*, Vol. 11, No. 2, 1975, pp. 16–22.

[22] Rinaldi, C., *Continuum modeling of polarizable systems*, Ph.d. thesis, Massachussetts Institute of Technology, Cambridge, MA. 2002.

[23] Rinaldi, C., "Effect of the particle size distribution on Brownian and Néel relaxations times of ferrofluids," Personal Communication 2005.

[24] Glazov, O., "Role of higher harmonics in ferrosuspension motion in a rotating magnetic field," *Magnitnaya Gidrodynamika*, Vol. 11, No. 4, 1975, pp. 31.

[25] Glazov, O. A., "Velocity profiles for magnetic fluids in rotating magnetic fields," *Magnitnaya Gidrodynamika*, Vol. 18, No. 1, 1982, pp. 27.

[26] Rosensweig, R. E. and Johnston, R. J., "Aspects of magnetic fluid flow with nonequilibrium magnetization," *Continuum Mechanics and its Applications*, edited by C. Graham and S. Malik, Hemisphere Publishing Company, 1989, pp. 707–729.

[27] Lebedev, A. V. and Pshenichnikov, A. F., "Motion of a magnetic fluid in a rotating magnetic field," *Magnitnaya Gidrodynamika*, Vol. 27, No. 1, 1991, pp. 7–12.

[28] Lebedev, A. V. and Pschenichnikov, A., "Rotational effect: The influence of free or solid moving boundaries," *Journal of Magnetism and Magnetic Materials*, Vol. 122, 1993, pp. 227–230.

[29] Kaloni, P. N., "Some Remarks on the Boundary-Conditions for Magnetic Fluids," *International Journal of Engineering Science*, Vol. 30, No. 10, 1992, pp. 1451–1457.

[30] Rosensweig, R. E., "Role of internal rotations in selected magnetic fluid applications," *Magnitnaya Gidrodynamika*, Vol. 36, No. 4, 2000, pp. 241–253.

[31] Pshenichnikov, A. F., Lebedev, A. V., and Shliomis, M. I., "On the rotational effect in nonuniform magnetic fluids," *Magnetohydrodynamics*, Vol. 36, No. 4, 2000, pp. 275–281.

[32] Kagan, I., Rykov, V., and Yantovskii, E. I., "Flow of a dielectric ferromagnetic suspension in a rotating magnetic field," *Magnitnaya Gidrodynamika*, Vol. 9, 1973, pp. 135–137.

[33] Calugaru, G. H., Cotae, C., Badescu, R., Badescu, V., and Luca, E., "A new aspect of the movement of ferrofluids in a rotating magnetic field," *Reviews in Rumanian Physics*, Vol. 21, 1976, pp. 439–440.

[34] Dahler, J. S. and Scriven, L. E., "Angular momentum of continua," *Nature*, Vol. 192, No. 4797, 1961, pp. 36–37.

[35] Dahler, J. S. and Scriven, L. E., "Theory of structured continua. I. General considerations of angular momentum and polarization," *Proceedings of the Royal Society of London, Series A*, Vol. 275, 1963, pp. 504–527.

[36] Condiff, D. W. and Dahler, J. S., "Fluid mechanical aspects of antisymmetric stress," *Physics of Fluids*, Vol. 7, No. 6, 1964, pp. 842–854.

[37] Shliomis, M. I., "Effective viscosity of magnetic suspensions," *Soviet Physics JETP*, Vol. 34, No. 6, 1972, pp. 1291–1294.

[38] Zahn, M. and Greer, D. R., "Ferrohydrodynamic pumping in spatially uniform sinusoidally time-varying magnetic fields," *Journal of Magnetism and Magnetic Materials*, Vol. 149, 1995, pp. 165–173.

[39] Zahn, M. and Pioch, L. L., "Ferrofluid flows in AC and traveling wave magnetic fields with effective positive, zero or negative dynamic viscosity," *Journal of Magnetism and Magnetic Materials*, Vol. 201, 1999, pp. 144–148.

[40] Rinaldi, C. and Brenner, H., "Body versus surface forces in continuum mechanics: Is the Maxwell stress tensor a physically objective Cauchy stress?" *Physical Review E*, Vol. 65, No. 3, 2002, pp. 036615.

[41] Rinaldi, C. and Zahn, M., "Effects of spin viscosity on ferrofluid flow profiles in alternating and rotating magnetic fields," *Physics of Fluids*, Vol. 14, No. 8, 2002, pp. 2847–2870.

[42] Brunn, P., "The velocity slip of polar fluids," *Rheologica Acta*, Vol. 14, No. 12, 1975, pp. 1039–1054.

[43] Aero, E. L., Bulygin, A. N., and Kuvshinski, E. V., "Asymmetric hydromechanics," *Journal of Applied Mathematics and Mechanics*, Vol. 29, 1965, pp. 333–346.

[44] Shliomis, M. I., Lyubimova, T. P., and Lyubimov, D. V., "Ferrohydrodynamics: an essay on the progress of ideas," *Chem. Eng. Comm.*, Vol. 67, 1988, pp. 275–290.

[45] Chaves, A., Rinaldi, C., Elborai, S., He, X., and Zahn, M., "Bulk flow in ferrofluids in a uniform rotating magnetic field," *Physical Review Letters*, Vol. 96, No. 19, 2006, pp. 194501(1–4).

[46] Rosensweig, R. E., "Continuum equations for magnetic and dielectric fluids with internal rotations," *Journal of Chemical Physics*, Vol. 121, No. 3, 2000, pp. 1228–1242.

[47] Brenner, H., "Rheology of two-phase systems," *Annual Review of Fluid Mechanics*, Vol. 2, 1970, pp. 137–176.

[48] Shliomis, M. I., "Concerning one gyromagnetic effect in a liquid paramagnet," *Sov. Phys. JETP*, Vol. 39, No. 4, 1974, pp. 701–704.

[49] Shliomis, M. I., "Ferrohydrodynamics: Testing a third magnetization equation," *Physical Review E*, Vol. 64, No. 06051(R), 2001, pp. 060501(1)–060501(4).

[50] Shliomis, M. I., "Comment on "Magnetoviscosity and relaxation in ferrofluids"," *Physical Review E*, Vol. 64, No. 063501, 2001, pp. 063501(1)–063501(6).

[51] Felderhof, B. U., "Steady-state magnetoviscosity of a dilute ferrofluid," *Magnitnaya Gidrodynamika*, Vol. 36, No. 4, 2000, pp. 329–334.

[52] Felderhof, B. U., "Magnetoviscosity and relaxation in ferrofluids," *Physical Review E*, Vol. 62, No. 3, 2000, pp. 3848–3854.

[53] Felderhof, B. U., "Reply to "Comment on 'Magnetoviscosity and relaxation in ferrofluids'"," *Physical Review E*, Vol. 64, 2001, pp. 063502(1)–063502(4).

[54] Stratton, J. A., *Electromagnetic Theory*, McGraw-Hill, New York, NY, 1941.

[55] Melcher, J. R., *Continuum Electromechanics*, MIT Press, Cambridge, MA, 1981.

[56] Kline, K. A., "Predictions from polar fluid theory which are independent of spin boundary-condition," *Transactions of the Society of Rheology*, Vol. 19, No. 1, 1975, pp. 139–145.

[57] Cowin, S. C., "Note on Predictions from polar fluid theory which are independent of spin boundary-condition," *Transactions of the Society of Rheology*, Vol. 20, No. 2, 1976, pp. 195–202.

[58] Kline, K. A., "Discussion of Predictions from polar fluid theory which are independent of spin boundary-conditions," *Journal of Rheology*, Vol. 26, No. 3, 1982, pp. 317–319.

[59] Lamb, H., *Hydrodynamics*, Dover, New York, NY, sixth ed., 1945.

[60] Deen, W. M., *Analysis of Transport Phenomena*, Oxford University Press, New York, NY, 1998.

[61] Brenner, H., "Rheology of a dilute suspension of dipolar spherical particles in an external field," *Journal of Colloid and Interface Science*, Vol. 32, No. 1, 1970, pp. 141–158.

[62] Bender, C. M. and Orszag, S. S., *Advanced mathematical methods for scientists and engineers*, Springer, New York, 1999.

[63] Rinaldi, C. and Chaves, A., "Comment on "Tangential stresses on the magnetic fluid boundary and rotational effect"," *Magnetohydrodynamics*, Vol. 43, No. 1, 2007, pp. 135–141.

[64] Chaves, A., Gutman, F., and Rinaldi, C., "Torque and bulk flow of ferrofluid in an annular gap subjected to a rotating magnetic field," *Journal of Fluids Engineering*, Vol. 129, 2007, pp. 412–422.

[65] Chantrell, R. W., Popplewell, J., and Charles, S. W., "Measurements of particle size distribution parameters in ferrofluids," *IEEE Transactions on Magnetics*, Vol. 14(5), No. 5, 1978, pp. 975–977.

[66] Kikura, H., Takeda, Y., and Durst, F., "Velocity profile measurements of the Taylor vortex flow of a magnetic fluid using the ultrasonic Doppler method," *Experiments in Fluids*, Vol. 26, 1999, pp. 208–214.

[67] Kikura, H., M. Aritomi, M., and Takeda, Y., "Velocity measurement on Taylor-Couette flow of a magnetic fluid with small aspect ratio," *Journal of Magnetism and Magnetic Materials*, Vol. 289, 2005, pp. 342–345.

[68] Rinaldi, C., Chaves, A., Elborai, S., He, X., and Zahn, M., "Magnetic fluid rheology and flows," *Current Opinion in Colloid and Interface Science*, Vol. 10, 2005, pp. 141–157.

[69] Lehlooh, A. F., Mahmood, S. H., and Williams, J. M., "On the particle size dependence of the magnetic anisotropy energy constant," *Physica B*, Vol. 321, No. 1-4, 2002, pp. 159–162.

[70] Takeda, Y., "Ultrasonic Doppler method for velocity profile measurement in fluid dynamics and fluid engineering," *Experiments in Fluids*, Vol. 26, 1999, pp. 177–178.

[71] de Gans, B. J., Blom, C., Mellema, J., and Philipse, A. P., "Preparation and magnetisation of a silica-magnetite inverse ferrofluid," *Journal of Magnetism and Magnetic Materials*, Vol. 201, 1999, pp. 11–13.

[72] de Gans, B. J., Blom, C., Philipse, A. P., and Mellema, J., "Linear viscoelasticity of an inverse ferrofluid," *Physical Review E*, Vol. 60, 1999, pp. 4518–4527.

[73] de Gans, B. J., Hoekstra, H., and Mellema, J., "Non-linear magnetorheological behaviour of an inverse ferrofluid," *Faraday Discussions*, Vol. 112, No. 112, 1999, pp. 209–224.

[74] de Gans, B. J., Duin, N. j., den Ende, D. v., and Mellema, J., "The influence of particle size on the magnerheological properties of an inverse ferrofluid," *Journal of Chemical Physics*, Vol. 113, 2000, pp. 2032–2042.

[75] Brito, D., Nataf, H.-C., Cardin, P., Aubert, J., and Masson, J.-P., "Ultrasonic Doppler velocimetry in liquid gallium," *Experiments in Fluids*, Vol. 31, 2001, pp. 653–663.

[76] Selfridge, A. R., "Approximate material properties in isotropic materials," *IEEE transactions on Sonics and Ultrasonics*, Vol. SU-32, No. 3, 1985, pp. 381–394.

[77] Eckert, S. and Gerbeth, G., "Velocity measurements in liquid sodium by means of ultrasound Doppler velocimetry," *Experiments in Fluids*, Vol. 32, 2002, pp. 542–546.

[78] Willemetz, J. C., "DOP2000 User's manual," 2001.

[79] Takeda, Y., "Velocity profile measurement by ultrasonic Doppler method," *Experimental Thermal and Fluid Science*, Vol. 10, 1995, pp. 444–453.

[80] Feng, S., Graham, A., Abbott, J., and Brenner, H., "Antisymmetric stresses in suspensions: vortex viscosity and energy dissipation," *Journal of Fluid Mechanics*, Vol. 563, 2006, pp. 97–122.